Dissertation

submitted to the
Combined Faculty of Mathematics, Engineering and Natural Sciences
of Heidelberg University, Germany
for the degree of
Doctor of Natural Sciences

Put forward by
Jonas Michael Schleske
born in: Munich, Germany
Oral examination: 26.11.2024

MINFLUX Tracking of Endogenous Dynein in Live Neurons

Referees: Prof. Dr. Dr. h.c. mult. Stefan W. Hell
Prof. Dr. Joachim Spatz

Zusammenfassung

MINFLUX ist eine neuartige Form der optischen Nanoskopie und ermöglicht die Einzelmolekül-Verfolgung mit einer räumlichen und zeitlichen Präzision im Nanometer-/Millisekundenbereich, indem wesentlich weniger detektierte Photonen benötigt werden als bei etablierten Methoden. Durch die Nutzung dieser photoneneffizienten Präzision ermöglichte MINFLUX die Verwendung einer vergleichsweise kleinen Fluoreszenzmarkierung, um die nanometerkleinen Schritte des molekularen Motors Dynein in lebenden primären Neuronen bei physiologischen Konzentrationen von Adenosintriphosphat (ATP) direkt zu beobachten. Bislang war dies lediglich *in vitro* und unter deutlich verlangsamten Bedingungen möglich. Die endogene Markierung von Dynein an verschiedenen Stellen erfolgte mittels CRISPR/Cas9, wobei die erfolgreiche Markierung durch den Einsatz eines selbstgebauten Weitfeldmikroskops verifiziert wurde. Im Rahmen der MINFLUX Messungen konnten Richtungswechsel innerhalb des bidirektionalen axonalen Transports beobachtet werden, die auf einer Zeitskala von einzelnen Schritten auftraten. Dies weist auf das Vorhandensein eines schnellen Umkehrmechanismus hin, der sich von einem stochastischen Tauziehen-ähnlichen Verhalten unterscheidet. Die Analyse der Millisekunden kurzen Verweildauern zwischen aufeinanderfolgenden Schritten ergab, dass der mechanochemische Zyklus durch eine einzige Ratenkonstante begrenzt ist, was wiederum darauf hindeutet, dass Dynein ein ATP pro Schritt verbraucht. Die Etablierung der Einzelmolekül-Verfolgung von endogenem Dynein in lebenden Neuronen mittels MINFLUX eröffnet die Möglichkeit, mit MINFLUX weitere minimal-invasive Studien zur schnellen und ungestörten Proteindynamik in lebenden Zellen durchzuführen.

Abstract

MINFLUX represents a novel class of optical nanoscopy techniques, enabling tracking measurements with nanometer/millisecond spatiotemporal precision by requiring substantially fewer detected photons than established methods for molecular tracking. By leveraging this photon-efficient precision, MINFLUX permitted the use of a comparatively small fluorescent label to directly observe the nanometer-sized steps of the molecular motor dynein in living primary neurons at physiological adenosine 5′-triphosphate (ATP) concentrations, which was previously only feasible *in vitro* and at markedly decelerated conditions. To tag dynein endogenously at different sites, CRISPR/Cas9 genome editing was implemented, and the successful tagging was confirmed through the utilization of a self-built widefield microscope. During MINFLUX tracking measurements, reversals within bidirectional axonal transport were observed to occur on a time scale corresponding to individual steps, indicating the presence of a rapid reversal mechanism that is distinct from a stochastic tug-of-war-like behavior. The analysis of the millisecond-short dwell times between consecutive steps revealed that the mechanochemical cycle is single-rate limited, indicating that dynein consumes one ATP to perform a step. Having established MINFLUX tracking of endogenous dynein in live neurons, it is anticipated that MINFLUX will facilitate further minimally invasive studies of rapid and undisturbed protein dynamics in live cells.

List of Abbreviations

AAA	*ATPases associated with diverse cellular activities*
ACSF	*Artificial cerebrospinal fluid*
ADP	*Adenosine diphosphate*
AIC	*Akaike Information Criterion*
AOTF	*Acousto-optic tunable filter*
ATP	*Adenosine 5′-triphosphate*
BFP	*Back focal plane*
bp	*Base pairs*
CDF	*Cumulative distribution function*
CFR	*Center frequency ratio*
cps	*Counts per second*
Da	*Dalton*
DHC	*Dynein heavy chain*
DIC	*Dynein intermediate chain*
EGFP	*Enhanced green fluorescent protein*
EMCCD	*Electron multiplying charge-coupled device*
Ex/Em	*Excitation and emission maxima*
FWHM	*Full width at half maximum*
gRNA	*Guide ribonucleic acid*
GFP	*Green fluorescent protein*
HILO	*Highly inclined and laminated optical sheet*
MAD	*Median absolute deviation*
mEGFP	*Monomeric enhanced green fluorescent protein*
MTBD	*Microtubule binding domain*
NA	*Numerical aperture*
ORANGE	*Open Resource for the Application of Neuronal Genome Editing*
PAINT	*Points accumulation for imaging in nanoscale topography*
PALM	*Photo-activated localization microscopy*
PAM	*Protospacer adjacent motif*
PCR	*Polymerase chain reaction*
PDF	*Probability density function*
px	*Pixels*
ROI	*Region of interest*

SBR	*Signal-to-background ratio*
SD	*Standard deviation*
STED	*Stimulated emission depletion*
STORM	*Stochastic optical reconstruction microscopy*
SVD	*Singular value decomposition*
TCP	*Targeted coordinate pattern*
TIR	*Total internal reflection*

Contents

1 Introduction

A multitude of intracellular processes and molecular reactions rely on diffusion. Nevertheless, for large particles that necessitate transport within a specified timeframe over a long distance within a cell, diffusive motion is insufficient (Mogre et al., 2020). Consequently, a transport system distinct from diffusion is required that is directed, specific, and rapid. Indeed, eukaryotic cells are on the one hand permeated by a complex and dynamic cytoskeleton that serves as tracks and on the other hand contain molecular motor proteins that are not only capable of rapidly moving along these molecular tracks but also specifically bind intracellular cargoes, thus enabling their directed transport (Vale, 2003).

In axons, which can extend for distances of millimeters to meters and represent the longest projections of neurons, the transport of cargo driven by motor proteins is of particular importance. The kinesin motor protein family and its counterpart, the cytoplasmic dynein 1 (hereafter referred to as dynein), are capable of processive movement, that is, movement without detaching from the track, along the unidirectionally oriented microtubules within the axon (Guedes-Dias and Holzbaur, 2019; Maday et al., 2014). Kinesin motors move from the soma towards the axon terminal (anterograde), whereas dynein moves in the opposite direction back to the soma (retrograde). This enables the transport of cargo in either direction by converting chemical energy into mechanical work through the hydrolysis of ATP (Schnitzer and Block, 1997). Given the essential role of axonal transport in neuronal development, homeostasis, and survival, impairments in this process have been linked to the pathogenesis of several neurological diseases, including Parkinson's disease, Alzheimer's disease, and amyotrophic lateral sclerosis, as well as neurodegenerative conditions (Hafezparast et al., 2003; Sleigh et al., 2019). A comprehensive investigation of axonal transport provides insights not only into the sophisticated molecular processes underlying motor proteins, but also may contribute to the development of potential therapeutic modalities for the treatment of neurological disorders.

To facilitate retrograde cargo transport, a tripartite motor complex is formed, comprising one or two dynein dimers, dynactin, and an activating adaptor that binds specifically to a particular cargo. Initial *in vitro* studies have demonstrated that dynein exhibits highly variable discrete steps on the microtubule lattice towards the minus end, utilizing artificially linked truncated yeast dynein monomers as a minimalistic study system (DeWitt et al., 2012; Qiu et al., 2012; Reck-Peterson et al., 2006). Consequently, different proposed stepping mechanisms have been put forth, including uncoordinated and independent head stepping (DeWitt et al., 2012; Qiu et al., 2012), which is notably distinct from the predominantly recurring

mechanisms observed in kinesin motors (Asbury et al., 2003; Hua et al., 2002; Yildiz et al., 2004). In addition to yeast dynein, the use of purified human and mammalian dynein motor complexes has revealed variable step sizes between 8 and 32 nm, which encompass frequent sideways and backwards stepping (Elshenawy et al., 2019; Mallik et al., 2004). Moreover, it has been demonstrated that dynein performs smaller steps, predominantly 8 nm in size, under the influence of an applied load through the use of an optical trap and beads attached to the dynein motor complex (Elshenawy et al., 2019; Mallik et al., 2004).

However, established methods of protein tracking that rely on the detection of a fluorescence diffraction pattern and subsequent centroid localization require an exceedingly high number of photons to attain sufficient localization precision for the detection of fast nanometer-sized steps (Eilers et al., 2018). As a result, measurements conducted *in vitro* to determine the individual steps of a dynein have utilized markedly reduced ATP concentrations to decelerate the movement of dynein by several orders of magnitude (DeWitt et al., 2012; Elshenawy et al., 2019; Mallik et al., 2004; Niekamp et al., 2021; Qiu et al., 2012; Reck-Peterson et al., 2006). In live cells, the direct tracking of dynein using a small label proved insufficient for detecting individual steps due to its rapid motion (Fellows et al., 2024; Tirumala et al., 2024; Twelvetrees et al., 2016). An alternative approach has been to track the transported cargo rather than dynein directly (Kural et al., 2005). This includes the use of large, strongly scattering optical probes with a diameter greater than 50 nm, which produce the requisite photon rates for detecting steps of the transported cargo (Nan et al., 2005; Peng et al., 2024). Consequently, the present understanding of dynein stepping behaviour is predominantly based on markedly decelerated *in vitro* measurements or extrapolated from cargo movement in live cells. Nevertheless, direct tracking of dynein in live cells necessitates an alternative approach capable of detecting individual steps with a minimally invasive and specific label, considerably smaller than the dynein motor complex itself.

Recent studies have demonstrated that MINFLUX enables the direct observation of unrestrained protein dynamics, including those of kinesin-1 (Deguchi et al., 2023; Wirth et al., 2023), through the use of a minimally invasive fluorescent label. In contrast to the passive collecting of photons in established centroid localization methods, the MINFLUX localization procedure actively positions the central intensity minimum (zero) of an excitation beam as closely as possible to the fluorophore position (Balzarotti et al., 2017). As the distance between the initially unknown fluorophore position and the known position of the intensity minimum decreases, the localization precision per detected photon increases. In practice, MINFLUX achieves single-digit nanometer precision with only a few hundred detected photons (Gwosch et al., 2020; Schmidt et al., 2021), thus enabling nanometer/millisecond spatiotemporal precision using a small single fluorophore. In comparison, established centroid localization techniques necessitate approximately a hundred times more detected photons to achieve a comparable spatiotemporal precision (Eilers et al., 2018). The generation of such high photon detection rates is typically only feasible with the use of large, highly scattering

labels, which are often many times larger than the protein under observation.

To study the stepping behavior of dynein directly and as a whole endogenous mammalian motor complex in live neurons, MINFLUX tracking with nanometer/millisecond spatiotemporal precision was utilized. For specific tagging of endogenous dynein, CRISPR/Cas9-mediated tagging of dynein at different sites was established, using tags that are notably smaller than the dynein motor complex. The implementation of a widefield microscope allows for the assessment of the endogenous dynein tagging and labeling procedure. A comprehensive analysis of the MINFLUX data was conducted to gain insights into naturally occurring direction reversals and pauses between processive movements at single-step resolution in live neurons. The fundamental attributes of the mechanochemical cycle of dynein were elucidated. Collectively, this work aims to characterize unrestrained endogenous dynein stepping directly and minimally invasively in live neurons using MINFLUX tracking.

2 MINFLUX Tracking of Endogenous Dynein

2.1 Tracking at Nanometer/Millisecond Precision with MINFLUX

2.1.1 Fluorescence Microscopy

The visualization of cellular structures and processes is a fundamental approach for understanding the underlying principles of living systems. Fluorescence microscopy has proven to be an indispensable tool for achieving this objective (Sahl et al., 2017). This is not only because light interacts with living matter in a minimally invasive manner, but also because the cellular components of interest can be specifically visualized within the complex environment of multiple other components. To this end, fluorophores are specifically attached to the target to be observed and excited by a light of matching wavelength, typically from a laser. The emitted color-shifted light is then separated from the excitation light by spectral filtering and collected on a detector, which is typically either a camera or a photodiode. In addition to high contrast, another key advantage of fluorescence microscopy is the ability to image live cells and thus dynamic processes within their cellular environment.

In general, the mechanism of fluorescence involves the absorption of a photon, which excites a molecule (fluorophore) to an excited state of higher energy. The molecule then rapidly relaxes non-radiatively into the lowest vibrational level of the higher electronic state. Fluorescence is the emission of a photon by relaxation of the molecule from the higher electronic state to the lower energy ground state (Lakowicz, 2006). The energy of the emitted photon is less than that of the absorbed photon, leading to a longer, red-shifted wavelength of the emitted fluorescence photon.

To further suppress unwanted background signal, including that from autofluorescence of cellular components, the incident light can be directed onto the sample at a highly inclined angle, leading to total internal reflection (TIR) at the interface between the coverslip and the sample medium. In this case, the incident light illuminates only a thin layer of the sample near the coverslip, from which fluorescence photons are emitted. Quantitatively, the angles of incidence θ_I and refraction θ_R are related to the refractive indices of the coverslip n_C and the sample medium n_M as given in Snell's law:

$$n_\mathrm{C} \cdot \sin\theta_\mathrm{I} = n_\mathrm{M} \cdot \sin\theta_\mathrm{R} \tag{2.1}$$

A critical angle θ_crit of incidence can be determined when the angle of refraction is set to 90°. For the refractive indices of the coverslip $n_\mathrm{C} = 1.52$ and the sample medium $n_\mathrm{M} = 1.33$, the

critical angle of incidence in the cover glass is

$$\theta_{\mathrm{crit}} = \arcsin \frac{n_{\mathrm{M}}}{n_{\mathrm{C}}} \approx 61^{\circ} \,. \tag{2.2}$$

For incidence angles that exceed the critical angle, TIR occurs. The associated evanescent field intensity decays exponentially into the sample medium and can be used to excite only those fluorophores that are close to the coverslip, while leaving those molecules that are farther away in the dark. Below the critical angle, but still at highly inclined angles, so-called highly inclined and laminated optical sheet (HILO) microscopy can be used to illuminate only a thin sheet of the sample with a high signal-to-background ratio (SBR), which is often used to study cellular structures or processes with widefield microscopy across an entire volume (Tokunaga et al., 2008).

2.1.2 Fluorescence Nanoscopy

For over a century, the diffraction limit, as formulated by Ernst Abbe, was considered an insurmountable barrier to defining the limits of attainable resolution, that is, the discernment of distinct details. It states that, due to the diffractive nature of light, the resolution is limited by half the wavelength λ and the inverse of the numerical aperture NA, which is approximately 200 nm for visible light.

$$d_{\mathrm{Abbe}} = \frac{\lambda}{2NA} \tag{2.3}$$

The NA, which serves as a measure of the ability of an objective lens to collect and focus light, can be expressed in terms of the refractive index n and the semi-aperture angle θ as $NA = n \sin\theta$.

While some concepts have pushed the limit to smaller scales, for instance via shorter wavelengths, higher refractive indices and/or structured illumination, the diffraction limit has only been conceptually overcome by separating in time the emitters within a diffraction-limited region rather than attempting their simultaneous detection. The overcoming of the diffraction limit constituted a paradigm shift that permitted imaging at much finer resolution, and was consequently awarded the 2014 Nobel Prize in Chemistry (Hell, 2015). Imaging below the diffraction limit became known as optical nanoscopy or super-resolution microscopy, and relies on time-sequential switching between a “bright” and a “dark” state of fluorophores (Hell, 2007). Within a diffraction-limited region, only a few or even a single fluorophore is detected in its bright state, while the remaining fluorophores in the diffraction-limited region are switched to and/or kept in a dark state. Subsequently, a different set of fluorophores are switched to their bright state and are thus detected, while the neighboring fluorophores are in a dark state. This time-sequential bright/dark transition of fluorophores and the exclusive detection of the few bright fluorophores within a diffraction-limited region is repeated until the entire region of interest (ROI) is read out to obtain a diffraction-unlimited image.

Depending on how the bright/dark transition of fluorophores is realized, the optical nanoscopy methods are divided into two categories (Sahl et al., 2017). The first category is that of coordinate-targeted nanoscopy, in which light is used to transition fluorophores to their dark and bright states at defined coordinates. The concept of stimulated emission depletion (STED), which laid the foundation for fluorescence nanoscopy, was proposed by Stefan W. Hell in 1994 (Hell and Wichmann, 1994) and was the first implementation of fluorescence nanoscopy in live cells (Klar et al., 2000). In STED, a de-excitation beam with a central intensity minimum is used to quench excited fluorophores (i.e., to force their transition to the dark state) within the diffraction-limited region. Consequently, only those fluorophores situated within the confined sub-diffraction region at the center of the de-excitation beam will fluoresce subsequent to being excited by a superimposed excitation beam with an intensity maximum (Hell, 2009). Therefore, the effective area of possible fluorescence is much smaller than the diffraction limit and can be reduced by increasing the intensity of the de-excitation beam. The diffraction-unlimited resolution of STED can be approximated by extending the Abbe diffraction limit as follows:

$$d_{\mathrm{STED}} \approx \frac{\lambda}{2NA \cdot \sqrt{1 + \frac{I}{I_{\mathrm{s}}}}}\,, \tag{2.4}$$

where I is the peak intensity of the de-excitation beam and I_{s} is the saturation intensity at which half of the fluorophores are depleted. By translating the known position of the depletion beam, a ROI can be read out in a targeted manner with diffraction-unlimited resolution. In principle, single-molecule ("infinite") resolution can be achieved when $I/I_{\mathrm{s}} \to \infty$ (Hell, 2007). In practice, the gain in resolution is limited by the residual intensity in the central minimum of the de-excitation beam and by photobleaching of the fluorophores.

The second category of fluorescence nanoscopy realizations relies on the stochastic transition between bright and dark fluorophore states. This coordinate-stochastic nanoscopy was originally implemented in photo-activated localization microscopy (PALM) (Betzig et al., 2006; Hess et al., 2006) and stochastic optical reconstruction microscopy (STORM) (Rust et al., 2006) by tuning the fluorophore properties such that only a single fluorophore can be in its bright state within a diffraction-limited region at a time, while the remaining fluorophores of the same region are in a dark state. The centroid of the bright molecule can be localized with a precision[1] proportional to the inverse square root of the number of photons N detected (Hell, 2007):

$$\sigma_{\mathrm{centroid}} \propto \frac{\lambda}{2NA \cdot \sqrt{N}} \tag{2.5}$$

As this approach relies on the localization of individualized bright molecules separated by at

[1] The localization precision in coordinate-stochastic nanoscopy is essentially equivalent to the concept of resolution, given that coordinate-stochastic nanoscopy relies on the time-sequential localization of individual molecules within one diffraction-limited region (Gwosch et al., 2023).

least one diffraction limit, it is often referred to as single-molecule localization microscopy. An alternative implementation of coordinate-stochastic nanoscopy is the recurrent reversible binding of fluorophores to target structures, which is known as points accumulation for imaging in nanoscale topography (PAINT) (Sharonov and Hochstrasser, 2006). In all these implementations, a diffraction-unlimited image is reconstructed after the acquisition by registering the centroids of the individualized bright fluorophores that were separated by a distance of at least one diffraction limit.

2.1.3 MINFLUX Nanoscopy and Tracking for Live-Cell Measurements

A decade after the implementation of coordinate-stochastic nanoscopy, MINFLUX introduced a novel class of nanoscopy, reducing the attainable localization precision by at least another order of magnitude into the single-digit nanometer regime (Balzarotti et al., 2017). MINFLUX nanoscopy incorporates aspects of both coordinate-targeted and coordinate-stochastic nanoscopy approaches, yet it differs significantly from both in that it not only surpasses the diffraction limit (Eq. 2.3) but also overcomes the inverse square root dependence of detected photons (Eq. 2.5) inherent to coordinate-stochastic nanoscopy. This is achieved by relating the unknown positions of individualized fluorophores (coordinate-stochastic nanoscopy) with the known shape and sampling positions of an excitation pattern (coordinate-targeted nanoscopy). Typically, the excitation pattern exhibits one or more intensity minima, ideally of zero intensity, in lieu of an intensity maximum. By positioning the intensity minimum in ever-increasing proximity to the fluorophore, the photon flux is minimized, while the positional information obtained per detected fluorescence photon is maximized. In the theoretical limit of exact superimposition of the intensity minimum (zero) and the fluorophore, no fluorescence photons would be detected, while the position of the fluorophore would be precisely determined. Should the fluorophore then undergo minor displacement, a few detected photons would be sufficient to steer the intensity minimum in a manner that would once again superimpose it with the position of the fluorophore. Consequently, rather than requiring an exceedingly high number of detected photons for the passive localization of a fluorophore, the inverse square root dependence is overcome in MINFLUX through the active searching and tracking of a fluorophore by an intensity minimum.

Upon implementation of MINFLUX, an intensity minimum featuring a strong curvature probes several positions around the estimated fluorophore position, following a targeted coordinate pattern (TCP) of extent L. By utilizing a donut-shaped excitation beam with a central minimum and an L that is much smaller than the beam focus, the background-free MINFLUX localization precision with a fluorophore situated at the center is proportional to L (Balzarotti et al., 2017):

$$\sigma_{\text{MINFLUX}} \geq \frac{L}{2\sqrt{2N}} \tag{2.6}$$

Significantly, the precision of MINFLUX localization is not solely dependent on the inverse square root of detected photons N, as is the case with coordinate-stochastic nanoscopy. Instead, it is also linearly proportional to L, which represents twice the distance between the excitation minimum position and the estimated fluorophore position. Consequently, reducing L, that is, bringing the excitation minimum closer to the fluorophore, results in a much faster reduction in localization precision compared to collecting more fluorescence photons. In other words, MINFLUX implements an iterative fluorophore search and reduction of L (Gwosch et al., 2020), thereby capitalizing on the rapid decline of the inverse square root function in each iteration. This is in contrast to the non-iterative localization procedure used in coordinate-stochastic nanoscopy, which is dependent on the collection of a multitude of photons to precisely determine the fluorophore position (Eq. 2.5). Following the completion of one MINFLUX iteration, the initial photons with high positional information detected at the probed positions of the TCP are used to estimate the fluorophore position. This estimation of the fluorophore position serves as the new TCP center for the subsequent iteration with reduced L. By repeating the iterative reduction of L around the increasingly precise position estimate of the fluorophore, a localization precision of a single nanometer can be readily achieved using just a few hundred fluorescence photons (Balzarotti et al., 2017; Gwosch et al., 2020; Schmidt et al., 2021). As a result, MINFLUX is markedly more photon efficient than other coordinate-stochastic nanoscopy techniques.

The photon efficiency of MINFLUX is of paramount importance not only for imaging purposes but also for tracking applications (Fig. 2.1A). Established single-particle tracking methods are severely constrained by the limited photon rate of fluorophores. This is evident if the detected photons N in Equation 2.5 are replaced by a fluorescence photon rate k at a specific time interval τ, which can be regarded as time resolution.

$$\sigma_{\text{centroid}}\sqrt{\tau} \propto \frac{1}{\sqrt{k}} \cdot d_{\text{Abbe}} \tag{2.7}$$

In order to achieve a spatiotemporal precision in the lower single-digit nanometer and millisecond regime—for example, to resolve steps of molecular motor proteins at physiological ATP concentrations—a fluorescence photon detection rate in the million counts per second (cps) regime is necessary (Fig. 2.1B). This is a considerably higher rate than what is typically measured from single fluorophores. It is only possible to achieve such high count rates by utilizing large optical probes, such as gold (Ando et al., 2020) or upconverting nanoparticles (Peng et al., 2024), or aggregates of quantum dots (Nan et al., 2005), which are all substantially larger than the protein under observation. To retain the use of individual fluorophores for tracking, one alternative approach involves markedly slowing down protein movement *in vitro*. This allows for sufficient fluorescence photon collection for single-digit nanometer precision, albeit at a time resolution of approximately 100 ms (Yildiz and Selvin, 2005). However, both approaches, namely the use of large optical probes or decelerated dynamics, are disadvantageous for directly and minimally invasively tracking protein dynamics in live cells.

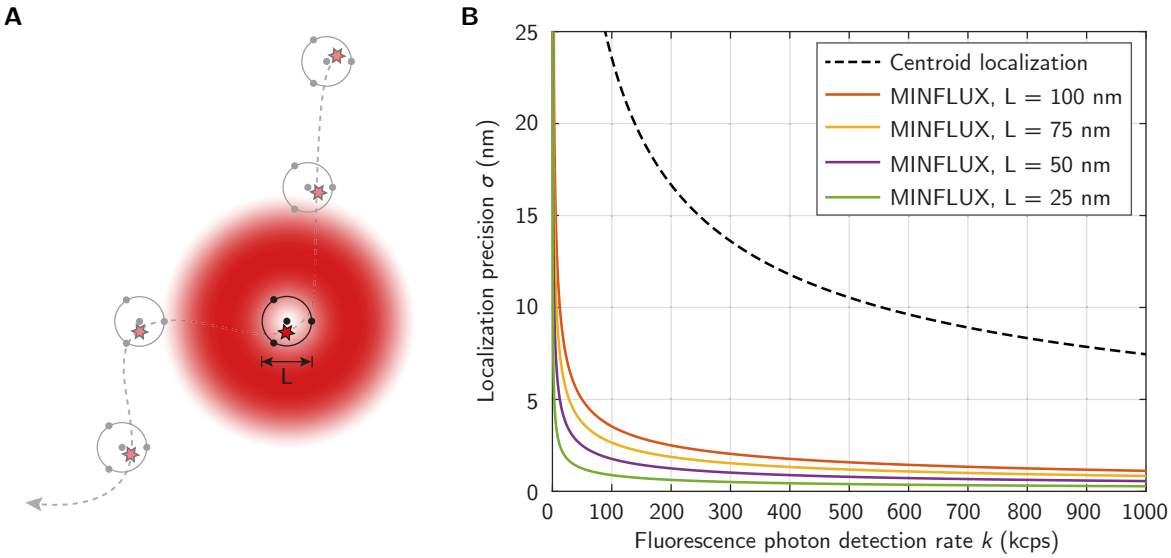

Figure 2.1 | MINFLUX tracking procedure and localization precision
(A) Schematic of the MINFLUX tracking procedure following a moving fluorophore (red star) along a trajectory (dashed line). In a typical MINFLUX tracking procedure, a single isolated and non-blinking fluorophore is first localized with a beam featuring an intensity maximum. This is followed by the described iterative localization procedure with an intensity minimum and a reduction of L. Once a final L is reached, L is held constant and the red donut-shaped excitation beam (here 640 nm wavelength) repeatedly probes (in this case) three positions around the estimated fluorophore position (dots) and one at the center of the TCP, thereby successively determining the position of the moving fluorophore. Past and future fluorophore positions and the corresponding TCPs are shown as faded out. For purposes of clarity, successive localizations are depicted with greater separation than would be the case in practice. **(B)** The centroid and MINFLUX localization precisions are plotted against the fluorescence photon count rate at a fixed time resolution of 1 ms using Equations 2.7 and 2.8 with $\lambda = 660\,\text{nm}$ and $NA = 1.4$.

In contrast, MINFLUX has demonstrated the capacity to enable spatiotemporal precision in the single-digit nanometer and millisecond range, for instance when applied to the tracking of kinesin-1 (Deguchi et al., 2023; Wirth et al., 2023). This is due to the fact that the spatiotemporal precision is no longer solely dependent on the inverse square root of fluorescence photons, but also on the reducible TCP diameter L and an iterative fluorophore position estimation.

$$\sigma_{\text{MINFLUX}}\sqrt{\tau} \propto \frac{1}{\sqrt{k}} \cdot \frac{L}{2\sqrt{2}} \tag{2.8}$$

Consequently, even with an $L = 75\,\text{nm}$ (Fig. 2.1B), a lower single-digit nanometer precision at a time resolution of 1 ms can be achieved at a fluorescence photon rate below 100 kcps, which is within the range of what single organic fluorophores provide under continuous wave excitation. A comparison of the spatiotemporal precisions of centroid localization and MINFLUX tracking ($L = 75\,\text{nm}$) reveals that at an equivalent fluorescence photon count rate, the attainable localization precision is almost one order of magnitude smaller for MINFLUX (Fig. 2.1B). For equivalent localization precision, MINFLUX reduces the required count rate by almost two orders of magnitude[2]. In addition to the restricted fluorescence photon rate, the total photon budget is constrained by photobleaching. Therefore, the photon efficiency of MINFLUX also permits tracking over a longer period of time compared to centroid localization (Kural et al., 2005), as MINFLUX requires considerably fewer photons per localization of similar precision. In conclusion, the superior spatiotemporal precision per photon rate and budget of MINFLUX is anticipated to facilitate direct and minimally invasive tracking of endogenous proteins in live cells using a single fluorophore that is substantially smaller than most proteins, including dynein.

2.2 Endogenous Protein Tagging via CRISPR/Cas9

In the pursuit of visualizing rapid, dynamic processes in live cells, fluorescent and covalent labeling of target proteins represents a powerful and versatile tool. This is typically achieved by introducing a plasmid into the cell that genetically encodes the protein of interest, which is fused to a tag that is either fluorescent in itself (e.g., the green fluorescent protein (GFP) (Prasher et al., 1992)) or to a self-labeling protein tag, such as SNAP-tag (Keppler et al., 2003) or HaloTag (Los et al., 2008). Consequently, the tagged protein of interest is (over)expressed within the cell, under the control of an exogenous promoter. In the case of a self-labeling protein tag, a cell-permeable fluorophore is introduced into the cell in a second step. This fluorophore is conjugated to an O^6-benzylguanine derivative for the SNAP-tag or to a chloroalkane for the HaloTag. It then binds covalently to the self-labeling protein tag, thus labeling the protein of interest (Xue et al., 2015). This approach offers the benefit of

[2]It is noteworthy that this discrepancy is further accentuated at smaller L, as also apparent in Figure 2.1B.

utilizing organic fluorophores at a preferred concentration, which often exhibit higher fluorescence photon rates and greater resistance to photobleaching compared to fluorescent proteins (Crivat and Taraska, 2012).

The expression of tagged proteins has the practical advantage of relatively low effort, but often results in overexpression artifacts or cytotoxicity and can severely disturb native processes of the cell (Gibson et al., 2013). For example, in the case of the multiprotein complex dynein, the overexpression of individual subunits has been observed to disrupt the fine-tuned composition and regulation of the entire complex (Burkhardt et al., 1997; Moughamian et al., 2013), as well as affect endomembrane localization (King et al., 2003; Vaughan et al., 2001).

As an alternative to exogenous expression, CRISPR/Cas9-based gene editing strategies enable the modification of the genome of the cell itself (Doudna and Charpentier, 2014; Knott and Doudna, 2018) allowing for endogenous expression of the tagged protein of interest controlled by the endogenous promoter (Ratz et al., 2015). This is accomplished by inserting a donor sequence encoding the tag specifically at the gene locus corresponding to the protein of interest. Since neurons are non-dividing cells and therefore homology-based strategies are inefficient (Suzuki et al., 2016), strategies based on non-homologous end-joining are preferable. The recently introduced homology-independent Open Resource for the Application of Neuronal Genome Editing (ORANGE) enables accurate and efficient knock-in of donor sequences for tagging proteins of interest in live neurons (Willems et al., 2020). The provided CRISPR/Cas9 knock-in template vector (pORANGE) renders the tagging of custom proteins of interest particularly convenient, as all the target, donor, Cas9, and guide ribonucleic acid (gRNA) sequences are located on a single plasmid (Fig. 2.2).

The CRISPR/Cas9-mediated tagging process, utilizing the ORANGE knock-in approach in live neurons, is conducted as follows: A CRISPR/Cas9 knock-in plasmid, generated specifically for this purpose, is introduced into freshly cultured primary neurons, for example, by electroporation. The neuron expresses the endonuclease Cas9, which is encoded on the plasmid and originally part of the adaptive immune system of bacteria and archaea against foreign plasmids and viruses (Jinek et al., 2012). This enzyme can introduce double-stranded breaks in DNA, directed by a gRNA. The gRNA contains a 20-nucleotide-long target sequence that specifically corresponds to the gene locus where the desired tag should be incorporated into the genome and a protospacer adjacent motif (PAM) site at which next to it the DNA is cleaved (Doudna and Charpentier, 2014). The ORANGE-based approach utilizes the expressed Cas9 to cleave the gene locus and excise the donor sequence encoding the tag from the plasmid (Fig. 2.2). Subsequently, the donor sequence is incorporated into the cleaved gene locus via non-homologous end-joining. The donor sequence is designed in such a way that if the tag is incorporated in reverse, two complete target sequences and PAM sites are created. This leads Cas9 to cut out the incorrectly incorporated donor sequence, thus ensuring the correct integration of the tag into the genome (Willems et al., 2020). Finally, the genome is modified to comprise the desired tag at a specific gene locus, resulting in the endogenous

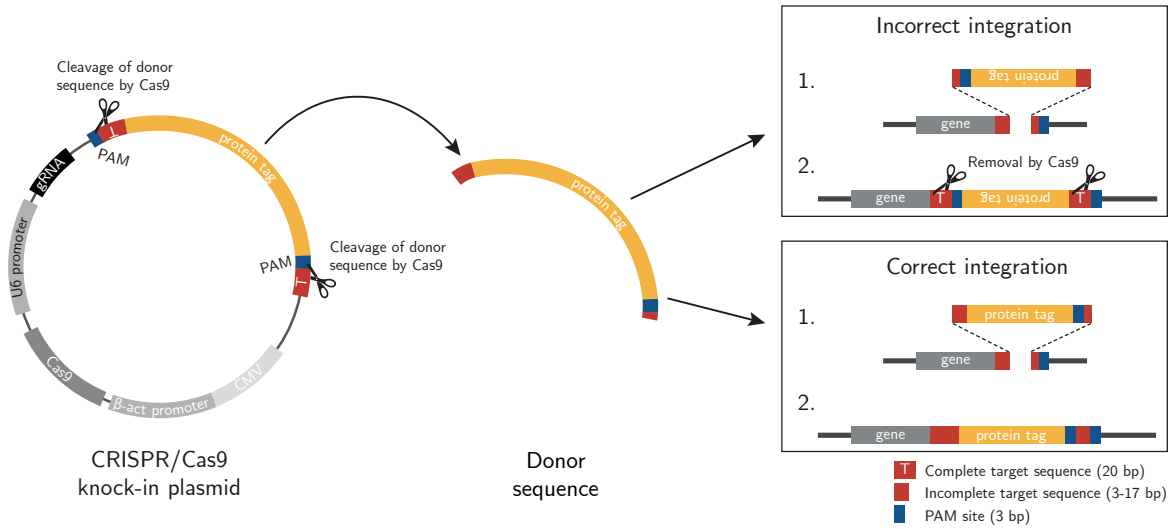

Figure 2.2 | CRISPR/Cas9-mediated Tagging of Endogenous Proteins in Live Neurons
The CRISPR/Cas9 knock-in plasmid (schematic representation, an example plasmid map can be found in Figure 3.1) contains the donor sequence encoding the protein tag, which is flanked by the 20-nucleotide-long target sequence and the PAM site. The expression of Cas9 is driven by a β-actin promoter in combination with a CMV enhancer, while the U6 promoter is responsible for the expression of the gRNA. Following electroporation, the Cas9 protein is expressed, which both excises the protein tag from the plasmid and specifically cleaves the gene locus. In the event that the donor sequence is integrated into the genome in reverse, two target sequences and PAM sites are created, which prompt Cas9 to excise the incorrectly integrated donor sequence from the genome once more. Conversely, if the orientation is correct, no genomic target sites are generated, ensuring that the donor sequence encoding the protein tag remains correctly integrated into the genome. Consequently, the neuron endogenously expresses protein of interest with the incorporated tag. The figure draws inspiration from the work of Willems et al., 2020.

expression of the desired tagged protein of interest.

In conclusion, CRISPR/Cas9-mediated protein tagging enables fluorescent labeling of endogenous proteins and thus visualization of unperturbed and native dynamic processes in live neurons. While a previous study has demonstrated the endogenous tagging of dynein in induced neurons (Fellows et al., 2024), this work applies a different approach to establishing endogenous tagging of dynein in primary neurons.

2.3 Motor-Driven Intracellular Transport by Dynein

2.3.1 Physical Principles of Intracellular Transport

Living systems are highly dynamic. However, the driving forces of motion within a cell differ markedly from that observed macroscopically. The Reynolds number Re provides a means of quantifying the relative dominance of inertial forces over viscous forces within a given fluid of density ρ and viscosity η, as follows (Purcell, 1977):

$$Re = \frac{av\rho}{\eta}\,, \tag{2.9}$$

wherein a represents the characteristic length scale and v denotes the velocity. A low Reynolds number indicates that viscous forces are dominant, while a high Reynolds number indicates that inertial forces are dominant. To illustrate, for a human swimmer with $a = 1\,\mathrm{m}$ and $v = 1\,\mathrm{m\,s^{-1}}$, the Reynolds number is $Re = 10^6$, considering water with $\rho = 1\,\mathrm{g\,cm^{-3}}$ and $\eta = 10^{-3}\,\mathrm{Pa\,s}$, but for a protein with $a = 10\,\mathrm{nm}$ and $v = 1\,\mathrm{\mu m\,s^{-1}}$, the Reynolds number is $Re = 10^{-8}$. This rough estimation emphasizes the enormous difference in Reynolds numbers, which span 14 orders of magnitude. Consequently, for macroscopic objects, inertial forces are dominant ($Re \gg 1$), whereas for intracellular entities, such as proteins, hydrodynamic forces are of a viscous nature ($Re \ll 1$). The latter may be envisioned by considering oneself immersed in honey.

An additional consequence of operating at low Reynolds numbers becomes evident when considering the (incompressible) Navier-Stokes equation. In the limit of $Re \ll 1$, the inertial terms are negligible, thereby reducing the Navier-Stokes equation to the Stokes equation:

$$\underbrace{\rho\left(\frac{\partial\vec{v}}{\partial t} + \left(\vec{v}\cdot\vec{\nabla}\right)\vec{v}\right)}_{\text{inertial forces}} = \eta\Delta\vec{v} - \vec{\nabla}p \quad \overset{Re\ll 1}{\Longrightarrow} \quad \eta\Delta\vec{v} = \vec{\nabla}p\,, \tag{2.10}$$

where p denotes the pressure. Notably, by disregarding the inertial terms, the temporal dependence also disappears. This implies that solely the instantaneous forces are of consequence, not those from the past. Additionally, motion is reversible, irrespective of whether it is slow or fast. Consequently, movement at low Reynolds numbers adheres to a markedly different principle than that observed at the macroscopic scale. This is known as the “Scallop Theorem”,

named by Purcell, as a macroscopic scallop is capable of swimming through reciprocal motion of its shells, yet is unable to do so at low Reynolds numbers. Swimming at low Reynolds numbers is, however, possible by a corkscrew-like propulsion (e.g., that of a prokaryotic flagellum) or by a flexible "oar" (e.g. that of a eukaryotic flagellum or cilium, driven by dyneins) (Purcell, 1977).

In considering intracellular movement, it is essential to take into account the additional forces that are at work, namely thermal forces. These forces originate from random collisions among solute particles, resulting in diffusive motion. Thermal forces play a role at the cellular level due to their comparable magnitude to deterministic intracellular forces (Phillips et al., 2012). This is evident when considering the thermal energy scale at body temperature ($T \approx 310\,\mathrm{K}$), which yields $k_\mathrm{B}T \approx 4\,\mathrm{pN\,nm}$, where k_B denotes Boltzmann's constant. Indeed, molecular motor proteins exert forces in the piconewton range (Elshenawy et al., 2019), resulting in conformational changes within the nanometer range.

To obtain an estimation of the length and time scales of diffusion, it is useful to consider the following relation. The mean squared displacement $\langle r^2 \rangle$ of a solute particle is proportional to the diffusion coefficient D and time t, as indicated by

$$\langle r^2 \rangle \propto D t^\alpha \,. \tag{2.11}$$

In a continuous hydrodynamic fluid, the exponent $\alpha = 1$. However, given the heterogeneous composition of the cytoplasm within cells, comprising a range of solute particles of varying sizes, it is probable that anomalous subdiffusion occurs, with $\alpha < 1$ (Dix and Verkman, 2008). In order to roughly estimate the time scale for different particles to diffuse, it is possible to make use of the Stokes-Einstein relation, which provides an estimate for the diffusion coefficient (Phillips et al., 2012):

$$D = \frac{k_\mathrm{B}T}{6\pi\eta R} \,, \tag{2.12}$$

with R denoting the radius of a spherical particle in a continuous fluid of viscosity η. When considered for simplicity, $\alpha = 1$ in Equation 2.11, the time scale for a small metabolite of 1 nm in size to diffuse across a bacterium of 1 µm in size would be 1 ms. This is in stark contrast to the time scale required for a vesicle of 100 nm radius to diffuse a length scale of a meter-long axon in the human peripheral nervous system, which would be more than 10,000 years. It thus follows that a different transport system is required for the conveyance of large intracellular cargoes and axonal distances.

In conclusion, intracellular transport can be classified into three main categories, depending on the underlying physical principle (Mogre et al., 2020). Firstly, diffusion-based transport of small molecules over short distances has the advantage of not requiring additional energy beyond that which is provided by thermal energy. As a second category with a greater degree of control, intracellular flow can be employed for the transportation of a broad range of

particles. For example, this can be generated by myosin-driven contraction of actin filament networks (Deneke et al., 2019) or by cell shape deformation (Koslover et al., 2017). Lastly, the highest level of control is provided by molecular motor-driven transport of intracellular cargo, which is considerably faster than diffusion over axonal distances. However, this comes at the cost of requiring additional energy in the form of ATP. One such molecular motor, namely dynein, will be discussed in greater detail in the subsequent section.

2.3.2 The Molecular Motor Dynein

Although cytoplasmic dynein was first identified in 1987 (Paschal et al., 1987; Paschal and Vallee, 1987), it took several years to elucidate its structure and study its dynamics. This was likely due to the enormous size and complex assembly and activation of the motor protein, particularly in mammalian and human cells (Canty et al., 2021). In addition to cytoplasmic dynein, which is responsible for the retrograde transport of a variety of intracellular cargoes in the cytoplasm (Reck-Peterson et al., 2018) and plays a pivotal role during cell division (Sharp et al., 2000), there are also ciliary dyneins that drive intraflagellar retrograde transport and ciliary beating, the latter also referred to as axonemal dyneins (Nachury and Mick, 2019). This work, however, focuses on cytoplasmic dynein 1 (herein referred to as dynein) in live neurons, which are non-dividing cells. In neuronal axons, dynein is the sole motor responsible for transporting intracellular cargo in the retrograde direction on microtubules (Guedes-Dias and Holzbaur, 2019), which are uniformly aligned in axons (Baas et al., 1988).

Dynein is a dimer comprising six subunits, with a molecular weight of 1.4 MDa. The dynein heavy chain (DHC) is the largest of the subunits. It contains a motor domain at its C-terminus and a tail domain at its N-terminus (Fig. 2.3A), where the two heavy chains are dimerized (Zhang et al., 2017). While both dynein and kinesin motors perform discrete steps on microtubules (Walter and Diez, 2012), they differ in numerous ways. In addition to being oriented in opposite directions, a notable distinction is that the motor domain of dynein is separated from its microtubule-binding domain (MTBD) by a 15 nm-long coiled-coil stalk. The motor domain is comprised of a ring of six structurally distinct ATPases associated with diverse cellular activities (AAA) domains. Notably, ATP binding is possible to four of these AAA domains, whereas only the ATP hydrolysis at AAA1 has been demonstrated to be pivotal for dynein's motility (Kon et al., 2004). AAA3 (Bhabha et al., 2014; DeWitt et al., 2015; Nicholas et al., 2015) and AAA4 (Liu et al., 2020) have been identified to serve regulatory functions. However, it remains unclear whether ATP hydrolysis at AAA3 and/or AAA4, in conjunction with AAA1, is necessary to perform a single step.

The stepping of dynein and the corresponding translation of cargo along microtubules are typically described in the context of AAA1's mechanochemical cycle (Yildiz and Zhao, 2023). The latter involves the conversion of chemical energy into mechanical work by means of the hydrolysis of ATP, occurring on a repetitive basis. The four nucleotide states of a mechanochemical cycle within one motor domain of a dynein monomer in the AAA1 site

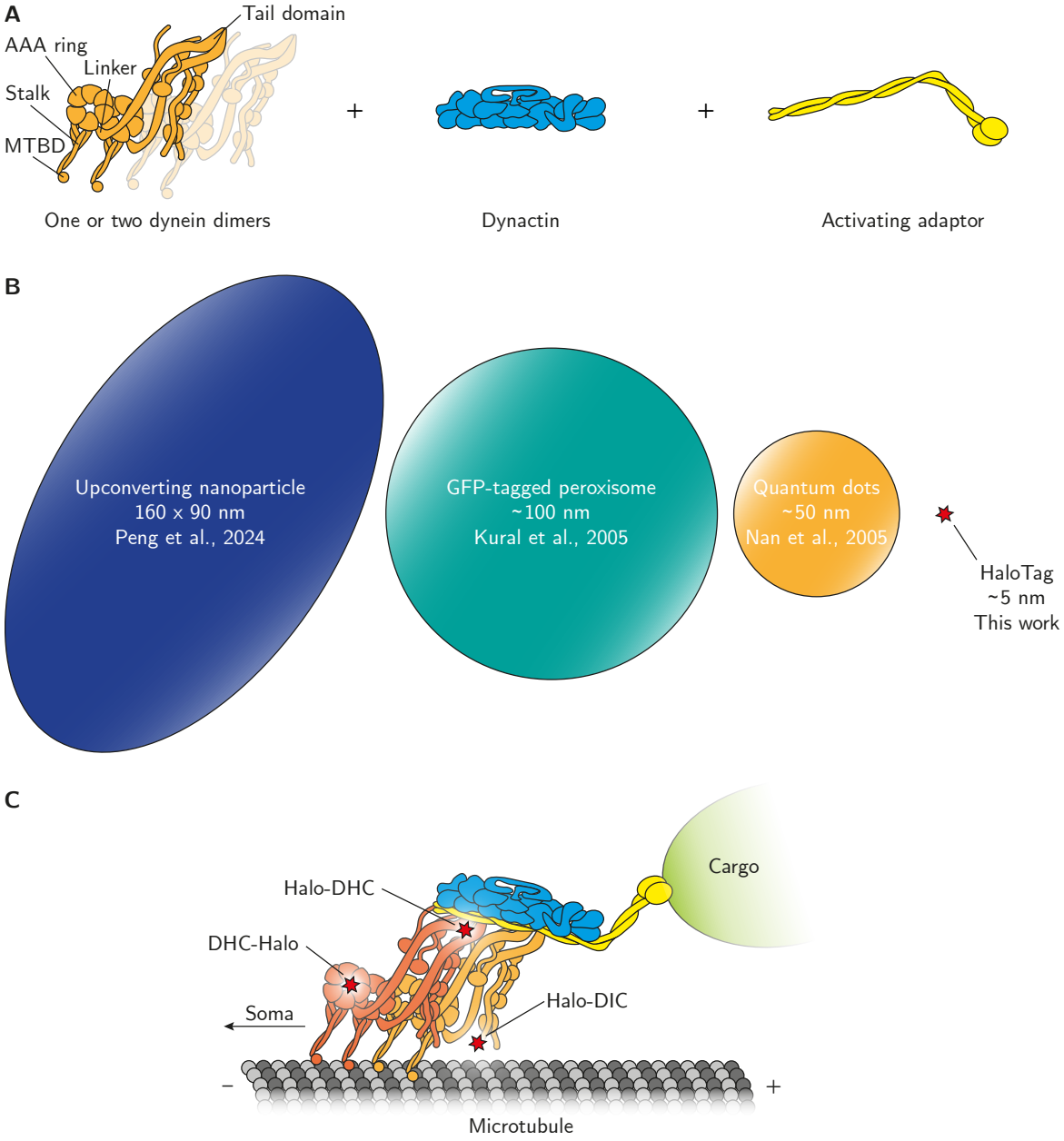

Figure 2.3 | Tagging of dynein in live cells
(A) The formation of an active dynein motor complex in mammalian and human cells involves the assembly of a tripartite complex comprising one or two dynein dimers, dynactin, and an activating adaptor. A dynein dimer is composed of two copies of each of the following: heavy chain, intermediate chain, light-intermediate chain, and three light chains. The activating adaptor binds a specific intracellular cargo. For purposes of clarity, the $p150^{Glued}$ subunit of dynactin is not shown. **(B)** Various strategies for labeling dynein in live cells with corresponding tags are illustrated, with the dimensions of the tags approximated to scale relative to that of dynein. The respective dimensions of the tags and corresponding references are indicated. **(C)** The fully assembled dynein motor complex is depicted on a microtubule moving in the retrograde direction to the soma. A red star indicates each of the three potential sites where a HaloTag is conjugated to dynein in this work via CRISPR/Cas9-mediated endogenous tagging.

correspond to the nucleotide that is bound, respectively (empty→ATP→adenosine diphosphate (ADP) and inorganic phosphate→ADP→...). The catalytic ATPase activity of AAA1 is proposed to be linked to the following conformational changes that are traversed in the course of a single mechanochemical cycle (Canty et al., 2021). However, the precise sequence of conformational changes and nucleotide states remains unclear.

It is proposed that the mechanochemical cycle commences with the AAA1 domain in its unbound state, with the MTBD exhibiting a strong affinity for the microtubule and the linker remaining in a straight configuration. Upon binding of ATP, the MTBD is released from the microtubule. Following the hydrolysis of ATP, the linker bends and dynein performs a priming stroke, which moves the MTBD towards the minus end of the microtubule. In fact, upon detachment of the MTBD from the microtubule, the MTBD initiates a diffusional search for the subsequent potential binding site on the microtubule lattice. Given that the αβ-tubulin dimers are spaced approximately 8 nm apart along the microtubule axis (on-axis direction) (Alushin et al., 2014), the possible steps are multiples of 8 nm (Carter et al., 2008), including the possibility of exceptional backsteps. Furthermore, the MTBD is capable of stepping sideways (off-axis direction) and binding to an adjacent protofilament that is approximately 6 nm apart (Asenjo et al., 2013). This is believed to facilitate the rerouting of obstacles on the track (Ferro et al., 2019). The mechanochemical cycle continues with the rebinding of the motor to the microtubule, which results in the dissociation of inorganic phosphate. In its ADP-bound state, the linker reverts to a straight conformation, referred to as the power stroke. This force-generating movement is believed to eventually exert a pulling force on the cargo. Ultimately, ADP dissociates, and the motor domain is prepared for the next round of the mechanochemical cycle. The completion of a step by dynein on the microtubule lattice thus entails the passage of one mechanochemical cycle, which is almost exclusively observed to consume one ATP molecule per cycle (DeWitt et al., 2015; Elshenawy et al., 2019; Mallik et al., 2004; Reck-Peterson et al., 2006; Slivka et al., 2024; Toba et al., 2006). However, as previously stated, there is a debate regarding whether the completion of one mechanochemical cycle involves the consumption of two ATP molecules (Peng et al., 2024).

In addition to the dynein dimer, a processive mammalian and human motor complex is only formed upon the assembly with dynein's cofactor dynactin and an activating adaptor (Fig. 2.3A). In the absence of these components, a single dynein dimer adopts an autoinhibited conformation, designated as the ϕ-particle, which impedes the concurrent binding of both MTBDs to the microtubule (Zhang et al., 2017). Dynactin is another extensive multiprotein complex with a molecular weight of 1.1 MDa, comprising 23 proteins. In live cells, a second dynein dimer typically assembles with dynactin (Grotjahn et al., 2018), which enhances the force production and speed of the motor complex (Elshenawy et al., 2019; Urnavicius et al., 2018). The processive dynein motor complex moves at a speed of more than $1\,\mu m\,s^{-1}$ in live neurons (Fellows et al., 2024), which is however also dependent on the cargo being trans-

ported (Klinman and Holzbaur, 2016). In addition to dynactin, the formation of a stable and processive dynein motor complex also requires the binding of an activating adaptor's coiled-coil domain (Urnavicius et al., 2015). The activating adaptor specifically binds to an intracellular cargo, thereby facilitating the connection of the dynein motor to the cargo and thus activating processive motility (McKenney et al., 2014). It is noteworthy that there are numerous distinct activating adaptors for various intracellular cargoes, yet a single motor, namely dynein, is responsible for retrograde transport (Canty et al., 2021). This is in contrast to the approximately 40 different kinesin motors that are responsible for anterograde transport. The transported cargo includes not only large membrane cargos such as mitochondria, endosomes, and peroxisomes but also viruses, RNA cargoes, and protein cargoes such as microtubules or misfolded proteins (Reck-Peterson et al., 2018).

Given the plethora of intracellular cargo, it is unsurprising that there are numerous regulatory levels to ensure the cargo is transported to the appropriate location at the correct time (Guedes-Dias and Holzbaur, 2019). It is not uncommon for opposite polarity kinesin and dynein motors to be anchored to the same cargo (Encalada et al., 2011; Maday et al., 2012), which facilitates bidirectional transport. Nevertheless, the precise mechanism by which directionality is controlled remains elusive. One proposed model to explain bidirectionality is the so-called "tug-of-war" model (Müller et al., 2008; Vale et al., 1992; Welte et al., 1998), which describes a stochastic mechanical competition between kinesin and dynein motors. While some live cell observations can be somewhat modeled by a tug-of-war this model fails to explain, among other observations, the "co-dependence" of both motors (Hancock, 2014). The latter describes the observation that for many bidirectionally transported cargoes, the inhibition of one motor also leads to an inhibition of the opposing motor (Ally et al., 2009; Encalada et al., 2011; Martin et al., 1999).

An additional potential explanation for the observed bidirectional intracellular transport in live cells is the involvement of regulatory factors. It has been demonstrated that activating adaptors can simultaneously recruit both kinesin and dynein motors (Canty et al., 2023; Fenton et al., 2021; Kendrick et al., 2019). Conversely, other adaptors have been shown to recruit either kinesin or dynein motors (Fu and Holzbaur, 2013). A further recent observation is that dynein and dynactin are partially spatially separated in order to prevent the formation of an active dynein motor complex during anterograde motility, thus promoting long-range transport in the axon (Fellows et al., 2024). Finally, post-translational modifications of the microtubules and microtubule-associated proteins represent an additional layer of transport regulation (Janke and Magiera, 2020). It is conceivable that controlling intracellular transport is a combination of these different layers. Nevertheless, it seems implausible that in live cells, pure stochastic mechanical competition (tug-of-war) is responsible for spatial and temporal precise cargo delivery. This hypothesis can potentially be tested by investigating the pause and reversal behavior of bidirectional transport with high spatiotemporal precision.

A further distinction between kinesin motors and dynein is their differing stepping be-

havior and mechanism. While kinesins have been observed to perform alternating stepping of their head domains (Wirth et al., 2023), regardless of whether they are described by a hand-over-hand (Yildiz et al., 2004) or inchworm mechanism (Hua et al., 2002), the stepping of the dynein motor domains has been observed to be independent of each other, at least in the context of the model system of artificially dimerized, tail-truncated yeast dynein *in vitro* (DeWitt et al., 2012; Qiu et al., 2012). Due to the elongated stalk and tail domain, which permits a substantial separation of the two dynein monomers, variable step sizes and recurrent sideways stepping are also observed for dynein *in vitro* (Elshenawy et al., 2019), in contrast to kinesins, where both head domains typically adhere to the same protofilament.

Nevertheless, several observations regarding dynein stepping have been derived from decelerated *in vitro* measurements with reduced ATP concentrations. This is due to the previously described limited spatiotemporal precision of centroid localization. *In vitro* measurements include the labeling of dynein with single fluorophores (Qiu et al., 2012), FluoroCubes (Niekamp et al., 2021), or quantum dots (DeWitt et al., 2012; Elshenawy et al., 2019; Reck-Peterson et al., 2006). Conversely, live cell measurements of dynein at physiological ATP concentrations have been conducted using labels that are considerably larger than the dynein motor complex (Fig. 2.3B), including upconverting nanoparticles (Peng et al., 2024), peroxisomes that are multiply tagged with GFP (Kural et al., 2005), and aggregates of quantum dots (Nan et al., 2005). As these approaches did not label the dynein directly, it is challenging to extrapolate findings regarding cargo movement to dynein itself.

To address how mammalian dynein steps in live neurons and to contribute to the answering of some of the outstanding mechanistic questions that have been raised, a tag that is substantially smaller than the dynein motor complex is utilized to directly, specifically and endogenously label dynein at three different sites (Fig. 2.3C). Resolving potential dynein stepping at physiological ATP concentrations is only feasible through the use of MINFLUX tracking, which necessitates markedly fewer detected photons to achieve single-digit nanometer/millisecond spatiotemporal precision, as previously outlined.

3 Materials and Methods

3.1 Sample Preparation

3.1.1 Preparation of Plasmids for Dynein Tagging

The following section outlines the preparation of several plasmids that are utilized for the tagging of dynein. These plasmids are employed in two distinct methods: transient overexpression and CRISPR/Cas9-mediated knock-in. In the former approach, the plasmids are introduced into neurons to overexpress a distinct dynein subunit. In the latter approach, the plasmids are integrated into the genome of primary neurons, thus tagging the endogenous dynein. Table 3.1 provides an overview of all generated plasmids.

As a preliminary step in the design of the plasmids for transient overexpression, a plasmid containing the full-length mouse cytoplasmic dynein 1 intermediate chain 2 isoform 2C (DIC2C) tagged with enhanced GFP (EGFP) at the N-terminus (GFP-DIC2C) (King et al., 2003) was obtained from Addgene (Plasmid #51409) and served as a template. The integrity of the GFP-DIC2C plasmid was confirmed by Sanger sequencing (Eurofins Genomics).

All plasmids for CRISPR/Cas9-mediated knock-in are based on the CRISPR/Cas9 knock-in template vector pORANGE (Willems et al. (2020), Addgene #131471). Target sequences for the rat genome were generated based on scoring algorithms (Doench et al., 2016; Hsu et al., 2013) provided by the CRISPR design tool from Benchling. To tag the N-terminus of the DIC, a well-scoring target sequence near the 5′ end of exon 1 of dynein cytoplasmic 1 intermediate chain 2 (*Dync1i2*) was selected. Similarly, for the purpose of tagging the N-terminus of the DHC, which is referred to as the dynein tail, a target sequence near the 5′ end of exon 1 of dynein cytoplasmic 1 heavy chain 1 (*Dync1h1*) was selected. The tagging of the dynein head, which is formed at the C-terminus of the DHC, is facilitated by the selection of a target sequence at the 3′ end of *Dync1h1*.

Plasmid SNAP-DIC2C for Overexpression

To replace the EGFP-tag of the GFP-DIC2C plasmid by a SNAP-tag, the GFP-DIC2C plasmid was used as a backbone and another plasmid containing a SNAP26m-tag as a template for the SNAP-tag. First, the SNAP-tag sequence was amplified by a polymerase chain reaction (PCR) and purified using the NucleoSpin Gel and PCR Clean Up kit (#740609, Macherey Nagel) according to manufacturer's instructions. Next, the backbone and the purified SNAP-tag insert were digested separately by the restriction enzymes AgeI and BglII (#FD1464 & #FD0083, Thermo Fisher Scientific). Backbone and insert were then ligated using the

Table 3.1 | Overview of plasmids used for tagging dynein in living cells

Plasmid Name	Description	Reference
GFP-DIC2C	EGFP tagged (N-terminus) full-length DIC2C for transient overexpression	Addgene #51409 King et al. (2003)
SNAP-DIC2C	SNAP26m tagged (N-terminus) full-length DIC2C for transient overexpression	This thesis
pOrange Vector	Empty backbone template for CRISPR/Cas9 (ORANGE) knock-in constructs	Addgene #131471 Willems et al. (2020)
pO-GFP-Dync1i2	CRISPR/Cas9-mediated tagging of *Dync1i2* with EGFP (N-terminus)	This thesis
pO-SNAP-Dync1i2	CRISPR/Cas9-mediated tagging of *Dync1i2* with SNAPf (N-terminus)	This thesis
pO-SNAPco-Dync1i2	CRISPR/Cas9-mediated tagging of *Dync1i2* with codon-optimized SNAPf (N-terminus)	This thesis
pO-Halo-Dync1i2	CRISPR/Cas9-mediated tagging of *Dync1i2* with HaloTag7 (N-terminus)	This thesis
pO-EOS-Dync1i2	CRISPR/Cas9-mediated tagging of *Dync1i2* with codon-optimized mEOS4b (N-terminus)	This thesis
pO-GFP-Dync1h1	CRISPR/Cas9-mediated tagging of *Dync1h1* with monomeric EGFP (mEGFP) (N-terminus, dynein tail)	This thesis
pO-Halo-Dync1h1	CRISPR/Cas9-mediated tagging of *Dync1h1* with HaloTag7 (N-terminus, dynein tail)	This thesis
pO-Dync1h1-GFP	CRISPR/Cas9-mediated tagging of *Dync1h1* with mEGFP (C-terminus, dynein head)	This thesis
pO-Dync1h1-Halo	CRISPR/Cas9-mediated tagging of *Dync1h1* with HaloTag7 (C-terminus, dynein head)	This thesis

T4 DNA Ligase (#EL0011, Thermo Fisher Scientific). The ligated plasmid and a negative control without SNAP-tag insert were transformed into One Shot TOP10 *Escherichia coli* (#C404003, Thermo Fisher Scientific) and plated onto LB agar plates with kanamycin. On the next day, five single colonies of the ligated plasmid were inoculated into 4 mL LB medium with 0.1 % kanamycin and incubated overnight. The five clones were then isolated using the QIAprep Spin Miniprep Kit (#27106X4, Qiagen) following manufacturer's instructions and evaluated by Sanger sequencing (Eurofins Genomics). Finally, a clone with correct sequence was amplified using the GeneJET Endo-Free Plasmid Maxiprep Kit (#K0861, Thermo Fisher Scientific) according to manufacturer's instructions to obtain the SNAP-DIC2C plasmid.

Plasmid pO-GFP-Dync1i2 for CRISPR/Cas9-Mediated Knock-in

As the N-terminal sequence of all three isoforms of the rat DIC is identical, endogenous tagging of DIC tags all three isoforms and not just one isoform, as is the case with overexpression. Note also that the tagging functions for both Rattus norvegicus genomes, Rnor 6.0 and mRatBN7.2, due to sequence identity in the respective genomic sequence segment. Since the ORANGE system requires cutting within the exon, a 20 bp long target sequence (5′-TAATTCACTTTTGTCTGACA-3′) corresponding to the Cas9 PAM sequence (5′-NGG-3′) was chosen that binds only 1 bp downstream of the start codon of *Dync1i2*, ensuring minimal loss of genomic information. Forward and reverse target sequence oligos were synthesized by Integrated DNA Technologies.

First, the forward target sequence was hybridized and ligated into the BbsI (#FD1014, Thermo Fisher Scientific) digested empty pOrange backbone (Addgene #131471) with a molar ratio of 1:3 (vector:insert). The donor sequence, comprising EGFP flanked by two inverse target sequence sequences, was generated in a stepwise manner. EGFP, the 3′ inverse target sequence (located downstream of EGFP), and linker sequences were generated by two consecutive PCRs. The donor sequence, comprising EGFP flanked by two inverse target sequence sequences, was generated in a stepwise manner. EGFP, the 3′ inverse target sequence (located downstream of EGFP), and linker sequences were generated by two consecutive PCRs. In the first PCR, pORANGE GFP-Actb KI #2 (Addgene #139666) served as a template to amplify EGFP. In the second PCR, additional primers were employed to amplify the PCR product of the first PCR, thereby introducing additional restriction sites. To insert the EGFP tag into the backbone, the second PCR product and the pORANGE-target-sequence construct were digested with BamHI and XbaI (#ER0051 & #ER0682, Thermo Fisher Scientific) and ligated with T4 ligase (#EL0011, Thermo Fisher Scientific). Subsequently, the 5′ inverse target sequences (situated upstream of EGFP) with NheI/HindIII compatible ends were annealed and ligated into the NheI and HindIII (#ER0972 & #ER0505, Thermo Fisher Scientific) digested second intermediate construct. Following bacterial transformation, colonies containing the correct pO-GFP-Dync1i2 construct were identified by sequencing (Eurofins Genomics) and purified using the GeneJET Endo-Free Plasmid Maxiprep Kit (#K0861, Thermo Fisher

Scientific).

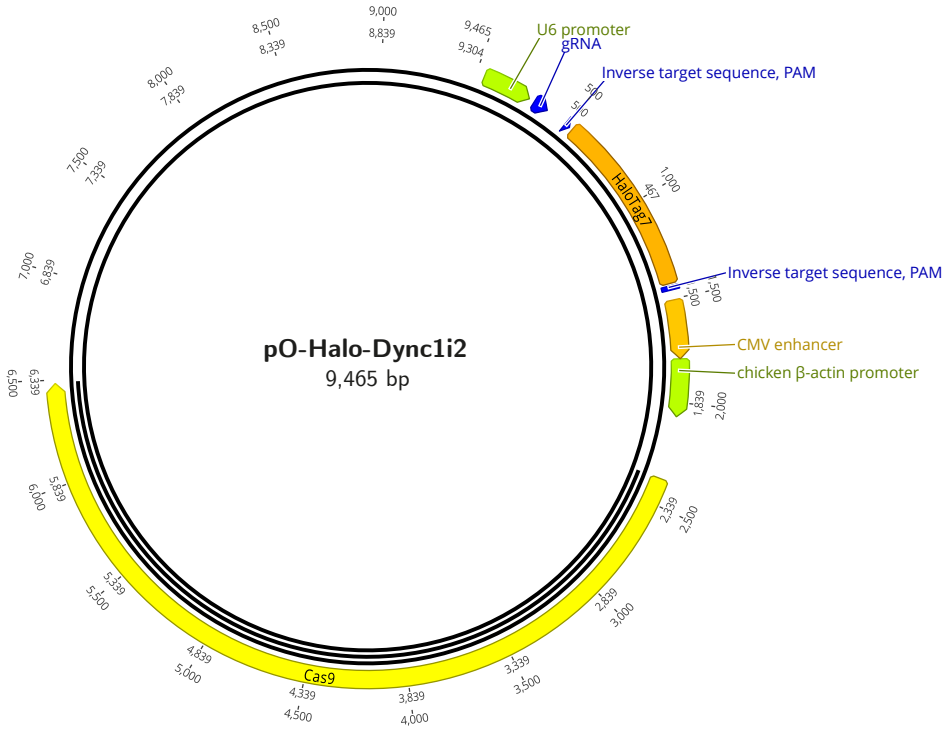

Figure 3.1 | CRISPR/Cas9 knock-in plasmid
The plasmid map shown here is used to insert a HaloTag7 sequence at the 5′ end of the rat Dync1i2 gene, thereby tagging the N-terminus of the endogenous DIC with a HaloTag7. The other CRISPR/Cas9 knock-in plasmids are similar to the one shown here.

Plasmids pO-Halo-Dync1i2, pO-EOS-Dync1i2, pO-SNAP-Dync1i2, and pO-sNAPco-Dync1i2 for CRISPR/Cas9-Mediated Knock-in

Based on the pO-GFP-Dync1i2 plasmid, four additional plasmids were prepared for tagging of the endogenous DIC. These plasmids contain a SNAPf-tag, a codon-optimized SNAPf-tag, a HaloTag7, and a codon-optimized mEOS4b-tag. The codon optimization of the rat sequence was conducted using the Codon Optimization Tool of Integrated DNA Technologies. To prevent the potential formation of hairpins during synthesis, nine codons in the SNAPf sequence were modified in the codon-optimized version.

First, the pO-GFP-Dync1i2 plasmid and all four inserts were digested separately with NheI-HF and KpnI-HF (#R3131S & #R3142S, NEB) to separate the backbone from the EGFP-tag by gel purification. Each insert containing the respective tag (acquired from Integrated DNA Technologies) was ligated into the pO-Dync1i2 backbone separately. Following bacterial transformation, colonies containing the correct construct were identified by sequencing (Eurofins Genomics). Finally, for each construct, a clone with the correct sequence was

purified using the GeneJET Endo-Free Plasmid Maxiprep Kit (#K0861, Thermo Fisher Scientific) to obtain the plasmids pO-SNAP-Dync1i2, pO-SNAPco-Dync1i2, pO-Halo-Dync1i2, and pO-EOS-Dync1i2. Figure 3.1 shows the plasmid map for pO-Halo-Dync1i2, representative for the other CRISPR/Cas9 knock-in plasmids.

Plasmids pO-GFP-Dync1h1 and pO-Halo-Dync1h1 for CRISPR/Cas9-Mediated Knock-in

The initial step in the preparation of the pO-GFP-Dync1h1 plasmid was identical to that employed in the preparation of pO-GFP-Dync1i2. However, in this instance, different oligonucleotides were hybridized to target *Dync1h1* with the integration site directly following the start codon (5′-CTTCCGCGGATCCGCCATGT-3′). The donor sequence containing mEGFP tag flanked by two inverse target sequences was generated again by PCR and inserted into the pORANGE template by restriction digestion with MunI and HindIII (#R3589 & #R3104 NEB), dephosphorylation, and ligation. To prepare the pO-Halo-Dync1h1, a subcloning step was employed. The plasmid pO-GFP-Dync1h1 and an HaloTag7 insert with corresponding restriction sites (obtained from Integrated DNA Technologies) were digested with SalI and NheI (#R3138 & #R3131, NEB) in order to replace the mEGFP with the HaloTag7 fragment. Following bacterial transformation, colonies containing the correct constructs were identified by sequencing (Eurofins Genomics) and purified using the GeneJET Endo-Free Plasmid Maxiprep Kit (#K0861, Thermo Fisher Scientific).

Plasmids pO-Dync1h1-GFP and pO-Dync1h1-Halo for CRISPR/Cas9-Mediated Knock-in

The target sequence (5′-CCTCGAAGCTTCTATGAGCG-3′) for the knock-in of the tags mEGFP and HaloTag7 close to the stop codon of the *Dync1h1* gene (exon 78) was selected to ensure that as few amino acids as possible at the C-terminus of the encoded DHC are cleaved. The corresponding plasmids, pO-Dync1h1-GFP and pO-Dync1h1-Halo, were generated in a two-step procedure using restriction enzymes. First, the ordered target sequence oligomers, containing the target sequences, were hybridized and ligated into the BbsI-digested (#FD1014, Thermo Fisher Scientific) pORANGE vector. Following bacterial transformation, colonies containing the correct intermediate construct were identified by sequencing (Eurofins Genomics) and subsequently digested with XbaI and SalI (#ER0682 & #R3138, Thermo Fisher Scientific). In the second step, both tags to be inserted into the plasmids were amplified from previous plasmids by PCR. The primers were designed in such a way that target sites were inserted as the reverse complement of the genomic target sequence on both sides of the amplified tag inserts. Finally, the amplified tags flanked by the inverse target sequences were ligated into the digested intermediate construct, and colonies containing the correct constructs from colony-PCR were purified using the GeneJET Endo-Free Plasmid Maxiprep Kit (#K0861, Thermo Fisher Scientific).

3.1.2 Preparation of Primary Hippocampal Neurons and PC12 Cells

Primary hippocampal cultures were obtained from Wistar rats at postnatal days P0 or P1, as previously described (Lukinavičius et al., 2014). One day before dissection, autoclaved ⌀18 mm coverslips were were put in 12-well cell culture plates. For each coverslip, 50 µL of a gold nanoparticle solution (#GC150, BBI Solutions) was centrifuged and diluted to 150 µL in phosphate-buffered saline per coverslip, with which the coverslips were coated. After a minimum of three hours, the remaining liquid was aspirated. Subsequently, the coverslips were coated with 100 µg mL^{-1} poly-L-ornithine (#P3655, Sigma-Aldrich) and 1 µg mL^{-1} laminin (#354232, Corning).

For transient overexpression experiments, 150×10^3 primary hippocampal neurons per coverslip were plated on coated coverslips and maintained in an incubator (37 °C, 5% CO_2, 95% rH) in Neurobasal medium (#21103049, Gibco) supplemented with 2% B27 serum-free supplement (#17504044, Gibco), 1% GlutaMAX (#35050061, Gibco) and penicillin/streptomycin (#25030, Biochrom) at a concentration of 100 U mL^{-1} or 100 µg mL^{-1}, respectively. The medium was exchanged 1 h to 2 h after seeding. After one day in culture, 5 µM Ara-C (#C1768, Sigma-Aldrich) was added to the cells. Neurons were transfected after five to seven days in culture using 500 ng plasmid DNA per coverslip and 2 µL Lipofectamine 2000 (#11668500, Invitrogen) diluted in Opti-MEM (#31985070, Thermo Fisher Scientific). Half of the culture medium was transferred out of the well and stored at 37 °C. After 1 h incubation, the transfection mixture was discarded and the stored cell medium was added again.

For CRISPR/Cas9-mediated tagging experiments, 200×10^3 neurons per coverslip were electroporated using 200 ng of the CRISPR/Cas9 knock-in plasmid via the Neon transfection system (#MPK10096 and #MPK5000, Thermo Fisher Scientific), utilizing a voltage of 1400 V and three pulses of 10 ms duration. The primary hippocampal neurons were maintained in an incubator in supplemented Neurobasal medium (#21103049, Gibco). The medium was exchanged after one day in culture.

The PC12 cell line (#C0032002, AddexBio) was utilized for the purpose of comparing the dynein movement to living neurons. The cells were seeded at a density of 50×10^3 per ⌀18 mm coverslip in a 12-well plate. After two days, the cells were transfected using a transfection mixture. First, 2 µg of plasmid was incubated for five minutes at room temperature in 200 µL of Opti-MEM (#31985070, Thermo Fisher Scientific), then 4 µL of Turbofect (#R0532, Thermo Fisher Scientific) was added, followed by a 20-minute incubation at room temperature. The mixture was then added to the well in dropwise fashion. After a period of five days, the cell density was assessed and, should it be deemed suitable for imaging, the expressed dynein was labeled with a cell-permeable fluorophore, as outlined in section 4.1.4. Following this, the cells were washed twice and imaged prewarmed in FluoroBright DMEM (#A1896701, Thermo Fisher Scientific).

3.1.3 Genomic DNA Isolation

Correct incorporation of respective tags into the genome of cultured neurons was assessed by isolating the genomic DNA of electroporated neurons and subsequent confirmation by Sanger sequencing. 1.2×10^6 to 1.8×10^6 neurons were electroporated with each of these plasmids: pO-GFP-Dync1i2, pO-SNAP-Dync1i2, pO-SNAPco-Dync1i2, pO-Halo-Dync1i2, pO-EOS-Dync1i2, pO-GFP-Dync1h1, pO-Halo-Dync1h1, pO-Dync1h1-GFP, and pO-Dync1h1-Halo. The genomic DNA was isolated using the GenElute Mammalian Genomic DNA Miniprep Kit (#G1N70-1KT, Sigma-Aldrich). A PCR was performed with primers that bind in the respective genes and tagging sequences. As an expample, the expected lengths of the Dync1i2 PCR products after gel electrophoresis are shown in figure 3.2A (all other electrophoresis gels are presented in figure 4.2). The PCR products were purified using the NucleoSpin Gel and PCR Clean Up kit (#740609, Macherey Nagel). The specificity of all five tags was confirmed by Sanger sequencing (Eurofins Genomics) of respective purified PCR products from isolated genomic DNA (Fig. 3.2B).

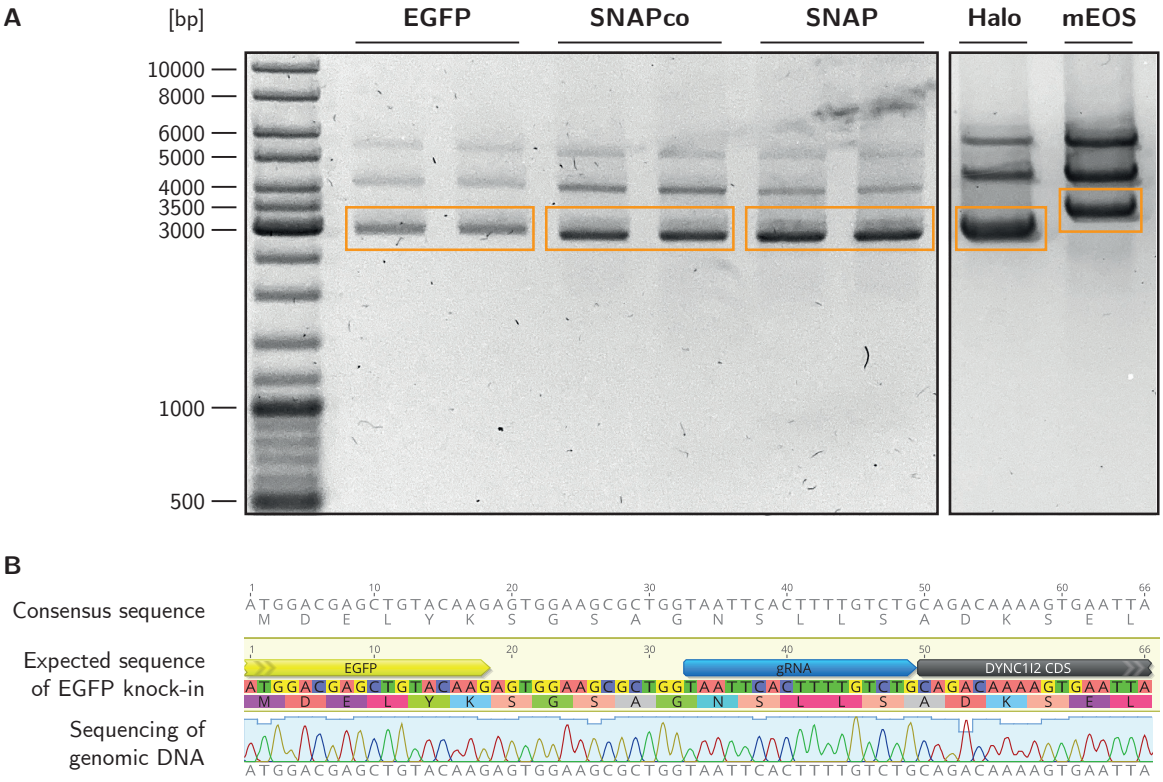

Figure 3.2 | Genomic DNA Isolation
(A) Agarose gel with PCR products of isolated genomic DNA from electroporated neurons. Orange boxes indicate expected PCR product lengths after CRISPR/Cas9-mediated tagging of dynein: EGFP (3022 bp), SNAPco (2929 bp), SNAP (2929 bp), Halo (2833 bp), mEOS (3199 bp). **(B)** Excerpt from the sequence using the example of pO-GFP-Dync1i2 electroporation in Geneious Prime (version 2023.2.1, Biomatters). The consensus sequence shows full agreement between the expected genomic sequence with knock-in tag and the sequencing of the isolated genomic DNA.

3.1.4 Fluorescent Labeling of Dynein in Living Neurons and PC12 Cells

Transfected or electroporated neurons were incubated with different cell-permeable fluorophores after six to nine days in culture to label dynein in living neurons. An overview of all fluorophores used in this thesis are listed in Table 3.2. For neurons that expressed SNAP-tagged dynein, a fluorophore conjugated to O^6-benzylguanine was used and for Halo-tagged dynein, a fluorophore conjugated to chloroalkane, respectively. In some experiments, microtubules are stained alongside dynein with a fluorophore conjugated to a taxane derivative that specifically binds tubulin.

For the labeling, the fluorophore was diluted in medium to the desired concentration. The fluorophore mixture was added dropwise to the well to distribute the fluorophore evenly. Neurons were incubated for several minutes with the fluorophore as indicated at each experiment right before imaging. Coverslips were washed with prewarmed artificial cerebrospinal fluid (ACSF) solution (27 mM Hepes pH 7.4, 126 mM NaCl, 2.5 mM KCl, 2.5 mM $CaCl_2$, 1.3 mM $MgCl_2$, 30 mM glucose) and transferred into a magnetic imaging chamber (Chamlide CMB, Live Cell Instrument) filled with ACSF for imaging.

Table 3.2 | Overview of fluorophores used for live-cell imaging
The wavelengths of excitation and emission maxima are indicated as Ex/Em.

Fluorophore	Ligand	Ex/Em [nm]	Reference or Supplier
Oregon Green	HaloTag	496/516	Promega, #G2802
LIVE 510	SNAP-tag	498/529	abberior, #LV510-0145
LIVE 510	Tubulin	498/529	abberior, #LV510-0141
BioTracker 488	Tubulin	500/515	Sigma-Aldrich, #SCT142
R110 Direct	HaloTag	502/527	Promega, #G3221
505-Star	SNAP-tag	504/532	NEB, #S9103S
NL19	HaloTag	514/533	Lardon et al. (2021)
JF549	HaloTag	549/571	Promega, #GA1110
MaP555	HaloTag	555/580	Wang et al. (2020)
580CP	SNAP-tag	582/607	Butkevich et al. (2018)
580CP	HaloTag	582/607	Butkevich et al. (2016)
610CP	SNAP-tag	609/634	Butkevich et al. (2018)
610CP	HaloTag	609/634	Butkevich et al. (2016)
LIVE 610	SNAP-tag	611/636	abberior, #LV610-0145
SiR	SNAP-tag	641/662	Lukinavičius et al. (2013)
JF646	HaloTag	646/664	Promega, #GA1120
JF646	SNAP-tag	646/664	Tocris, #1811539-59-9
JFX650	HaloTag	650/667	Promega, #HT1070
SiR	Tubulin	652/674	Lukinavičius et al. (2014)

3.2 Microscope Setups

3.2.1 Widefield Microscopy Setup

A widefield multiplexing microscopy setup (Fig. 3.3) was arranged for performing dynamic measurements of biological samples with a large field of view and multiple excitation lasers.

Four excitation laser lines provide the ability to measure fluorescent probes at different wavelengths within a large portion of the visible spectrum. The excitation lasers comprise a 640 nm 500 mW single-frequency diode laser (05-01 series Cobolt Bolero, HÜBNER Photonics), a 570 nm 1500 mW fiber laser (2RU-VFL-P-1000/1500-570, MPB Communications), a 532 nm 500 mW solid state laser (gem 532, Laser Quantum), and a 488 nm 70 mW diode laser (LBX-488, Oxxius). A 405 nm laser with 100 mW (LBX-405, Oxxius) and a 375 nm laser with 16 mW (CUBE 375-16C, Coherent) can be used to activate fluorescent probes by UV-light.

The beam is expanded by a $20\times/0.8$ apochromatic objective lens (440640-9903, ZEISS) in combination with an achromatic lens ($f_\mathrm{E} = 120\,\mathrm{mm}$). The beam can be moved laterally using a linear stage controlled by a motorized actuator (Z825B & KDC101, Thorlabs) and finally focused by the TIR focusing lens ($f_\mathrm{T} = 300\,\mathrm{mm}$) onto the back focal plane (BFP) of the oil immersion $100\times/1.5$ objective lens (UPLAPO100XOHR, Olympus). By translating the beam towards the edge of the back focal plane of the objective lens, the outgoing beam is tilted which is necessary for HILO and TIR fluorescence microscopy. The resulting diameter (indicated as full width at half maximum, FWHM) of the illuminated area at the sample plane d_s can be roughly estimated by

$$d_\mathrm{s} = d_\mathrm{b} \cdot \left(\frac{f_\mathrm{O}}{f_\mathrm{T}}\right) \approx 60\,\mu\mathrm{m} \tag{3.1}$$

with the expanded beam diameter (FWHM) at the TIR lens $d_\mathrm{b} \approx 10\,\mathrm{mm}$ (depending on the respective laser line), the objective focal length $f_\mathrm{O} = 180\,\mathrm{mm}/100 = 1.8\,\mathrm{mm}$ and the focal length of the TIR lens ($f_\mathrm{T} = 300\,\mathrm{mm}$).

A rapidly switchable acousto-optic tunable filter (AOTF) (nC-TN-1001, AA Opto Electronic) is used to deflect the unwanted part of the laser light and transmit only the desired part. By using the AOTF, it is possible to quickly switch between different excitation laser wavelengths and enable multiplexed imaging. A custom LabVIEW 2020 (National Instruments) program controls all components of the setup and synchronizes the alternate switching of the excitation lasers with the camera frames so that only one excitation laser wavelength is illuminating the sample in each successive frame. The software contains two acquisition modes, a fast one with single excitation and a slower one with the possibility for alternated multiplexing.

The microscope body (IX83, Olympus) is equipped with an auto-focus unit (IX3-ZDC, Olympus) that also compensates drift in the z-direction; a microscope scanning stage (SCAN IM 120x80, Märzhäuser Wetzlar) that can hold microscope slides or magnetic imaging cham-

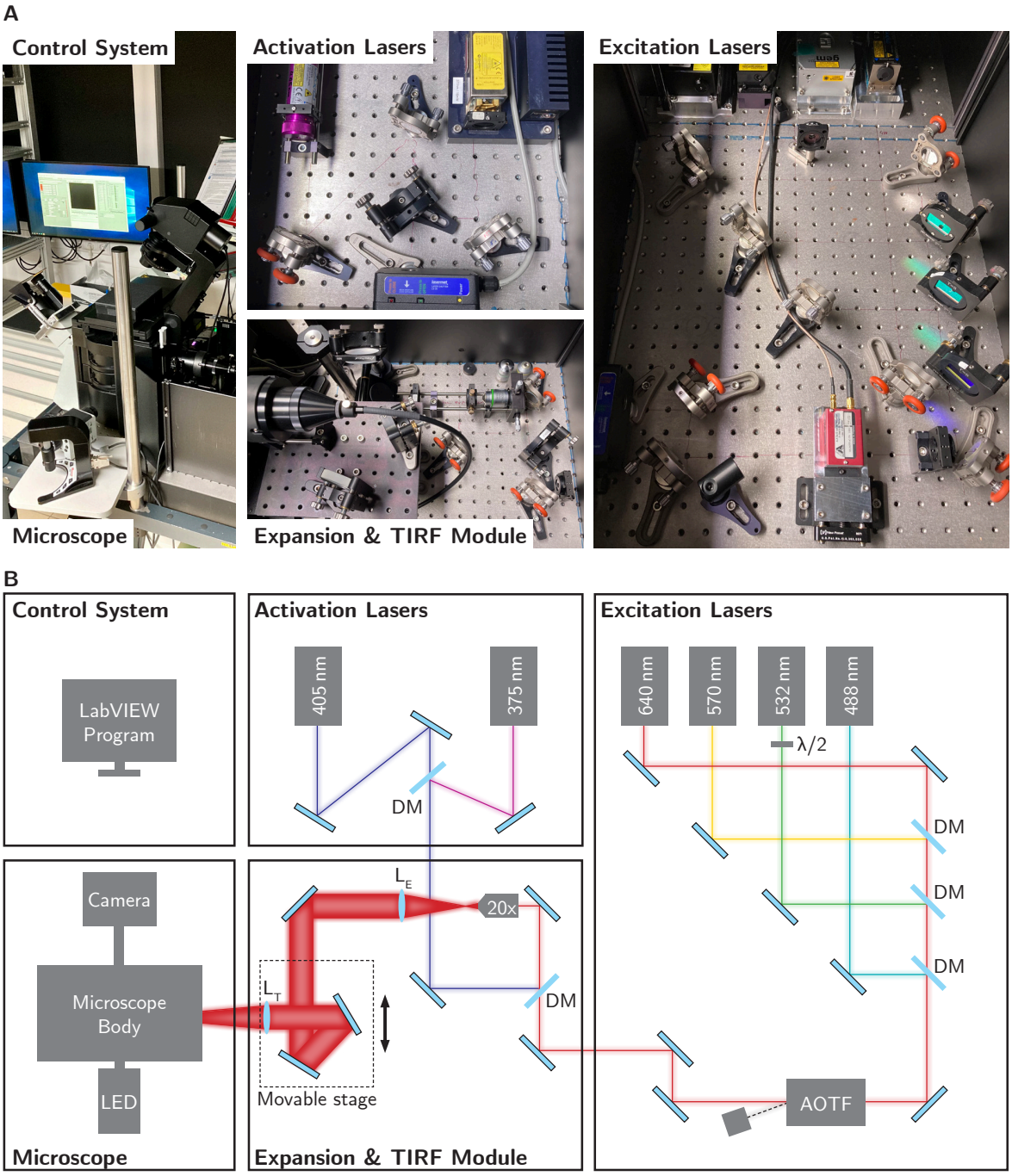

Figure 3.3 | Overview of the custom-built widefield microscopy setup
(A) Photos of the custom-built widefield microscopy setup. **(B)** The setup comprises four excitation laser lines and two activation laser lines that are directed onto one beam path using different mirrors and dichroic mirrors (DM). The desired excitation lasers can be selected and mulitplexed by a rapidly switchable AOTF. The beam is expanded by a $20\times/0.8$ apochromatic objective lens in combination with an achromatic lens (L_E). To tilt the beam angle at the microscope objective lens, the laser beam can be shifted towards the outside of the BFP of the objective lens by a movable stage. The beam is focused onto the BFP by an achromatic TIR focusing lens (L_T). The emission filter and dichroic mirror inside the microscope body are selected according to the excitation wavelengths. An additional LED lamp can be used to illuminate the sample while using the eyepieces. The sample is fixed on a microscope stage that can be moved in the x- and y-directions. Emitted light from the illuminated sample is directed on an EMCCD camera. A custom-written LabVIEW software controls the different devices and saves the camera images.

bers; and two mirror turrets (IX3-RFACA, Olympus), one for the respective excitation/emission filters and corresponding dichroic mirrors of the broad spectrum LED lamp (XT720L, Excelitas Technologies) and the other for the respective emission filters and dichroic mirrors of the excitation laser wavelengths. For multiplexed imaging, two quadband filter sets are available, one for alternating excitation by 405, 488, 532, and 640 nm wavelengths (F72-866 & F73-866S, AHF analysentechnik) and the other for alternating excitation by 405, 488, 570, and 640 nm wavelengths (F72-832 & F73-832S, AHF analysentechnik).

Emitted light from the sample is directed through a 1.6× magnifier onto a back-illuminated electron multiplying charge-coupled device (EMCCD) camera (Andor iXon^{EM}+ DU-897D-CSO-BV, Oxford Instruments) with 512×512 pixels and a pixel size of 16 µm. Consecutive frames are shown in real-time within the LabVIEW program and saved as a 14-bit TIFF stack on the hard drive of the PC.

The setup was aligned on a regular basis. For this purpose, all four excitation laser beams were first aligned to a common beam axis. Both activation laser beams were also aligned to the same beam axis. By tuning the frequencies of the AOTF, the main maximum for each wavelength with the highest transmitted intensity was identified. A shearing interferometer was used to adjust the expansion lens L_E to obtain a collimated beam. Subsequently, the central position of the movable stage was determined, and it was ensured that the beam was centered and perpendicular to the BFP using a pinhole with a connected crosshair reticle. The TIR lens was then adjusted to focus the beam on the BFP, ensuring that the beam diameter was as small and circular as possible (Fig. 3.4A). If the beam was defocused, a stretched beam pattern would result due to astigmatism in one or a perpendicular direction (Fig. 3.4B). Lastly, the camera position was centered.

Finally, the aligned setup was calibrated. The actual intensity in the sample plane was determined for each excitation and activation wavelength, which depends on the respective laser power and beam diameter. To determine the actual laser power P in the BFP, a power meter was used to measure the laser beams at different output powers in the BFP and a corresponding conversion factor was determined. Depending on the wavelength, the transmittance of the objective lens is also taken into account. Assuming a Gaussian beam profile, the mean $FWHM$ of the beam is calculated from the 2D Gaussian fit at different positions of a fluorescent bead sample (TetraSpeck Microspheres 100 nm, Invitrogen). The beam intensity for each laser wavelength at the sample plane is then calculated.

The effective pixel size in the sample plane is expected to be 100 nm using the 100× objective lens and an additional 1.6× magnification. A slide with an 1 µm grating was used to determine the actual pixel size. Using a line profile (Fig. 3.4C), the intensity was plotted along the camera pixels (Fig. 3.4D). By means of the MATLAB function *findpeaks*, the peaks were identified and the mean distance between the respective neighboring peaks was calculated to $\overline{px} = (10.0 \pm 0.5)$. With an assumed grid spacing of $d_{\text{grid}} = (1000 \pm 10)$ nm an effective pixel

size of $d_{\mathrm{px}} = (100 \pm 5)\,\mathrm{nm}$ was calculated as follows:

$$d_{\mathrm{px}} = \frac{d_{\mathrm{grid}}}{\overline{px}} = 100\,\mathrm{nm} \quad \text{with} \quad \Delta d_{\mathrm{px}} = \sqrt{\left(\frac{\Delta d_{\mathrm{grid}}}{\overline{px}}\right)^2 + \left(\frac{d_{\mathrm{grid}} \cdot \Delta\overline{px}}{\overline{px}^2}\right)^2} = 5\,\mathrm{nm} \tag{3.2}$$

Consequently, the image size of a camera frame is $51.2 \times 51.2\,\mu\mathrm{m}^2$.

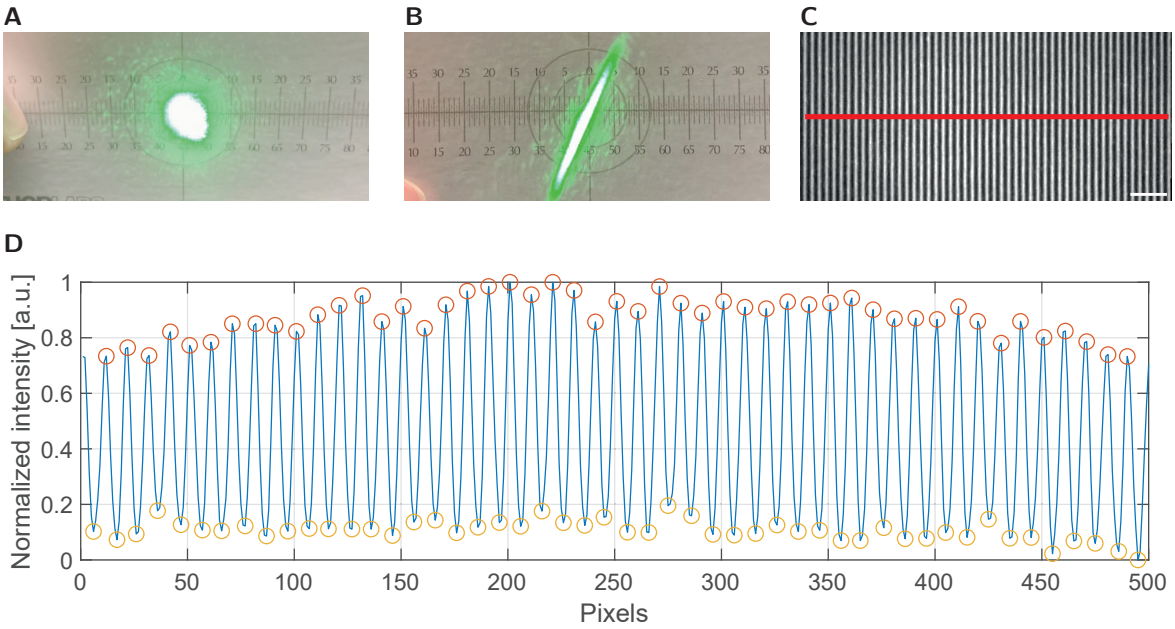

Figure 3.4 | Calibration and alignment of widefield microscopy setup
(A) Beam profile of aligned setup shown a few centimeters above the objective lens. Note that the slight asymmetry of the beam profile results from the inclination of the hand-held paper. **(B)** Beam profile of misaligned expansion or TIR lens. **(C)** Cropped camera image of a 1 µm grating. Scale bar: 50 px. **(D)** Line profile (red line in (C)) showing the normalized intensity and identified peaks.

3.2.2 MINFLUX Setup

MINFLUX tracking experiments were conducted using a commercially available MINFLUX system (Abberior Instruments) (Schmidt et al., 2021), which includes a motorized inverted microscope (IX83, Olympus) with a 100×/1.4 oil-immersion objective lens (UPLSAPO100XO, Olympus). The microscope is equipped with excitation laser lines of 640, 561 and 488 nm wavelengths and an LED lamp (XT720L, Excelitas) with corresponding filter sets. MINFLUX detection was achieved by employing two avalanche photodiodes in the spectral ranges of 650 nm to 685 nm and 685 nm to 720 nm wavelength, with the photon counts of the two avalanche photodiodes being summed. Confocal images are acquired in the spectral ranges of 500 nm to 550 nm and 580 nm to 630 nm wavelength, respectively. The reflection image of the gold nanoparticles fixed on the cover glass is used for active stabilization, resulting in a residual sample drift of typically less than 1 nm (mean square displacement) in all directions.

The Imspector software is used to operate the entire setup (version 16.3.15631-m2205, Abberior Instruments). The setup was fine-tuned the morning before the experiments by centering the beams of the different lasers and verifying the quality of the intensity minimum (zero) of the excitation laser.

3.3 Data Acquisition

For the purpose of tracking experiments, a fresh sample was prepared after a period of six to nine days in culture, as previously described. The identification of a CRISPR-positive neuron was achieved through the use of dynein labeled with a cell-permeable fluorophore or dynein tagged with EGFP. Using the eyepieces and LED illumination increased the speed of the identification process. The morphological characteristics of axons, namely their longer and constantly narrow extension and smoother appearance compared to dendrites (Cason et al., 2023), were employed to identify axons. In instances where the axon was not readily discernible, an alternative cell was sought.

3.3.1 MINFLUX Tracking Measurements

Once an axon of a CRISPR-positive neuron had been identified, a series of ROIs along the axon were selected for MINFLUX tracking. To achieve a localization precision well below 8 nm, which is the expected step size of dynein, and a temporal resolution well below 1 ms, to avoid missing steps, the parameters listed in Table 3.3 were set in the localization procedure. According to Equation 2.6, a minimum of 75 photons per localization is required to achieve approximately 3 nm localization precision at a TCP diameter of $L = 75\,\text{nm}$. The pattern dwell time was set to 200 µs with at least three repetitions, which results in a mean photon count rate of 125 kcps needed to obtain 75 photons per localization in 600 µs. In the course of test experiments, these photon rates were frequently achieved by setting the laser power of the 640 nm excitation laser to 135 µW (measured at the periscope). A confocal detection pinhole size of 0.93 AU was used.

In the initial phase of the MINFLUX localization procedure, the ROI is continuously scanned, and once a predefined photon threshold is reached, the specified iterative MINFLUX localization procedure (Table 3.3) is initiated. The diameter L of the TCP is gradually reduced while the laser power is incrementally increased. For MINFLUX tracking, the final iteration step is repeated until the maximum center frequency ratio (CFR) (Schmidt et al., 2021) is surpassed or the detection signal is lost completely. This ultimately yields a MINFLUX trace of successive localizations.

3.3.2 Widefield Measurements

For widefield measurements in section 4.2, several ROIs of dimension $51.2 \times 51.2\,\mu\text{m}^2$ were successively selected along the axon. To achieve the highest frame rate for widefield dynein

Table 3.3 | MINFLUX localization procedure
The minimum number of photons detected (photon count) refers to the overall dwell time of the pattern, for example, $3 \times 200\,\mu s$ for the final iteration. Should the minimum number of photons not be reached during a pattern, the entire pattern is repeated until the minimum number of photons is achieved. This may result in an extended time interval to the next localization.

Iteration	**1**	**2**	**3**	**4**
TCP mode	Prescan	Hexagon	Hexagon	Hexagon
TCP diameter L (nm)	284	302	151	75
TCP dwell time (µs)	50	50	50	200
TCP repeat	1	1	1	3
Minimum photon counts	40	20	10	75
Background threshold (kcps)	15	30	30	40
Maximum CFR	–	0.5	–	0.8
Laser power multiplication	1	1	2	3

tracking, microtubules and dynein were not simultaneously imaged in multiplexed mode but rather successively. First, stained microtubules were imaged with the 488 nm excitation wavelength at a focal intensity of $92\,W/cm^2$ and near TIRF conditions. To avoid channel bleed-through, the stained microtubules were then bleached. Subsequently, in the same ROI, movies were recorded with the 532 nm excitation wavelength at a focal intensity of $92\,W/cm^2$ and an exposure time of 100 ms for at least one minute. For recordings in other sections, other laser intensities may have been used, which are indicated in the text.

3.4 Data Analysis and Processing

In the figures presented in the subsequent chapter, the symbol 'n' represents the number of data points, while the symbol 'N' denotes the number of independently conducted experiments.

3.4.1 Analysis of MINFLUX Measurements

Data from MINFLUX measurements were analyzed and plotted in MATLAB R2022a using custom-written scripts.

Singular Value Decomposition to Determine On-Axis Direction

The first step in the analysis of the measured MINFLUX traces was to determine the main direction of propagation of the movement. Here, one can take advantage of the fact that the shape of a processive motion of dynein along the axon corresponds approximately to a rectilinear motion and thus has a large variance in the direction of propagation and a small variance orthogonal to the direction of propagation. It is therefore reasonable to determine

the direction of propagation using a singular value decomposition (SVD). In the following, the main propagation direction is called "on-axis" and the direction orthogonal to it "off-axis".

In case of a two-dimensional measurement and an economy SVD, the centered trace matrix $\mathbf{T} \in \mathbb{R}^{2\times m}$ containing x-/y-coordinates for m consecutive localizations can be uniquely decomposed into two unitary matrices $\mathbf{U} \in \mathbb{R}^{2\times 2}$ and $\mathbf{V} \in \mathbb{R}^{m\times 2}$ and a diagonal matrix $\mathbf{\Sigma} \in \mathbb{R}^{2\times 2}$ in the following manner (Brunton and Kutz, 2019).

$$\mathbf{T} = \begin{bmatrix} t_1 & \cdots & t_m \end{bmatrix} = \underbrace{\begin{bmatrix} x_1 & \cdots & x_m \\ y_2 & \cdots & y_m \end{bmatrix}}_{\mathbf{T}\in\mathbb{R}^{2\times m}} = \mathbf{U}\mathbf{\Sigma}\mathbf{V}^\top = \underbrace{\begin{bmatrix} u_{11} & u_{12} \\ u_{21} & u_{22} \end{bmatrix}}_{\mathbf{U}\in\mathbb{R}^{2\times 2}} \underbrace{\begin{bmatrix} \sigma_1 & 0 \\ 0 & \sigma_2 \end{bmatrix}}_{\mathbf{\Sigma}\in\mathbb{R}^{2\times 2}} \underbrace{\begin{bmatrix} v_{11} & v_{12} \\ \vdots & \vdots \\ v_{m1} & v_{m2} \end{bmatrix}^\top}_{\mathbf{V}\in\mathbb{R}^{m\times 2}} \tag{3.3}$$

The economy SVD was applied to each centered trace $\mathbf{T}$ using the MATLAB function *svd*. The first column of $\mathbf{U}$ corresponds to the on-axis direction (main propagation direction) and the second column the off-axis direction. Each trace vector t_j, with $j \in [1, m]$, was subsequently rotated into the on-/off-axis coordinate system by means of an inverse linear transformation.

$$\widetilde{t_j} = \mathbf{U}^\top t_j \tag{3.4}$$

where $\widetilde{t_j}$ denotes the rotated trace vector in the on-/off-axis coordinate system.

Filter Criteria for Sorting out Non-Processive Motion Traces

Given that the dataset often comprises more than 1,000 traces, four filter criteria were employed to pre-filter the processive traces (Table 3.4). Initially, traces with fewer than 200 localizations were excluded. Subsequently, traces with a photon count rate above 300 kcps were omitted in the second filtering step. Thirdly, traces with a singular value σ_1 less than 20 nm were discarded, as these traces do not demonstrate processive motion. Finally, traces exhibiting similar variance in both axes ($\sigma_1/\sigma_2 < 3$) were excluded.

Step Finding and Segmentation

In order to evaluate the MINFLUX data without bias, the AutoStepfinder algorithm (Loeff et al., 2021) was utilized to analyze the MINFLUX traces, which does not require any assumptions about the number or size of steps. Subsequently, the traces were divided into retrograde and anterograde segments, which is defined as a processive run of at least 50 nm. As a direction reversal, the short trace segments between consecutive runs in opposite directions were defined. A segment was considered to be a pause within a processive run if it exhibited a speed below $100\,\mathrm{nm\,s^{-1}}$ for at least 100 ms.

To estimate the localization precision of a trace, the standard deviation of the distance between successive localizations was calculated as previously described (Deguchi et al., 2023).

Table 3.4 | Filter criteria for sorting out non-processive motion traces.
These filter criteria were applied in descending order to all acquired MINFLUX traces in each data set.

Filter criterion	Description	Threshold
Number of localizations	Traces were filtered out if minimum number of valid localizations per trace did not exceed the threshold.	200
Photon count rate	High photon count rates are often a sign of multiple emitters or background emissions. Traces with median photon count rate values above the threshold were thus omitted.	300 kcps
Singular value σ_1	Traces were sorted out if the first (on-axis) singular value (Eq. 3.3) did not exceed the threshold.	20 nm
Ratio of singular values σ_1/σ_2	Non-processive motion traces have similar singular values in both axes in contrast to processive ones and were therefore filtered out.	3

The uncertainty of detected step sizes was estimated based on plateau length and step size (Loeff et al., 2021).

Gaussian Mixture Model Fitting

The on-axis step distribution was fitted with a Gaussian Mixture Model using the MATLAB function *fitgmdist*. To find the optimal number of Gaussian components, the Akaike Information Criterion (AIC) was used in 1,000 fitting runs, where p is the number of estimated parameters in the model and $\hat{L}$ is the likelihood function. The repeated runs compensate for the stochastic initial conditions of *fitgmdist* which resulted in a varying number of fitted components. The optimal set of components was determined in a range from one to seven components.

$$AIC = 2p - 2\ln\hat{L} \tag{3.5}$$

Maximum Likelihood Estimation and Model Selection for Dynein Stepping

In order to select a model that best describes the dwell time distribution, which is composed of the time interval τ between successive steps, three models were fitted to the distribution. These models are a single exponential, a convolution of two exponentials with the same rate constant k, and a convolution of two exponentials with different rate constants k_1 and k_2 (Table 3.5). In order to ensure that the model fitting is independent of the data representation, maximum likelihood estimates were used by employing the MATLAB function *mle*. The model

that best describes the observed data was determined using the Akaike weights as a measure of the probability that one of the candidate models was the optimal model given the data and three competing models (Burnham and Anderson, 2002). It should be noted that the AIC (Eq. 3.5) penalizes the model with two distinct rate constants more than the other two models.

Table 3.5 | Maximum likelihood models for dynein stepping
Overview of different models for fitting the dwell time distribution, including their probability density function (PDF) and cumulative distribution function (CDF) as well as a interpretation of these models in the context of the kinetics of dynein stepping. The first model is a single exponential, the second a convolution of two exponentials with the same rate constant, the third a convolution of two exponentials with different rate constants.

PDF	CDF	Interpretation
$ke^{-k\tau}$	$1 - e^{-k\tau}$	Dynein stepping is based on a single process described by the rate constant k, i.e. consumption of one ATP per step.
$k^2\tau e^{-k\tau}$	$1 - e^{-k\tau}(1 + k\tau)$	Dynein stepping is based on two equal processes occurring successively at a rate of k, i.e. consumption of two ATPs per step.
$\frac{k_1 k_2}{k_1 - k_2}\left(e^{-k_2\tau} - e^{-k_1\tau}\right)$	$1 + \frac{k_2 e^{-k_1\tau} - k_1 e^{-k_2\tau}}{k_1 - k_2}$	Dynein stepping is based on two unequal successive processes described by rate constants k_1 and k_2, i.e. different rate constants may be assigned to slow and fast subprocesses within the ATPase cycle.

Generation of Markov Chains

Markov chains were constructed by sampling the segmented MINFLUX traces at a sampling rate of $1/k$, with $k = 90\,\mathrm{s}^{-1}$, corresponding to the inverse rate constant determined by maximum likelihood fitting of the dwell time data (Fig. 4.32B). This resulted in the generation of a varying number of time intervals, corresponding to the distinct states observed. These states included (i) processive retrograde movement (R), (ii) anterograde movement (A), (iii) a pause within retrograde movement (R→R), (iv) a pause within anterograde movement (A→A), (v) a direction reversal from retrograde to anterograde movement (R→A), and (vi) a direction reversal from anterograde to retrograde movement (A→R). The sampling rate was selected on the basis of the aforementioned segmentation, which was also performed on the single-step timescale. The transition probabilities, which constitute the transition matrix $\mathbf{P}$, were calculated as the ratio of the number of time intervals representing a transition into a subsequent state to the total number of time intervals for all transitions from the initial state. The stationary probability vector $\boldsymbol{\pi}$ was determined using MATLAB's *asymptotics* function. Traces were excluded from the Markov chain generation procedure if they contained outlier

pause or reversal times (Fig. 4.30B).

Simulation of MINFLUX Traces

MINFLUX traces (on-axis displacement versus time) were simulated using MATLAB by assuming 1,000 discrete steps of 4 nm increment at probabilities that matched the observed Gaussian Mixture Model fit (Fig. 4.35B). The dwell times between these steps were generated from a randomly exponential distribution with a decay constant of $k = 90\,\mathrm{s}^{-1}$, corresponding to the maximum likelihood fit to the experimental dwell times (Fig. 4.32B). To account for similar experimental conditions, noise was added to the trace at a level reflective of the desired localization precision.

3.4.2 Analysis of Widefield Measurements

From the movies acquired with the widefield microscope, kymographs were generated along the axon using the Fiji ImageJ (Schindelin et al., 2012) macro KymographClear (Mangeol et al., 2016). The Fourier-filtered kymograph was color-coded to highlight retrograde (orange) and anterograde (cyan) movement. With the KymographDirect program (Mangeol et al., 2016), several segments of retrograde and anterograde movement with a run length longer than 1 µm were manually traced. The exported data included the speed of the segments, which were then visualized using MATLAB.

4 Results

4.1 Establishing Endogenous Tagging of Dynein in Living Neurons

In order to be able to track dynein in living primary hippocampal neurons, it was necessary to establish and optimize the different steps of the sample preparation. The custom-built widefield microscope was utilized to assess cell viability, the number of transfected or CRISPR/Cas9-positive neurons, the expression of different protein tags, the specific binding of fluorophores, and the colocalization of dynein with microtubules.

4.1.1 Optimization of Transfection and Electroporation of Living Neurons

A series of plasmids have been designed and generated with the objective of tagging dynein at different subunits in living neurons (Table 3.1). In order to determine the optimal conditions for transfection with overexpression plasmids and electroporation with CRISPR/Cas9 knock-in plasmids, a series of conditions were tested. The optimal conditions were determined based on the number of transfected or CRISPR/Cas9-positive neurons and cell viability.

Overexpression Plasmids

For DIC overexpression in living neurons, transfection with GFP-DIC2C or SNAP-DIC2C plasmids was optimized by varying plasmid amounts in the range of 25 ng to 1000 ng and transfection times between one and seven days in culture. Optimal conditions were obtained with 500 ng plasmid per coverslip, 2 µL Lipofectamine 2000 after five to seven days in culture.

CRISPR/Cas9 Knock-In Plasmids

To optimize electroporation of living neurons, the amount of plasmid was varied between 200 ng to 400 ng, the voltage between 1200 V to 1400 V, the number of pulses between 1 and 3, and the pulse duration between 10 ms to 30 ms. The optimum was obtained with 3 pulses of 10 ms duration at 1400 V and 200 ng plasmid.

To compare transfection with electroporation, neurons were also transfected with the CRISPR/Cas9 knock-in plasmids using the optimal conditions described above. Overall, electroporation resulted in more CRISPR/Cas9-positive neurons than transfection.

4.1.2 Assessing Various Protein Tags Conjugated to Different Dynein Subunits

The subsequent step was to ascertain which protein tag is most suitable for tracking dynein in living neurons. To this end, overexpression plasmids were initially evaluated, and then the various CRISPR/Cas9 knock-in plasmids.

Overexpression of Dynein Intermediate Chain

To assess the suitability of overexpressing the tagged DIC, a subunit of the dynein motor complex, as a strategy to track dynein in living neurons, two overexpression plasmids were utilized, and living neurons were imaged with the custom-built widefield microscope. Using the optimized transfection conditions, primary hippocampal neurons were transfected with either the GFP-DIC2C plasmid or the SNAP-DIC2C plasmid. Following transfection, either the fluorescent protein EGFP (Cormack et al., 1996) or the SNAP-tag (Keppler et al., 2003; Sun et al., 2011), both conjugated to the mouse DIC2C (King et al., 2003), was overexpressed. Neurons expressing SNAP-DIC2C were additionally labeled with the cell-permeable fluorophore LIVE610-SNAP to visualize dynein. Finally, various movies of different preparations of living hippocampal neurons were recorded with the widefield microscope.

Figure 4.1A shows a widefield image of two neurons expressing EGFP-DIC2C. Three kymographs were generated along three neurites, displaying retrograde (back to the soma) and anterograde (away from the soma) movement as seen by the diagonal trajectories (Fig. 4.1B–D). This indicates that the overexpressed and tagged DIC2C was incorporated into the dynein motor complex, which moved in both directions in neurites, similar to a previous study using the same overexpression plasmid in live neurons (Guo et al., 2016).

Similarly, retrograde and anterograde movement was observed in neurites of neurons expressing SNAP-DIC2C, labeled with LIVE610-SNAP (Fig. 4.1E, F). In addition to the observation of small moving particles, elongated structures in the neurites were also labeled. These structures may correspond to non-specifically labeled mitochondria (indicated by red triangles in Fig. 4.1E).

When comparing EGFP-tagged dynein to SNAP-tagged and fluorescently labeled dynein, recordings of EGFP exhibited higher background intensity due to autofluorescence of the neurons. In contrast, LIVE610-SNAP-labeled dynein complexes exhibited a high signal-to-noise ratio and few background intensities, apart from non-specific labeling of mitochondria, due to the red laser excitation. Compared to EGFP, the high photostability of the organic fluorophore allowed for the acquisition of longer movies until the fluorophore was photobleached.

In summary, overexpression of tagged DIC, as part of the dynein motor complex, allows for the observation of bidirectional movement in neurites of living neurons. However, it is questionable whether the photostability of EGFP allows for long tracking experiments. Furthermore, it is unfavorable that LIVE610-SNAP led to non-specific labeling of mitochondria. Moreover, the consequences of expressing a dynein subunit derived from the mouse genome within neurons of another organism, in this case rats, remain uncertain.

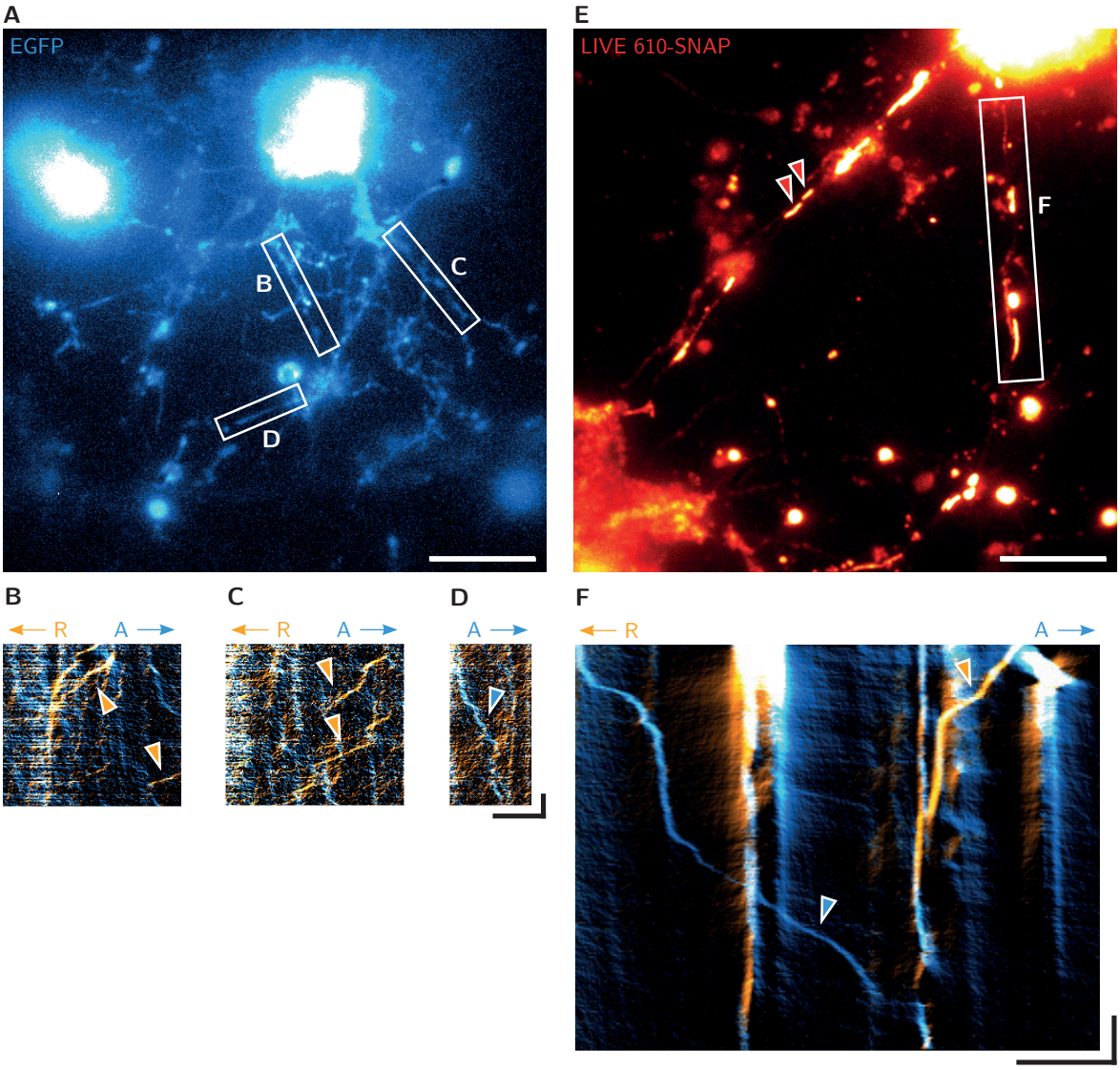

Figure 4.1 | Overexpression of dynein intermediate chain
(A) Representative maximum intensity projection of a widefield movie of living primary neurons transfected with GFP-DIC2C. White boxes indicate where the kymographs were generated. The laser intensity of the 488 nm excitation laser was 25 W/cm^2 at an exposure time of 200 ms. Scale bar: 10 µm. **(B, C, D)** Corresponding kymographs with color-coded retrograde (R, orange) and anterograde (A, blue) movements. Triangles highlight a selection of movements in each direction. Scale bars: 5 µm, 10 s. **(E)** Representative maximum intensity projection of a widefield movie of a neuron transfected with SNAP-DIC2C. Dynein was labeled with 100 nM LIVE610-SNAP for 24 h and washed thrice. Red triangles highlight non-specific labeling of mitochondria. White box indicates where the kymograph was generated. The laser intensity of the 640 nm excitation laser was 19 W/cm^2 at an exposure time of 200 ms. Scale bar: 10 µm. **(F)** Corresponding kymograph with color-coded retrograde (R, orange) and anterograde (A, blue) movements. Triangles highlight a selection of movements in each direction. Scale bars: 5 µm, 10 s.

CRISPR/Cas9 Knock-In Specificity Assessment

In order to overcome the aforementioned challenges associated with overexpression, it was investigated whether dynein could be tagged endogenously by specifically and directly editing various dynein genes through the introduction of DNA sequences encoding different protein tags via CRISPR/Cas9-mediated genome editing. To this end, it was first assessed whether the DNA sequences encoding the different protein tags were integrated at the correct location in the genome following electroporation with the respective CRISPR/Cas9 knock-in plasmid. To achieve this, genomic DNA was isolated from electroporated neurons and a PCR was conducted using primers, one of which binds in the respective dynein gene and the other in the respective sequence encoding the protein tag.

Figure 4.2 shows the resulting agarose gels that visualize the length of the PCR products. All of the PCR products exhibited the anticipated length (illustrated by the orange boxes in Fig. 4.2), as determined by the primers' binding to the CRISPR/Cas9-edited genome. The upper bands of the agarose gel were either not sufficiently clean to permit sequence resolution by sequencing or could not be aligned with the genome. It should be noted that the bands with the anticipated length are more prominent than the other bands. Sanger sequencing of the PCR products confirmed the correct integration of all the sequences encoding the protein tags (exemplary demonstrated in Fig. 3.2). This confirmed that the DNA sequence encoding the various protein tags, including EGFP and mEGFP (Cormack et al., 1996; Zacharias et al., 2002), mEOS4b (Paez-Segala et al., 2015), HaloTag7 (Encell et al., 2012; Los et al., 2008), and SNAPf-tag (Keppler et al., 2003; Sun et al., 2011) was integrated correctly at three different sites of the dynein genes.

CRISPR/Cas9-Tagged Dynein Intermediate Chain

Following confirmation of the correct integration of the DNA sequences encoding the protein tags to the dynein genes, the expression and motility of the CRISPR/Cas9-tagged dynein were assessed using the custom-built widefield microscope. Primary hippocampal neurons were first electroporated with the pO-GFP-DIC plasmid using the optimized conditions described above, and CRISPR/Cas9-positive neurons were identified using the eyepieces and the LED lamp. Upon identification of a CRISPR/Cas9-positive neuron (Fig. 4.3A), the axon was identified by its morphology as the longest and smoothest process with a constant diameter (Fig. 4.3B). A series of videos was recorded along the axon, and color-coded kymographs were generated using Fourier filtering (Mangeol et al., 2016; Shih et al., 2013) (Fig. 4.3C).

The kymograph of CRISPR/Cas9-tagged EGFP-DIC displays numerous particles, each discernible by a distinctive line, many of which are also diagonal, indicating a movement in retrograde or anterograde direction (Fig. 4.3C). Similar to the case of the overexpressed EGFP-tagged DIC (Fig. 4.1A), the widefield acquisition in Figure 4.3B also displays background intensity that originates from cellular autofluorescence. Similarly, as with the overexpressed EGFP-tagged dynein, but in contrast to the fluorophore labeling (Fig. 4.1E, F), the

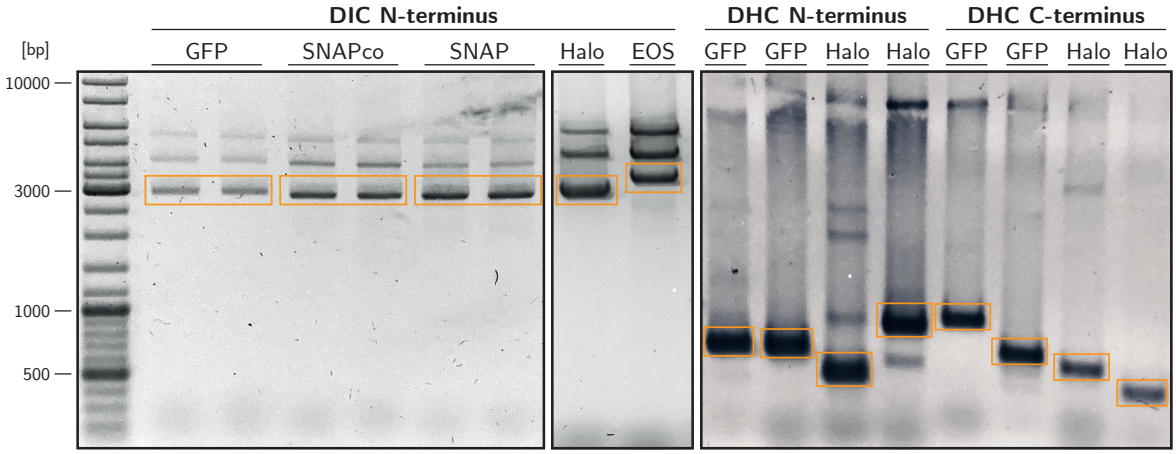

Figure 4.2 | CRISPR/Cas9 knock-in specificity assessment
Agarose gels with PCR products of isolated genomic DNA from neurons electroporated with respective CRISPR/Cas9 knock-in plasmids. Orange boxes indicate the expected PCR product lengths and areas where the bands have been cut out for subsequent DNA purification and sequencing. The expected PCR product lengths for the tagging of the DIC N-terminus were: EGFP (3022 bp), codon-optimized SNAPf-tag (2929 bp), SNAPf-tag (2929 bp), HaloTag7 (2833 bp), mEOS4b (3199 bp), for the DHC N-terminus: mEGFP (640 bp), mEGFP (630 bp), HaloTag (451 bp), HaloTag7 (798 bp), and for the DHC C-terminus: mEGFP (855 bp), mEGFP (610 bp), HaloTag7 (550 bp), HaloTag7 (421 bp).

photostability of EGFP is relatively low, as evidenced by the disappearance of lines at the bottom of the kymograph (end of movie) (Fig. 4.3C). A notable distinction between the overexpression and the tagged dynein approach is the sheer number of dynein motor complexes that are visible in the kymograph. This is due to the fact that the neuron expresses tagged dynein endogenously, as opposed to integrating overexpressed GFP-DIC2C into a select subset of motor complexes. In comparison to overexpression, there are considerably fewer neurons expressing tagged dynein due to the inherent low efficacy of CRISPR/Cas9-mediated knock-in. In any case, the morphology of CRISPR/Cas9-positive neurons appears to be similar to wildtype neurons. This contrasts with the overexpression case, where it remained unclear whether the morphology was altered due to overexpression artifacts (Ratz et al., 2015) or potential effects on the integrity of the entire motor complex and endomembrane localization (King et al., 2003; Vaughan et al., 2001).

Neurons electroporated with the pO-Halo-DIC plasmid were labeled with MaP555-Halo (Wang et al., 2020) and exhibited a similar morphology to those in which an EGFP was knocked-in (Fig. 4.4A, B). However, the background intensity was considerably lower due to the reduced excitation of cellular structures by 532 nm laser light in comparison to 488 nm for EGFP. Another notable distinction between the MaP555-Halo fluorophore and EGFP is its enhanced photostability, as evidenced by the kymograph (Fig. 4.4C, the kymograph was shortened to fit within the page layout). Additionally, the kymograph depicts numerous lines corresponding to individual particles, including anterograde and retrograde movement.

Finally, neurons were electroporated with plasmids pO-SNAP-DIC, pO-SNAPco-DIC,

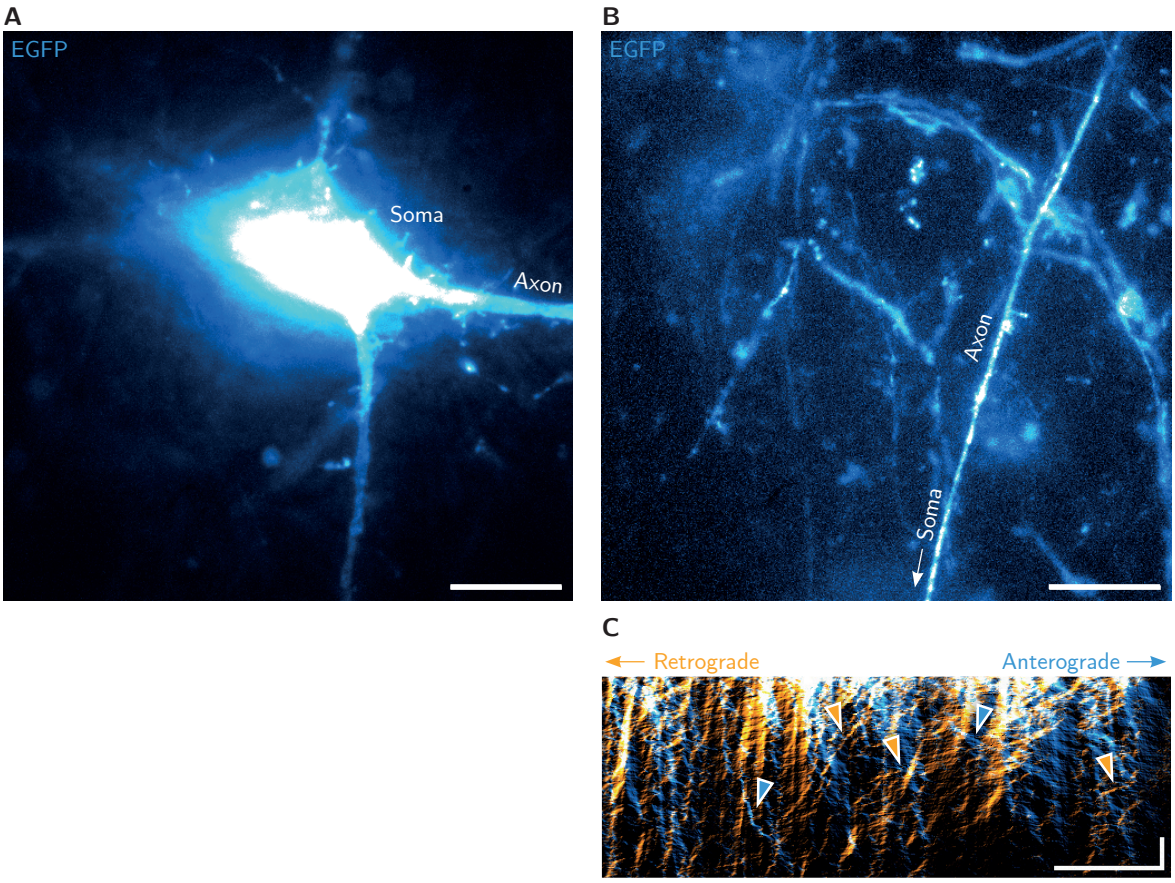

Figure 4.3 | CRISPR/Cas9-mediated knock-in of EGFP to dynein intermediate chain
(A) Representative maximum intensity projection of a widefield movie of the soma of a living primary CRISPR/Cas9-positive neuron electroporated with pO-GFP-DIC. The laser intensity of the 488 nm excitation laser was 49 W/cm^2 at an exposure time of 200 ms. Scale bar: 10 µm. **(B)** Representative maximum intensity projection of a widefield movie of the axon of the same CRISPR/Cas9-positive neuron. The laser intensity of the 488 nm excitation laser was 148 W/cm^2 at an exposure time of 200 ms. Scale bar: 10 µm. **(C)** Corresponding kymograph with color-coded retrograde (orange) and anterograde (blue) movements. Triangles highlight a selection of movements in each direction. Scale bars: 10 µm, 10 s.

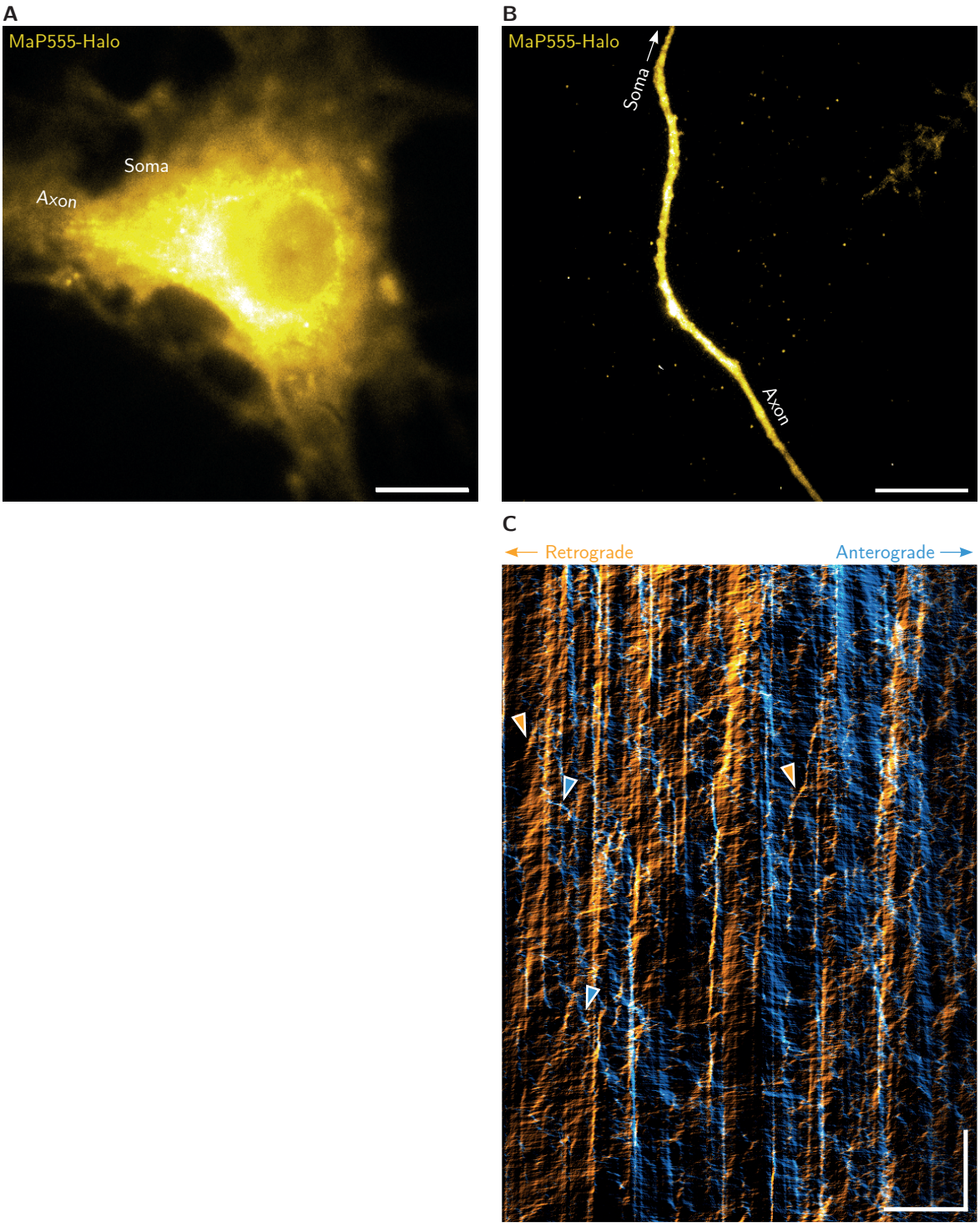

Figure 4.4 | CRISPR/Cas9-mediated knock-in of a HaloTag7 to dynein intermediate chain
(A) Representative frame of a widefield movie of the soma of a living primary CRISPR/Cas9-positive neuron electroporated with pO-Halo-DIC. Dynein was labeled with 10 nM MaP555-Halo for 15 min, washed once, followed by 30 min washout in conditioned medium and finally washed twice. The laser intensity of the 532 nm excitation laser was 92 W/cm^2 at an exposure time of 100 ms. Scale bar: 10 µm. **(B)** Representative maximum intensity projection of a widefield movie of the axon of the same CRISPR/Cas9-positive neuron. The laser intensity of the 532 nm excitation laser was 92 W/cm^2 at an exposure time of 100 ms. Scale bar: 10 µm. **(C)** Corresponding kymograph (displayed shorter due to long movie length) with color-coded retrograde (orange) and anterograde (blue) movements. Triangles highlight a selection of movements in each direction. Scale bars: 10 µm, 10 s.

and pO-EOS-DIC. In the first two cases, neurons were labeled with different SNAP-tag fluorophore ligands. In all cases, no CRISPR/Cas9-positive neurons could be identified using the widefield microscope. By recording several movies of potential CRISPR/Cas9-positive neurons, moving particles could not be observed. Therefore, although the CRISPR/Cas9-mediated integration of the respective DNA sequence encoding the SNAPf- or mEOS4b-tag was successful (Fig. 4.2), the expression of the tagged DIC may have been impeded, the expressed tagged DIC may have been folded incorrectly, or the tag may have impeded the assembly or motility of the whole motor complex.

In summary, CRISPR/Cas9-mediated knock-in of an EGFP and a HaloTag7 to the DIC resulted in the visible bidirectional movement of many particles, without the aforementioned mentioned concerns of overexpression.

CRISPR/Cas9-Tagged Dynein Heavy Chain

In addition to the DIC, the CRISPR/Cas9-mediated tagging of the DHC was investigated by electroporating neurons with the plasmids pO-GFP-DHC and pO-Halo-DHC and subsequent imaging with the custom-built widefield microscope. As the two aforementioned tags were demonstrated to be effective for the tagging of the DIC in living neurons, the generation of CRISPR/Cas9 knock-in plasmids for the tagging of the DHC was not pursued with other tags.

Similar to the CRISPR/Cas9-mediated tagging of the DIC with mEGFP, CRISPR/Cas9-positive neurons and their axon were identified using the eyepieces and LED lamp. The background intensity of the EGFP-tagged DHC (Fig. 4.5A, B) was similar to that of the DIC, and the kymograph showed many particles as indicated by the color-coded lines, including diagonal lines corresponding to retrograde and anterograde movement (Fig. 4.5C). However, the CRISPR/Cas9 knock-in efficacy was higher for the DHC compared to the DIC, as more CRISPR/Cas9-positive neurons were identified per coverslip.

When comparing CRISPR/Cas9-mediated tagging of the DHC with a HaloTag7 (Fig. 4.6A, B) to that of the intermediate chain, there were no notable differences in background intensity or particle movement as shown in the kymograph (Fig. 4.6C). Both retrograde and anterograde movement was observed in the axon of CRISPR/Cas9-positive neurons with considerably higher photostability compared to mEGFP. Note that the kymograph in Figure 4.6C has also been cropped to fit the page layout. The CRISPR/Cas9 knock-in efficacy of HaloTag7 on the DHC was also higher compared to the DIC.

Finally, neurons were also electroporated with the CRISPR/Cas9 knock-in plasmids pO-DHC-GFP and pO-DHC-Halo to tag the C-terminus of the DHC corresponding to the head domain of the dynein motor. In both cases, however, it was not possible to identify CRISPR/Cas9-positive neurons using the custom-built widefield microscope. Although CRISPR/Cas9-mediated integration of the respective DNA sequence encoding the tags was successful (Fig. 4.2), the expression of the tagged C-terminus may have been impeded, the

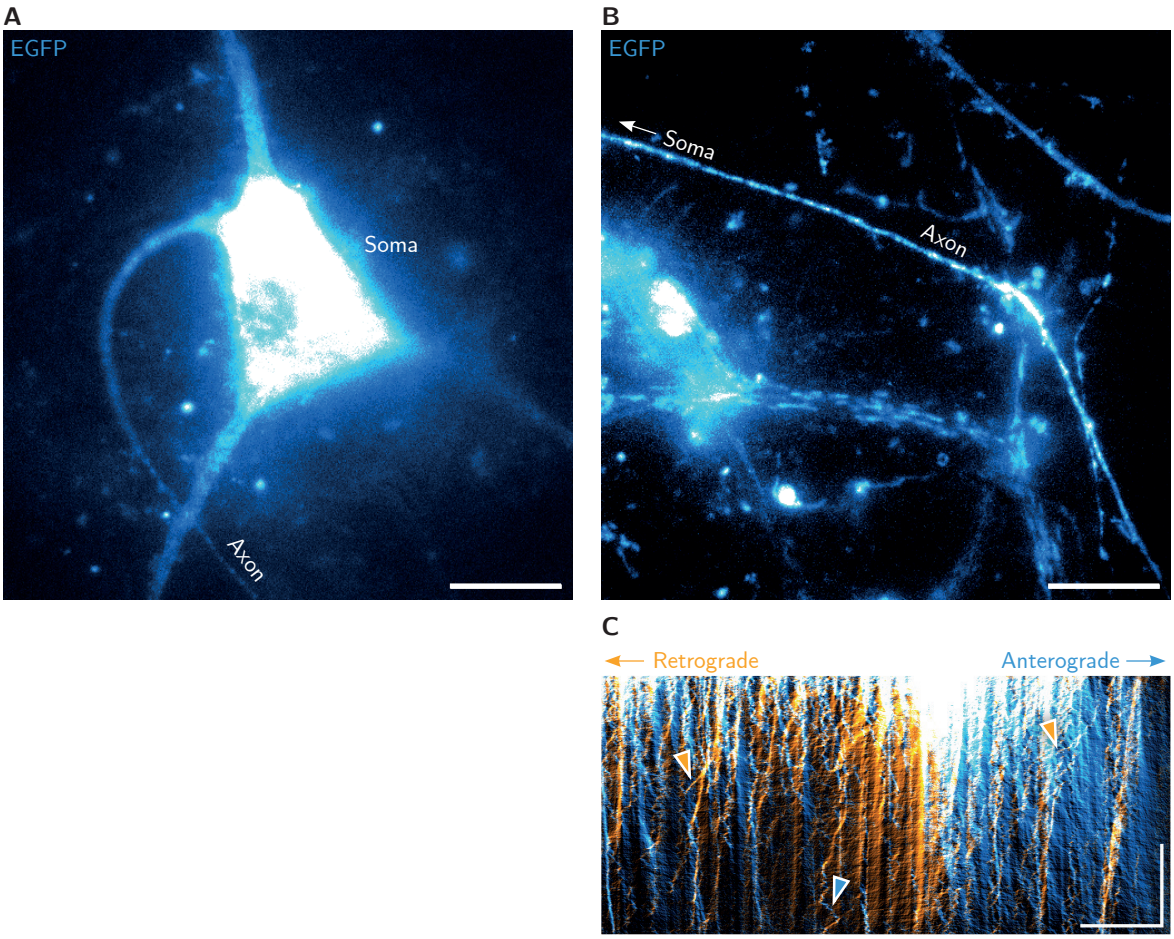

Figure 4.5 | CRISPR/Cas9-mediated knock-in of mEGFP to dynein heavy chain
(A) Representative frame of a widefield movie of the soma of a living primary CRISPR/Cas9-positive neuron electroporated with pO-GFP-DHC. The laser intensity of the 488 nm excitation laser was 31 W/cm^2 at an exposure time of 50 ms. Scale bar: 10 µm. **(B)** Representative maximum intensity projection of a widefield movie of the axon of the same CRISPR/Cas9-positive neuron. The laser intensity of the 488 nm excitation laser was 154 W/cm^2 at an exposure time of 50 ms. Scale bar: 10 µm. **(C)** Corresponding kymograph with color-coded retrograde (orange) and anterograde (blue) movements. Triangles highlight a selection of movements in each direction. Scale bars: 10 µm, 5 s.

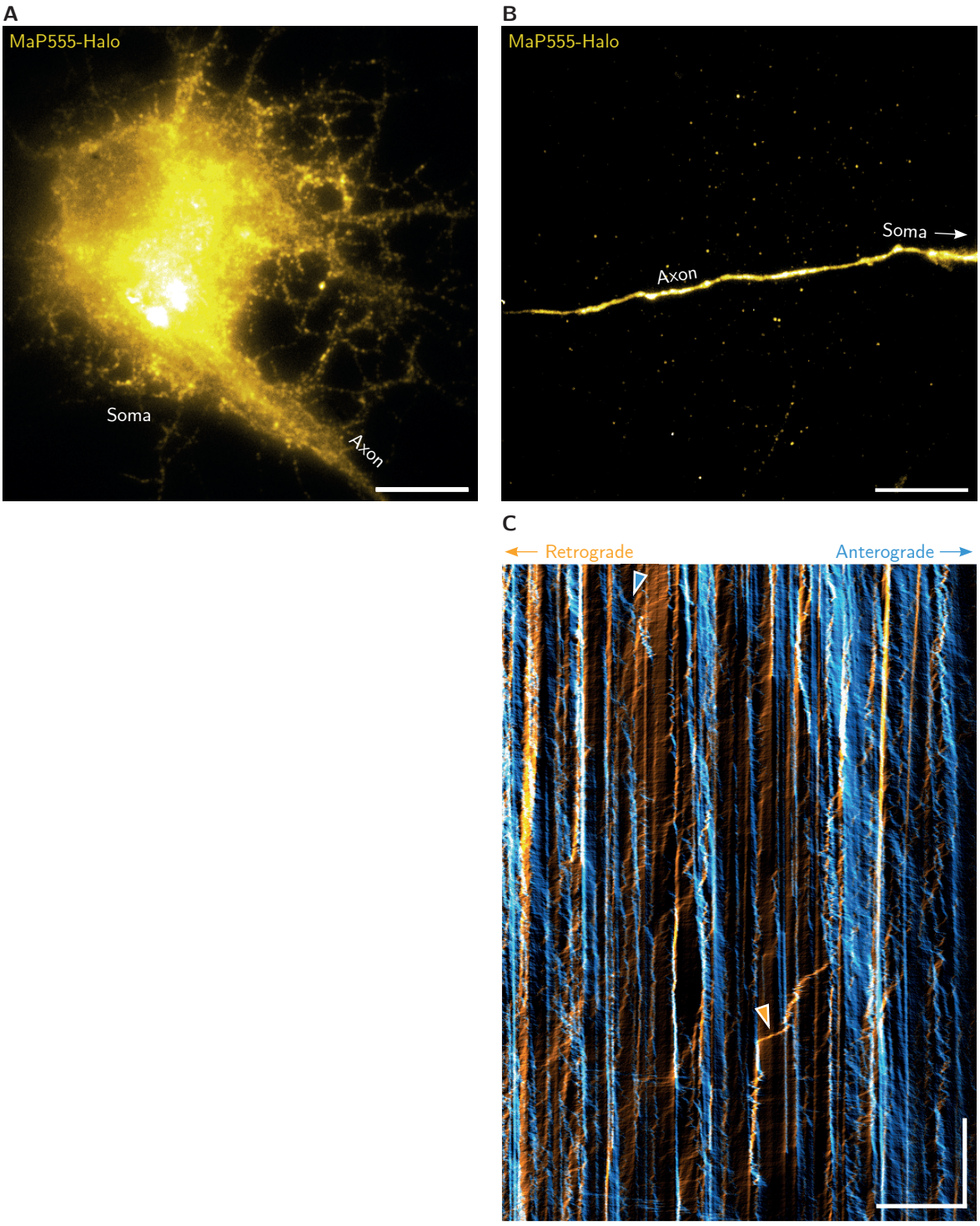

Figure 4.6 | CRISPR/Cas9-mediated knock-in of a HaloTag7 to dynein heavy chain
(A) Representative frame of a widefield movie of the soma of a living primary CRISPR/Cas9-positive neuron electroporated with pO-Halo-DHC. Dynein was labeled with 10 nM MaP555-Halo for 15 min, washed once, followed by 30 min washout in conditioned medium and finally washed twice. The laser intensity of the 532 nm excitation laser was 92 W/cm^2 at an exposure time of 100 ms. Scale bar: 10 µm. **(B)** Representative maximum intensity projection of a widefield movie of the axon of the same CRISPR/Cas9-positive neuron. The laser intensity of the 532 nm excitation laser was 92 W/cm^2 at an exposure time of 100 ms. Scale bar: 10 µm. **(C)** Corresponding kymograph (displayed shorter due to long movie length) with color-coded retrograde (orange) and anterograde (blue) movements. Triangles highlight a selection of movements in each direction. Scale bars: 10 µm, 10 s.

expressed tagged DHC may have been misfolded, or the tag may have impeded assembly or motility of the entire motor complex.

Using CRISPR/Cas9-mediated knock-in in living primary hippocampal neurons, the N-terminus of the DHC was endogenously tagged with mEGFP and HaloTag7 in addition to the DIC. Identification of CRISPR/Cas9-positive neurons containing DHC tagged at the C-terminus may require additional experimental trials.

4.1.3 Optimization of Fluorescent Labeling for MINFLUX Tracking

MINFLUX tracking of dynein in live neurons requires cell-permeable, non-blinking, photostable fluorophores that can be excited with the 561 nm or, even more optimal, the 640 nm excitation laser, as there is considerably reduced autofluorescent cellular background (Lukinavičius et al., 2016). It is also critical that the fluorophores bind specifically to the HaloTag or SNAP-tag, rather than non-specifically to other cellular components. This is necessary to ensure that the observed movement is due to dynein. In addition, non-specifically bound fluorophores generate a strong background intensity that makes MINFLUX tracking difficult or even impossible.

Due to the relatively inefficient nature of CRISPR/Cas9-mediated tagging compared to protein overexpression, only a small proportion of neurons was successfully tagged using CRISPR/Cas9. Consequently, in the case of CRISPR/Cas9-mediated tagging of dynein, two fluorophores that meet the aforementioned requirements are necessary for orthogonal labeling. One fluorophore is required for MINFLUX tracking at a low concentration (excitable by the 561 nm or 640 nm laser) and the other as a counterstain to identify CRISPR/Cas9-positive neurons (excitable by the 488 nm or 561 nm laser). It is important to select a fluorophore for the identification of CRISPR/Cas9-positive neurons with an emission spectrum that is not too red-shifted, as this can make it challenging to identify labeled neurons using the eyepieces.

To identify suitable fluorescent probes, a series of fluorescent HaloTag and SNAP-tag ligands were screened under different labeling conditions, including fluorophore concentration, labeling time, and wash steps. Table 4.1 provides an overview of all tested fluorophores and their performance in terms of specific labeling, low background intensity, photostability, and finally whether moving particles corresponding to dynein were visible using widefield microscopy. The fluorophores that fulfilled these criteria were JF549-Halo and MaP555-Halo, which can be used to identify CRISPR/Cas9-positive neurons, and JF646-Halo and JFX650-Halo, which can be used for MINFLUX tracking. Figures 4.7 and 4.8 illustrates representative widefield recordings of these fluorophores and corresponding kymographs along the axon, where the movement of particles can be observed.

When comparing JF549-Halo and MaP555-Halo in terms of labeling efficacy, a lower fluorophore concentration and shorter labeling time of MaP555-Halo was sufficient to label more particles than in the case of JF549-Halo. This can be seen by comparing the number of lines visible in the kymographs (Fig. 4.7A, D). The high labeling efficacy of MaP555-Halo

Table 4.1 | Fluorophore performance for CRISPR/Cas9-mediated tagging of dynein in living neurons
The fluorophores that permitted the observation of moving particles corresponding to dynein, exhibiting high photostability and low background intensity, are highlighted in bold.

Fluorophore	Ligand	Ex/Em [nm]	Observations
Oregon Green	HaloTag	496/516	Low photostability, non-specific cytosolic background
LIVE 510	SNAP-tag	498/529	Low photostability
R110 Direct	HaloTag	502/527	High background, low photostability
505-Star	SNAP-tag	504/532	Low photostability, non-specific cytosolic background
NL19	HaloTag	514/533	High cytosolic background
JF549	**HaloTag**	**549/571**	**Moving particles, high background**
MaP555	**HaloTag**	**555/580**	**Moving particles, photostable, low background**
580CP	SNAP-tag	582/607	Non-specific cytosolic background
580CP	HaloTag	582/607	Non-specific binding to mitochondria, photostable, low background
610CP	SNAP-tag	609/634	Non-specific cytosolic background
610CP	HaloTag	609/634	Non-specific binding to vesicles, photostable, low background
LIVE 610	SNAP-tag	611/636	Non-specific binding to mitochondria, photostable, low background
SiR	SNAP-tag	641/662	Few neurons visible, blinking in background
JF646	**HaloTag**	**646/664**	**Moving particles, photostable, low background**
JF646	SNAP-tag	646/664	Not possible to find CRISPR/Cas9-positive neurons
JFX650	**HaloTag**	**650/667**	**Moving particles, photostable, low background**

is advantageous to avoid cytotoxicity and, combined with its high photostability and specific labeling, makes it the best choice of all tested fluorophores to identify CRISPR/Cas9-positive neurons.

For MINFLUX tracking, the fluorophores JF646-Halo and JFX560-Halo both showed less background intensity compared to JF549-Halo and MaP555-Halo, probably due to the use of longer wavelength excitation light. No differences in photostability or brightness could be detected between JF646-Halo and JFX560-Halo using the widefield microscope. However, because JFX650-Halo was found to have improved photostability and brightness in live U2OS cells (Grimm et al., 2021), it was used for MINFLUX tracking of dynein in live neurons.

In addition to labeling dynein, microtubules were also stained with different fluorophores as a control to ensure that labeled dynein colocalized with microtubules and to ensure specific labeling. Non-specific labeling, such as binding of the fluorophore to mitochondria, would be seen as colocalized movement in adjacent wild-type neurons. Of the tubulin ligands tested, BioTracker 488 Green Microtubule had the highest photostability and could be used at a low concentration and with a short labeling time (Fig. 4.9A–C).

As described above, SNAP-tagged dynein was observed upon overexpression (Fig. 4.1) but not upon CRISPR/Cas9-mediated knock-in. Among the SNAP-tag ligands, LIVE610-SNAP had the highest photostability, but was found to accumulate non-specifically in mitochondria. However, it is difficult to assess the performance of the SNAP-tag ligands as it was not possible to identify CRISPR/Cas9-positive neurons with CRISPR/Cas9-mediated knock-in of the SNAP-tag to dynein.

For dynein labeling in live neurons, the combination of MaP555-Halo for CRISPR/Cas9-positive neuron identification, JFX650-Halo for MINFLUX tracking, and BioTracker 488 Green Microtubule for microtubule staining was the best combination of fluorophores tested.

4.1.4 Evaluating PC12 Cells as a Study System for Dynein Tracking

Given that dynein is the essential molecular motor for retrograde transport of cellular cargo not only in the axons of neurons but in all eukaryotes (Reck-Peterson et al., 2018), live-cell tracking of dynein using MINFLUX may be possible in other cells beyond neurons. PC12 cells, derived from transplantable rat pheochromocytoma, represent a suitable option due to their rat genome, which enables the use of the same CRISPR/Cas9-mediated tagging plasmids used for rat hippocampal neurons.

To evaluate whether PC12 cells are a suitable study system for live-cell tracking of dynein, PC12 cells were transfected with the pO-Halo-DIC plasmid and imaged using the custom-built widefield microscope. Figure 4.10A shows a CRISPR/Cas9-positive PC12 cell with MaP555-Halo labeled dynein, which demonstrates that the entire cytosol is labeled. This appears to be similar to the soma of neurons, where the entire soma is also labeled (Fig. 4.9A), and to what has been previously observed in PC12 cells with overexpressed DIC fused to GFP (Myers et al., 2007). To track individual particles, the cell was illuminated with high laser intensity

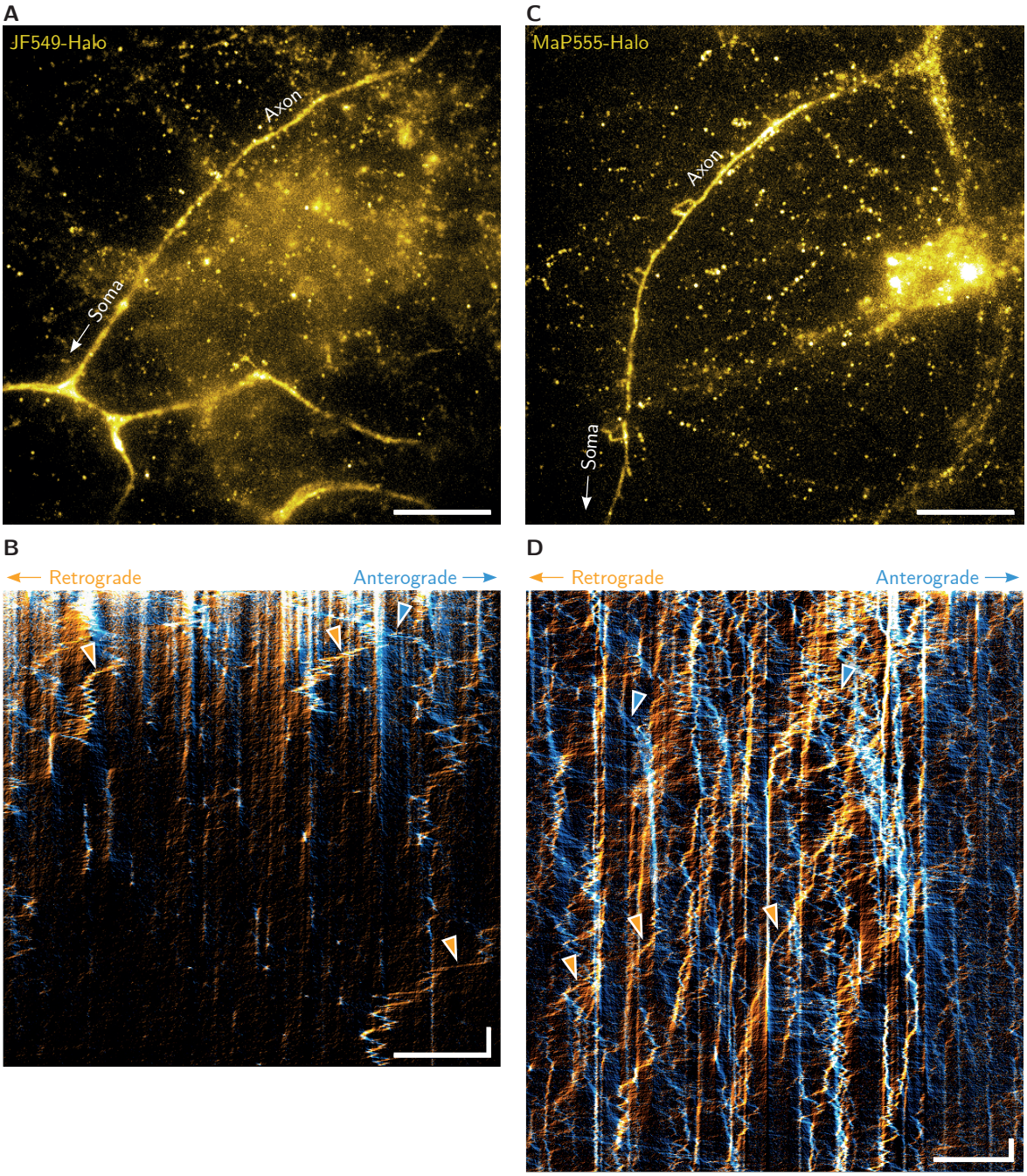

Figure 4.7 | Labeling of dynein with JF549-Halo and MaP555-Halo
(A) Representative maximum intensity projection of a widefield movie of the axon of a living primary CRISPR/Cas9-positive neuron electroporated with pO-Halo-DIC. Dynein was labeled with 100 nM JF549-Halo for 60 min, washed twice, followed by 50 min washout in conditioned medium and finally washed twice. The laser intensity of the 532 nm excitation laser was 975 W/cm^2 at an exposure time of 30 ms. Scale bar: 10 µm. **(B)** Corresponding kymograph with color-coded retrograde (orange) and anterograde (blue) movements. Triangles highlight a selection of movements in each direction. Scale bars: 10 µm, 1 s. **(C)** Representative maximum intensity projection of a widefield movie of the axon of a CRISPR/Cas9-positive neuron electroporated with pO-Halo-DIC. Dynein was labeled with 10 nM MaP555-Halo for 15 min, washed once, followed by 30 min washout in conditioned medium and finally washed twice. The laser intensity of the 532 nm excitation laser was 92 W/cm^2 at an exposure time of 100 ms. Scale bar: 10 µm. **(D)** Corresponding kymograph with color-coded retrograde (orange) and anterograde (blue) movements. Triangles highlight a selection of movements in each direction. Scale bars: 10 µm, 3 s.

for several seconds to photobleach the majority of the labeled dynein. Figure 4.10B shows a time-lapse color-coded image of the left part of the same cell after photobleaching, wherein movement is indicated by the rainbow-colored trajectory marked by the white triangle. The inset (Fig. 4.10C) shows the corresponding kymograph.

In general, it is possible to track endogenous dynein in live PC12 cells. However, because virtually all dynein motor complexes in the cytosol are labeled, tracking individual particles would be very challenging and only possible after photobeaching or reduction of the fluorophore concentration. Moreover, it is difficult to discern between anterograde and retrograde movement, as the microtubules may not be oriented in the same direction. Additional microtubule orientation markers, such as CLIP-170 or EB1 (Howard and Hyman, 2003; Perez et al., 1999), may be necessary to determine microtubule orientation. Conversely, neurons form elongated and thin axons that contain unidirectionally oriented microtubules. As a result, axons facilitate both the identification of the transport direction and the tracking of individual particles due to their much greater dispersion along the axon length over several hundred microns.

Figure 4.8 ***(facing page)*** **| Labeling of dynein with JF646-Halo and JFX650-Halo**
(A) Representative maximum intensity projection of a widefield movie of the axon of a living primary CRISPR/Cas9-positive neuron electroporated with pO-Halo-DIC. Dynein was labeled with 1 nM JF646-Halo for 15 min, washed twice, followed by 30 min washout in conditioned medium and finally washed thrice. The laser intensity of the 640 nm excitation laser was 370 W/cm^2 at an exposure time of 100 ms. Scale bar: 10 µm. **(B)** Corresponding kymograph with color-coded retrograde (orange) and anterograde (blue) movements. Triangles highlight a selection of movements in each direction. Scale bars: 10 µm, 3 s. **(C)** Representative maximum intensity projection of a widefield movie of the axon of a CRISPR/Cas9-positive neuron electroporated with pO-Halo-DIC. Dynein was labeled with 0.5 nM JFX650-Halo for 15 min, washed once, followed by 30 min washout in conditioned medium and finally washed thrice. The laser intensity of the 640 nm excitation laser was 352 W/cm^2 at an exposure time of 100 ms. Scale bar: 10 µm. **(D)** Corresponding kymograph with color-coded retrograde (orange) and anterograde (blue) movements. Triangles highlight a selection of movements in each direction. Scale bars: 10 µm, 3 s.

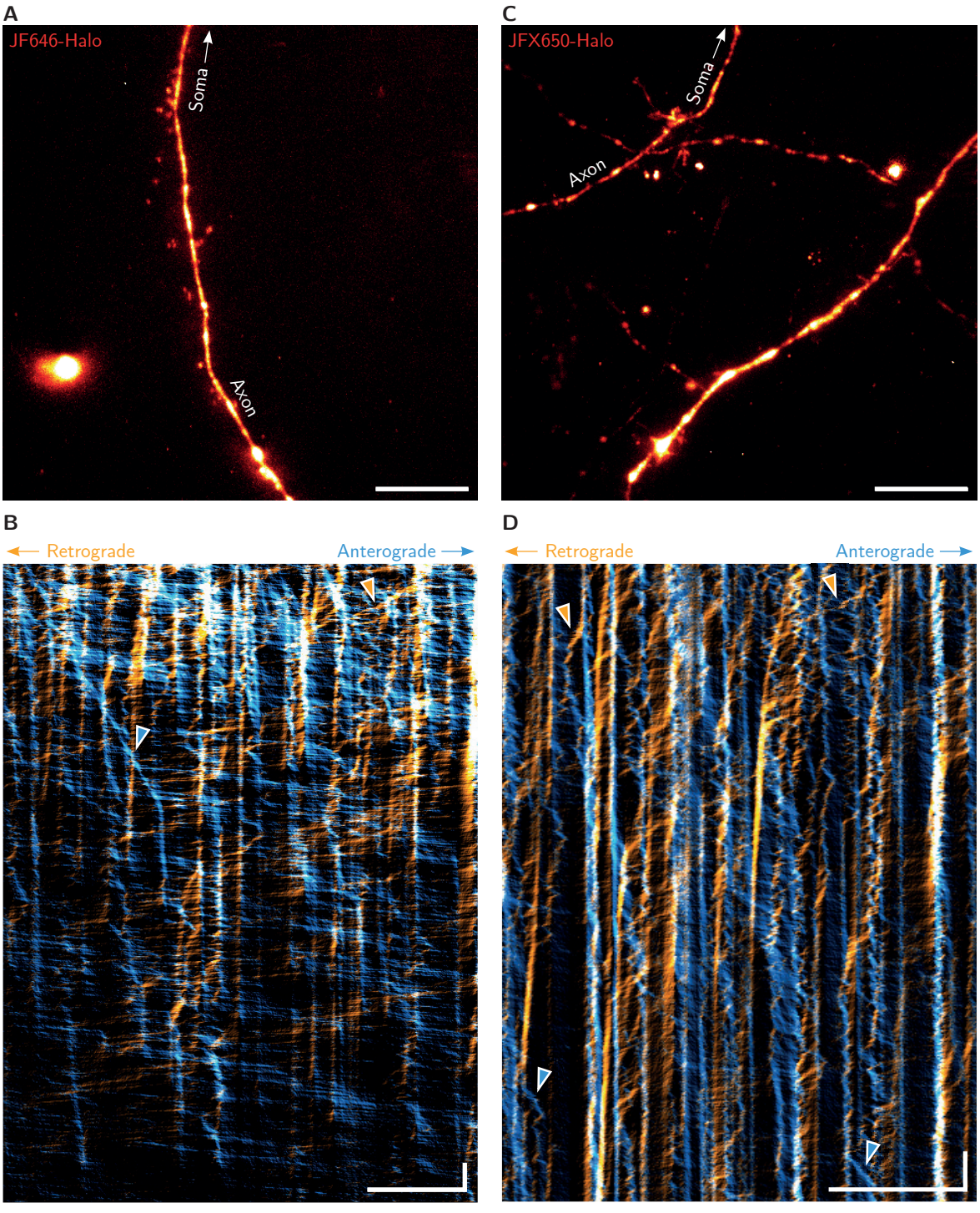
A
JF646-Halo
Soma
Axon
C
JFX650-Halo
Soma
Axon
B
Retrograde
Anterograde
D
Retrograde
Anterograde

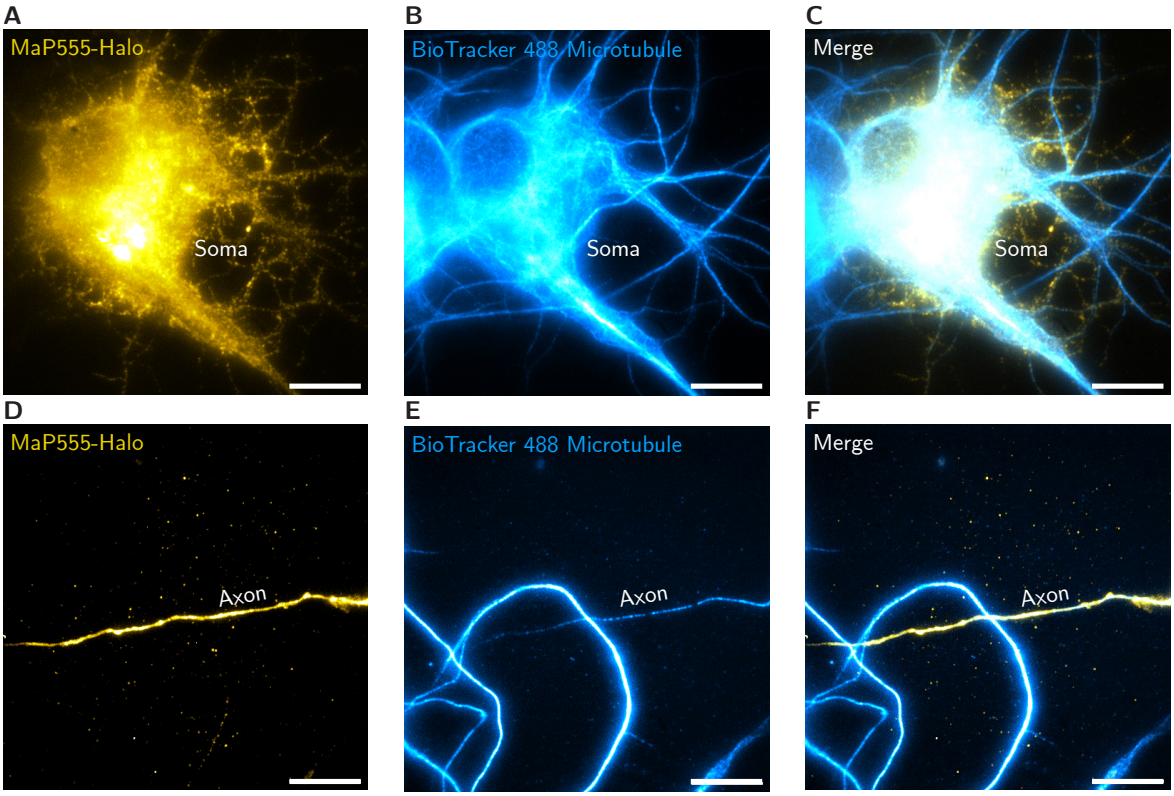

Figure 4.9 | Colocalization of dynein and microtubules
(A) Widefield movie frame of a living primary CRISPR/Cas9-positive neuron, electroporated with pO-Halo-DHC, labeled with MaP555-Halo and excited with the 532 nm laser (same ROI as in Fig. 4.6A). **(B)** Maximum intensity projection of the same ROI where microtubules were stained with BioTracker 488 Green Microtubule (1:40,000) for 15 min and excited with the 488 nm laser at an intensity of 92 W/cm^2. **(C)** Overlay of dynein labeling (A) and microtubule staining (B). **(D)** Maximum intensity projection of a widefield movie of the axon, labeled with MaP555-Halo and excited with the 532 nm laser (same ROI as in Fig. 4.6B). **(E)** Maximum intensity projection of the same ROI (as shown in (D)), excited with the 488 nm laser at an intensity of 92 W/cm^2. **(F)** Overlay of dynein labeling (D) and microtubule staining (E). Scale bars: 10 µm.

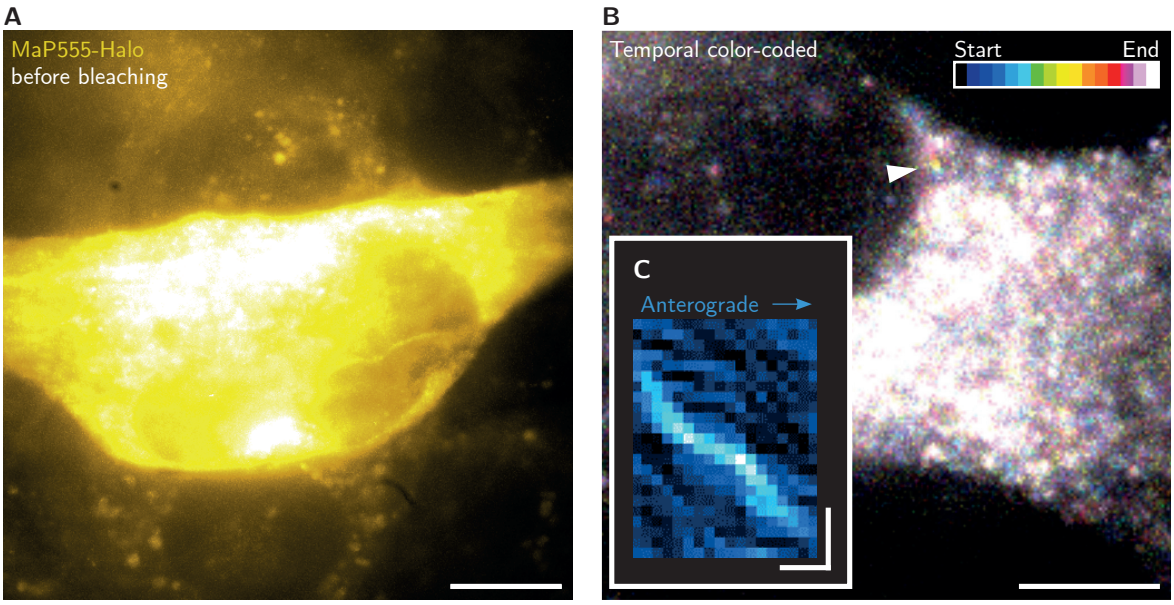

Figure 4.10 | PC12 cells as study system for dynein tracking
(A) Representative maximum intensity projection of a widefield movie of a living PC12 cell transfected with pO-Halo-DIC. Dynein was labeled with 500 nM MaP555-Halo for 15 min, washed twice, followed by 45 min washout in conditioned medium and finally washed twice. The laser intensity of the 532 nm excitation laser was 260 W/cm^2 at an exposure time of 30 ms. Scale bar: 10 µm. **(B)** Temporal color-coded maximum intensity projection of a zoom-in of the same PC12 cell. The white triangle highlights a trajectory of an outward-moving (anterograde) particle as seen by the rainbow-like color. Scale bar: 5 µm. **(C)** Enlarged kymograph of the anterograde moving particle in (B). Scale bars: 500 nm, 200 ms.

4.2 Single-Molecule Tracking of Endogenous Dynein in Living Neurons

The dynein motor complex has been previously studied in neurons by labeling the transported cargo (Deinhardt et al., 2006; Maday et al., 2014), performing overexpression of tagged dynein subunits (Guo et al., 2016; King et al., 2003), or by CRISPR/Cas9-mediated tagging in induced neurons (Fellows et al., 2024). Here, the CRISPR/Cas9-mediated tagging of two dynein subunits in primary neurons was established, which can now be utilized to examine and contrast the motility of these dynein subunits with the custom-built widefield microscope.

To perform single-molecule tracking of endogenous DIC and DHC, primary hippocampal neurons were electroporated with the pO-Halo-DIC and pO-Halo-DHC plasmids using the optimized conditions (Section 4.1.1). After six to nine days in culture, dynein was labeled with 10 nM MaP555-Halo and 1:40,000 BioTracker 488 Green Microtubule for 15 min (Fig. 4.11A). Labeling with MaP555-Halo facilitates both the single-molecule tracking of dynein and the identification of CRISPR/Cas9-positive neurons. The concentration of the fluorophore MaP555-Halo was determined to be optimal for labeling a sufficient number of dynein molecules for sufficient motile events, while avoiding the hindrance of single-molecule tracking by an excess of labeled non-processive motors along the microtubule tracks. To confirm specific labeling of dynein, the low microtubule staining concentration and time were employed to image the microtubules at a brightness level that avoided cytotoxicity and channel bleed-through while still allowing for sufficient visualization of microtubules. After labeling, the neurons were washed once, followed by a 30-minute washout in conditioned medium, and finally imaged in ACSF.

The custom-built widefield microscope was employed to identify CRISPR/Cas9-positive neurons, utilizing the LED lamp and eyepieces. To identify the axon, each neurite was traced from the soma to its terminal point to assess its potential as the axon. The longest and smoothest process was determined to be the axon (Cason et al., 2023). If the identification process was inconclusive, a new CRISPR/Cas9-positive neuron was sought until it was confirmed that the axon was identified. This is important because only in the axon is the microtubule orientation unidirectional (Baas et al., 1988), allowing for the study of active dynein-mediated transport as the movement from the axon tip backward to the soma, which is referred to as retrograde transport (Guedes-Dias and Holzbaur, 2019).

The exposure time of the EMCCD camera was set to 100 ms in fast acquisition mode, and the laser intensity to 92 W/cm^2, which was the optimal trade-off between high signal-to-noise ratio of the tracked dynein particles and long trajectories before photobleaching. In all widefield ROIs, microtubules were first imaged and bleached to avoid channel bleed-through and thus unnecessary background intensity along the microtubules.

4.2.1 Dynein Intermediate Chain Motility in Primary Neurons

To examine the motility of the DIC in primary neurons, 22 movies were recorded in four biological replicates using a custom-built widefield microscope. The procedure was as previously described. Figure 4.11B–D depicts the soma of a representative maximum intensity image from a movie of a CRISPR/Cas9-positive neuron. A comparison of the Halo-DIC image (Fig. 4.11B) with the microtubule staining (Fig. 4.11C) reveals an apparent overlay of both images, while at the bottom left, a wildtype neuron is visible in the microtubule staining (Fig. 4.11C–D). This demonstrates that CRISPR/Cas9-positive neurons can be clearly distinguished from wildtype neurons. The axon was identified as described above and several movies along the axon were recorded. A representative maximum intensity image of one movie is shown in Figure 4.11E–G. The microtubule staining in comparison to the Halo-DIC image reveals neurites from wildtype neurons, thereby demonstrating the specificity of the labeling.

After the experimental acquisition, the movies were analyzed and the axons within the recorded movies were carefully traced in Fiji ImageJ (Schindelin et al., 2012). Kymographs were created, in which the recorded intensity along the traced axon of each movie frame is projected as a horizontal line with the time axis in vertical direction. This allows the identification of particles that move along the axon as diagonal lines, whereas particles that are stationary will appear as vertical lines. Fourier filtering was applied to the kymographs in order to distinguish between retrograde and anterograde movement (Mangeol et al., 2016; Shih et al., 2013).

Figure 4.12 shows a representative kymograph corresponding to the axon in Figure 4.11E, where retrograde movement is colored in orange and anterograde movement in cyan. In the kymograph, numerous particles are visible, whereas the majority appears to be stationary, indicated by the vertical lines. In the upper right-hand corner, a long retrograde movement is visible, representing dynein-driven movement back to the soma. This movement is redrawn on the right for clarity. It is interrupted by two pauses, as indicated by the short vertical sections, and ends with another pausing or stationary state. On the other side, four sections of bidirectional movement are redrawn, including a direction reversal from either anterograde to retrograde or retrograde to anterograde movement.

The observation that the majority of dynein motors appear stationary has also been made in induced neurons, suggesting that only a small portion of dynein motors are actively involved in retrograde transport (Fellows et al., 2024). Furthermore, the bidirectional nature of dynein movement, including direction reversals and pauses, has also been observed previously for different transported cargoes (Encalada et al., 2011; Kobayashi and Murayama, 2009; Kural et al., 2005; Morris and Hollenbeck, 1993; Soppina et al., 2009). It seems plausible to suggest that anterograde movement involves the active motion of the opposing kinesin motor family, which is known to transport cargo, where dynein binds (Hancock, 2014; Maday et al., 2014; Welte, 2004). Therefore, it seems reasonable to conclude that labeled dynein molecules travel anterogradely as a passenger of kinesin-driven movement.

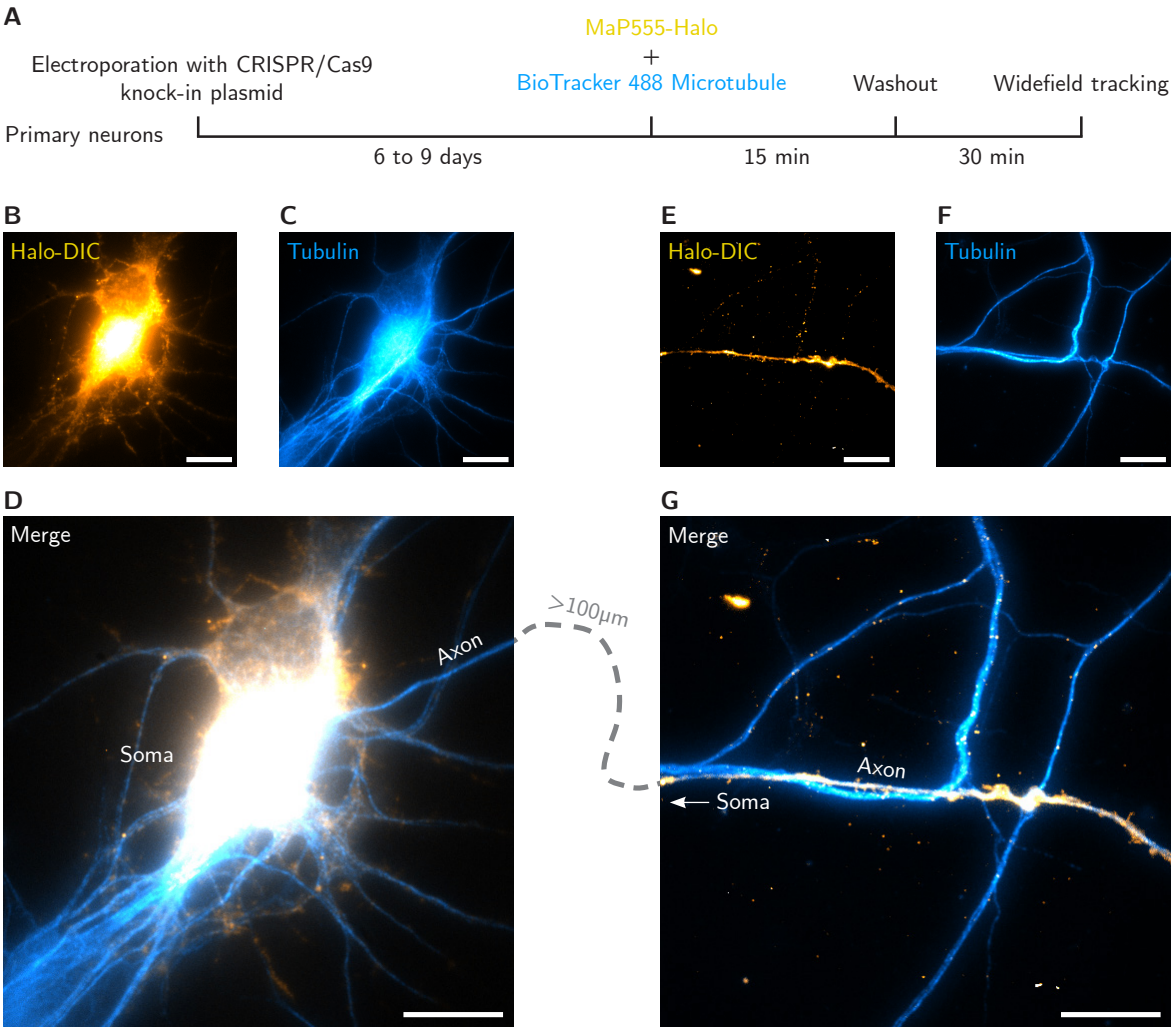

Figure 4.11 | Colocalization of CRISPR/Cas9-tagged dynein intermediate chain and microtubules in a living primary neuron

(A) Primary neurons were electroporated with pO-Halo-DIC after six to nine days in culture. Dynein was labeled simultaneously with 10 nM MaP555-Halo and 1:40,000 BioTracker 488 Green Microtubule for 15 min, washed once, followed by 30 min washout in conditioned medium, washed twice, and imaged in ACSF. **(B)** Representative maximum intensity image of a widefield movie of the soma of a living primary CRISPR/Cas9-positive neuron. The laser intensity of the 532 nm excitation laser was 92 W/cm^2 at an exposure time of 100 ms. **(C)** Maximum intensity image of the same ROI where the tubulin staining was excited by the 488 nm laser at 92 W/cm^2. **(D)** Overlay of dynein and microtubules showing the soma and axon of the living primary neuron. **(E)** Representative maximum intensity image of a widefield movie of the axon of the same neuron in which the labeled DIC was excited. **(F)** Maximum intensity image of the same ROI where the tubulin staining was excited. **(G)** Overlay of dynein and microtubules showing the axon of the living primary neuron. The ROI shown is more than 100 µm from the soma. Scale bars: 10 µm.

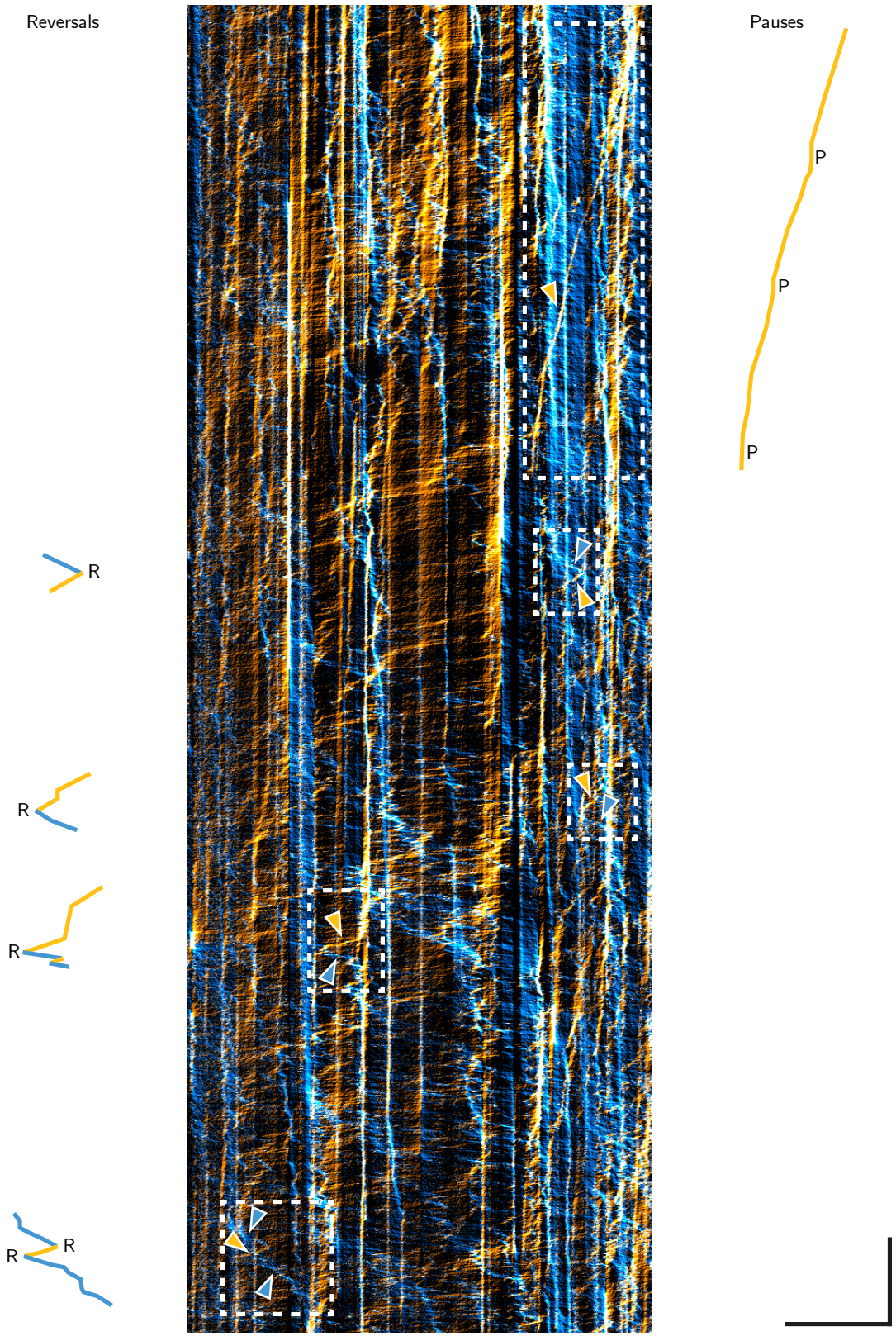

Figure 4.12 | Pauses and direction reversals within endogenous dynein intermediate chain movement
Kymograph along the axon as shown in Figure 4.11E, revealing pauses (P) and direction reversals (R) within the endogenous dynein movement. Trajectories were traced within the white dotted boxes in the kymograph. Anterograde (cyan) and retrograde (orange) movements are indicated by colored triangles. Scale bars: 10 µm, 10 s

To investigate the speed of the CRISPR/Cas9-tagged dynein motors, segments of processive movement, that is, uninterrupted movement, were collected using the kymographs generated along the axons. 343 segments with a run length longer than 1 µm were considered in the analysis. The segment speed is shown in Figure 4.13 as a histogram, with anterograde speed represented in cyan and retrograde speed in orange. It should be noted that the direction of speed was defined as positive in the retrograde direction, which corresponds to dynein-driven motion. The distributions in both directions appear to be very similar, with speeds up to 4.5 µm s^{-1} and a median speed of approximately 1.5 µm s^{-1} in each direction. This is comparable to what was observed previously in induced neurons (Fellows et al., 2024), amyloid precursor protein (Fu and Holzbaur, 2013), or prion protein vesicles (Encalada et al., 2011).

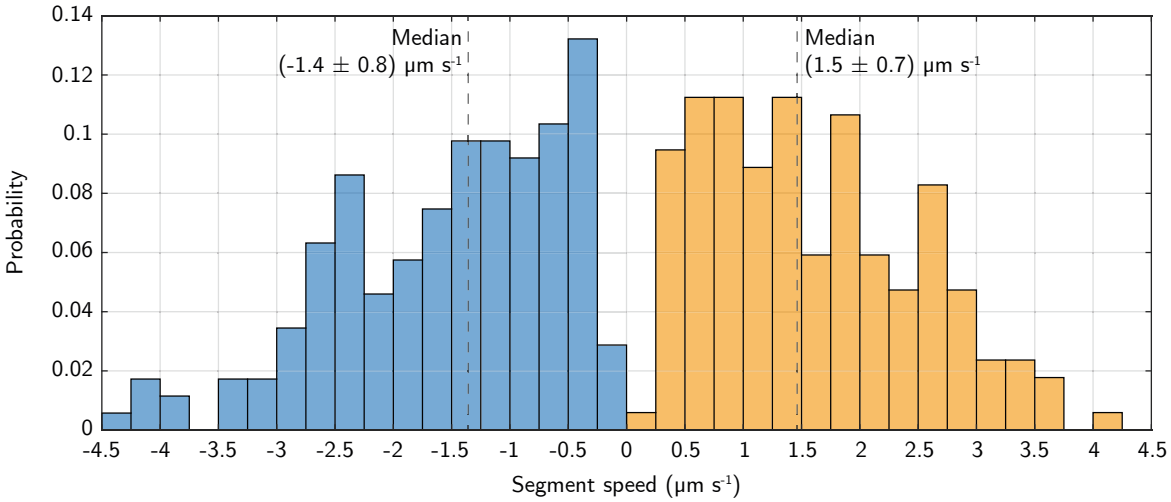

Figure 4.13 | Segment speed of endogenous dynein intermediate chain
Histogram showing the speed of the CRISPR/Cas9-tagged DIC in anterograde (cyan, n = 174) and retrograde (orange, n = 169) segments. Medians are indicated by the dotted line (with median absolute deviation as uncertainty). Only segments with run lengths longer than 1 µm were considered.

4.2.2 Dynein Heavy Chain Motility in Primary Neurons

The motility of the DHC in living primary neurons was investigated using the same aforementioned sample preparation procedure, but this time with the pO-Halo-DHC plasmid. CRISPR/Cas9-positive neurons and their axons were identified according to the same procedure. A total of 25 movies were recorded in six biological replicates. Figure 4.14A–C shows a soma of a CRISPR/Cas9-positive neuron. By comparing the Halo-DHC image with microtubule staining, a wildtype neuron at the bottom can be seen, demonstrating the distinction between CRISPR/Cas9-positive and wildtype neurons. The specificity of the labeling can also be appreciated in the overlay of the associated axon (Fig. 4.14D—F). The Halo-DHC-positive neurons exhibited similar characteristics to those of Halo-DIC-positive neurons. However, the

efficacy of CRISPR/Cas9-mediated knock-in was higher for Halo-DHC, as more positive neurons per coverslip could be identified.

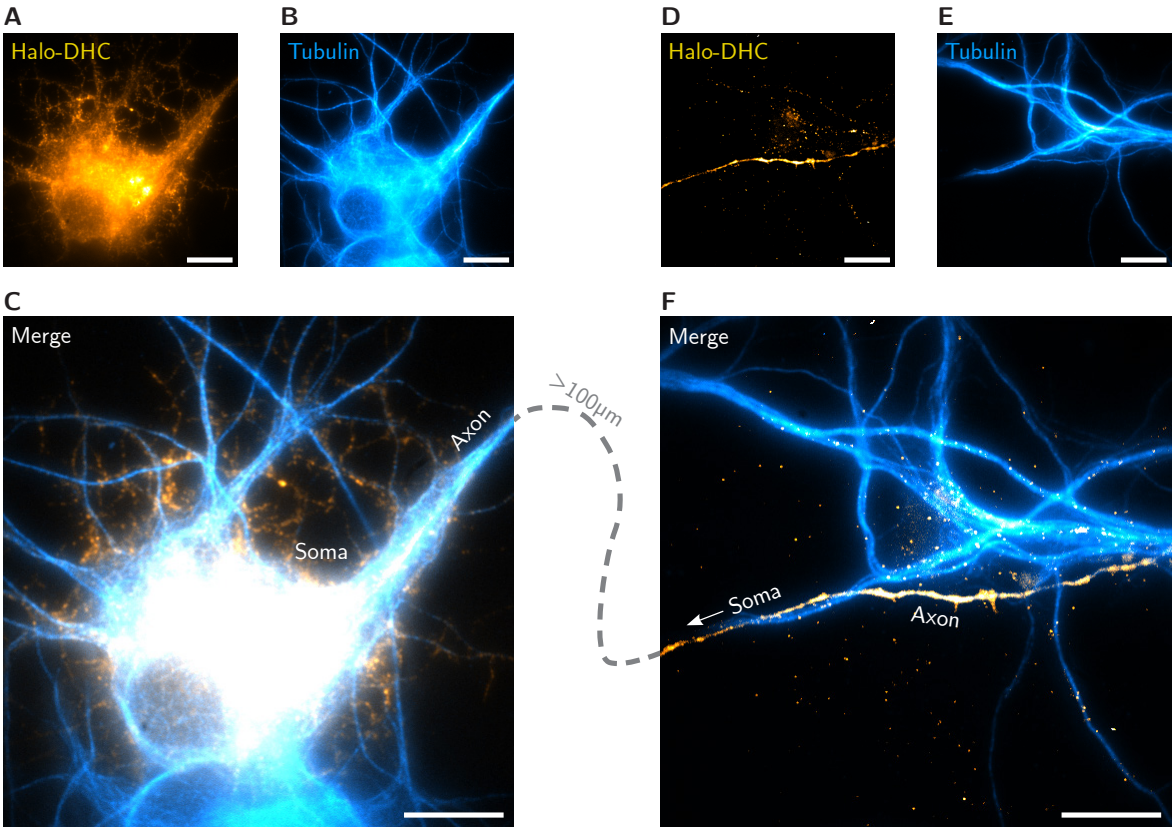

Figure 4.14 | Colocalization of CRISPR/Cas9-tagged dynein heavy chain and microtubules in a living primary neuron
(A) Representative maximum intensity image of a widefield movie of the soma of a living primary CRISPR/Cas9-positive neuron electroporated with pO-Halo-DHC after seven days in culture. Dynein was labeled simultaneously with 10 nM MaP555-Halo and 1:40,000 BioTracker 488 Green Microtubule for 15 min, washed once, followed by 30 min washout in conditioned medium, washed twice, and imaged in ACSF. The laser intensity of the 532 nm excitation laser was 92 W/cm^2 at an exposure time of 100 ms. **(B)** Maximum intensity image of the same ROI where the tubulin staining was excited by the 488 nm laser at 92 W/cm^2. **(C)** Overlay of dynein and microtubules showing the soma and axon of the living primary neuron. **(D)** Representative maximum intensity image of a widefield movie of the axon of the same neuron in which the labeled DIC was excited. **(E)** Maximum intensity image of the same ROI where the tubulin staining was excited. **(F)** Overlay of dynein and microtubules showing the axon of the living primary neuron. The ROI shown is more than 100 µm from the soma. Scale bars: 10 µm.

The kymograph in Figure 4.15 illustrates the movement of the endogenous DHC, corresponding to the representative recording of the axon in Figure 4.14D. As with the DIC, most particles remained stationary, as seen by the vertical lines. Some particles exhibited bidirectional movement, including direction reversals, as well as pauses or transitions into a long-lasting pause or stationary state.

Once more, a segmentation of processive retrograde and anterograde movements was carried out. A total of 329 segments were recognized with run lengths exceeding 1 µm. The

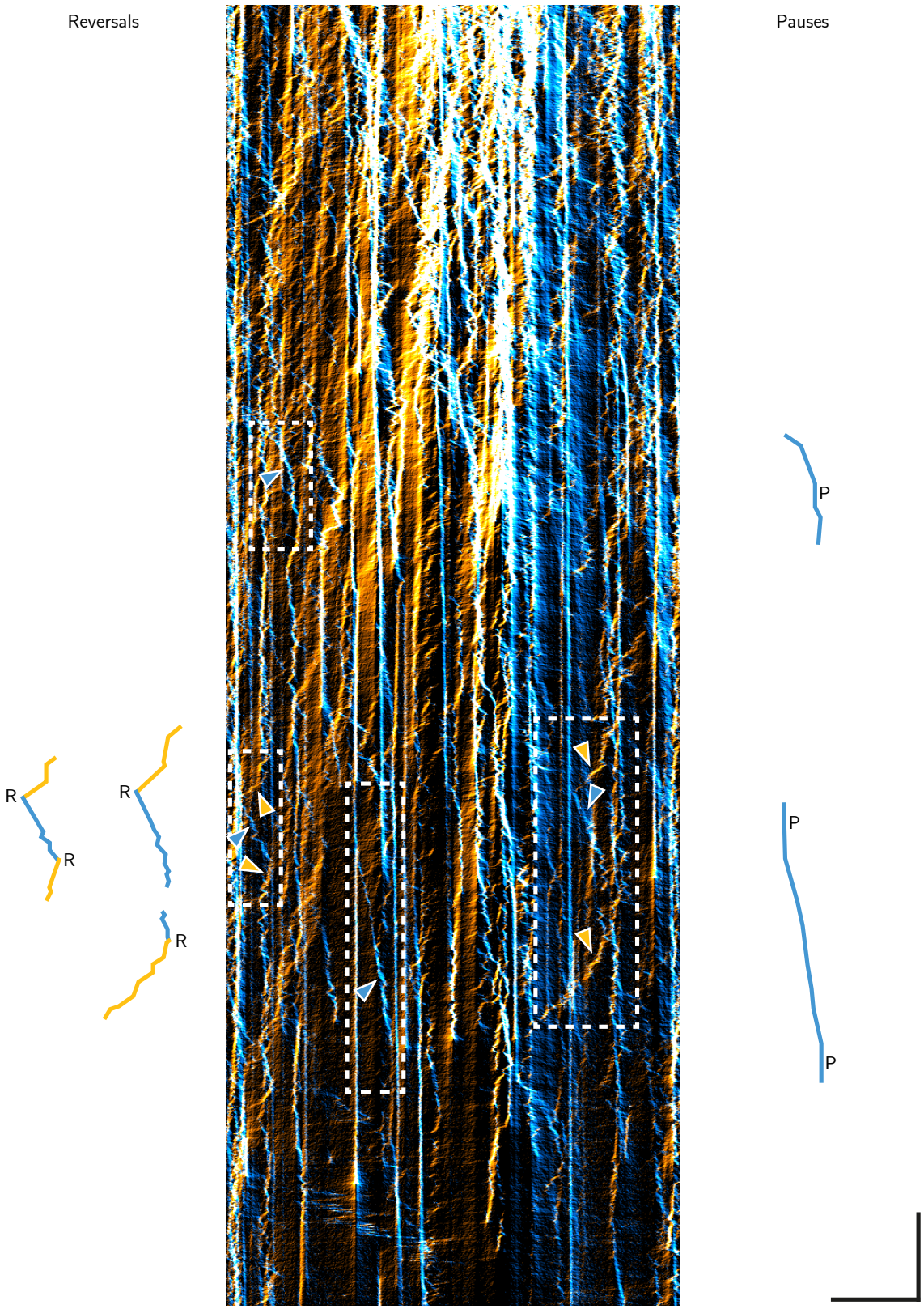

Figure 4.15 | Pauses and direction reversals within endogenous dynein heavy chain movement
Kymograph along the axon as shown in Figure 4.14D–F, revealing pauses (P) and direction reversals (R) within the endogenous dynein movement. Trajectories were traced within the white dotted boxes in the kymograph. Anterograde (cyan) and retrograde (orange) movements are indicated by colored triangles. Scale bars: 10 µm, 10 s

corresponding segment speed is displayed in the histogram depicted in Figure 4.16. The median speed, approximately $1\,\mu m\,s^{-1}$, was comparable in both directions, although slightly slower than what was observed for the DIC. Nevertheless, this speed is still comparable to that observed in the aforementioned literature. The DHC experiments were conducted earlier, with a culture period of six to seven days, than those of the DIC, which were performed after eight and nine days in culture. This may influence the motility of dynein in living neurons as they mature. The region of the axon where the movies were recorded may also influence the processivity and speed of dynein, as has been partially observed in dorsal root ganglion neurons (Peng et al., 2024). The experiments conducted here did not differentiate which region of the axon the movies were recorded in, which could result in slightly different speeds.

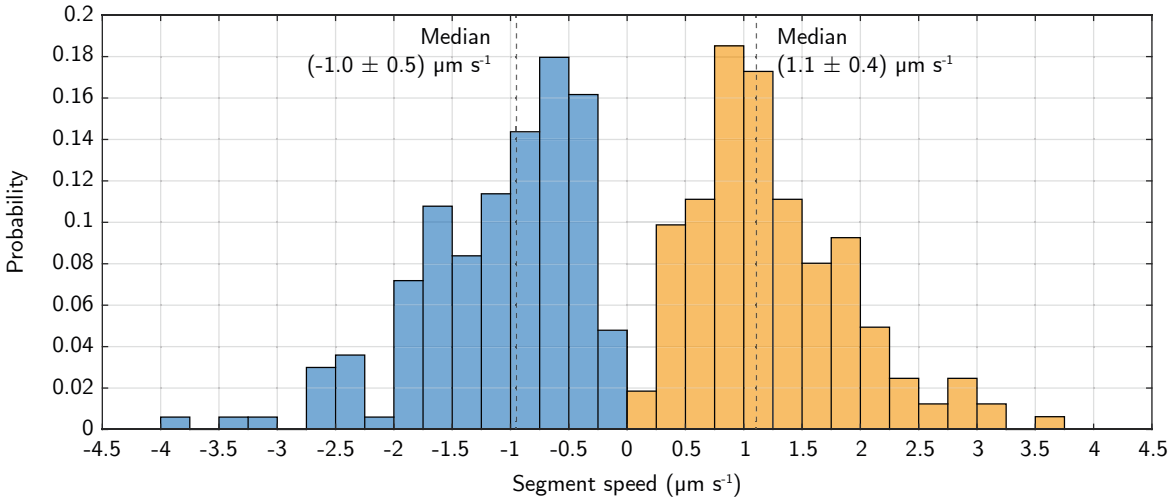

Figure 4.16 | Segment speed of endogenous dynein heavy chain
Histogram showing the speed of the CRISPR/Cas9-tagged DHC in anterograde (cyan, n = 167) and retrograde (orange, n = 162) segments. Medians are indicated by the dotted line (with median absolute deviation as uncertainty). Only segments with run lengths longer than 1 µm were considered.

4.3 Stepping Behavior of Endogenous Dynein Scrutinized by MINFLUX

The molecular motor dynein has been observed to perform discrete, nanometer-sized steps within milliseconds on the microtubule lattice in a direction towards the minus end (Mallik et al., 2004; Reck-Peterson et al., 2006). To date, the stepping behavior of dynein has been predominantly investigated *in vitro* at a reduced ATP concentration, which has been decreased by multiple orders of magnitude to markedly slow its movement (DeWitt et al., 2012; Elshenawy et al., 2019; Niekamp et al., 2021; Qiu et al., 2012). Consequently, the dwell times between successive steps were extended to enable the resolution of individual steps through the use of established single-molecule tracking techniques. MINFLUX, conversely, enables the discernment of molecular movement within the single-digit nanometer/millisecond domain (Deguchi et al., 2023; Wirth et al., 2023). Therefore, to identify the actual rapid, discrete steps of the dynein motor and thereby investigate its unimpeded stepping behavior in living cells, a MINFLUX microscope with a donut-shaped excitation beam was utilized (Schmidt et al., 2021).

To enable the tracking of individual dynein motors in living cells using the MINFLUX microscope, primary hippocampal neurons were electroporated with CRISPR/Cas9 HaloTag-dynein knock-in plasmids in accordance with the aforementioned optimal conditions (Section 4.1.1). After six to nine days in culture, Halo-DHC or Halo-DIC were labeled with a low concentration (100 pM) of JFX650-Halo for 15 min followed by a second 15-minute labeling step with both 100 nM MaP555-Halo and 1:20,000 BioTracker 488 Green Microtubule (Fig. 4.17A), as these were identified as the optimal labeling conditions (Section 4.1.3). Following a 30-minute washout in conditioned medium, Halo-DHC or Halo-DIC motor complexes were tracked in living neurons using MINFLUX.

As previously outlined, the MINFLUX tracking procedure was optimized to enable the attainment of a single-digit nanometer localization precision within a time span of less than one millisecond, thus allowing for the detection of fast nanometer-sized steps (Section 3.3.1). To ensure the exclusive localization of a single emitter, the ratio of central to peripheral emission was calculated during tracking, serving as a termination condition for the localization scheme (Schmidt et al., 2021).

4.3.1 MINFLUX Tracking of the Dynein Heavy Chain

The initial dynein subunit to be examined using MINFLUX in living neurons was the DHC. First, a Halo-DHC-positive neuron was identified by the MaP555-Halo labeled dynein motors using eyepieces and LED illumination (Fig. 4.17B). By tracing all processes that originate from the soma, the axon was identified as the longest and smoothest (Fig. 4.17C). Figure 4.17C also displays a neighboring wildtype neuron discernible through tubulin staining, though without colocalization of MaP555 emission, thus corroborating the specificity of the HaloTag

labeling.

Within the selected region, multiple MINFLUX traces were obtained (Fig. 4.17D). Figure 4.17E depicts one of these MINFLUX traces, which was rotated into the on-/off-axis coordinate system via a singular value decomposition as previously described (Section 3.4.1). The steps were fitted to the traces without prior knowledge of the step size or number (Loeff et al., 2021), as indicated by the time-colored dots. Sideways steps with off-axis step sizes exceeding 6 nm, which corresponds to the width of a protofilament (Asenjo et al., 2013), are indicated by arrowheads and are perpendicular to the on-axis. The presented trace also comprises two off-axis sideways steps exceeding 25 nm in length (black arrows), which were occasionally observed. These could represent a large sideways step over multiple protofilaments at once or a transition to an adjacent microtubule, the diameter of which is approximately 25 nm (Harterink et al., 2019). The individual detected steps are visible in the on-axis displacement versus time plot, with the majority exhibiting an on-axis size of approximately 8 nm. MINFLUX traces from six independent experiments were considered for subsequent analysis, as they exhibited processive movement.

In total, traces with a length of up to 1.6 µm and a duration of 3 s were obtained in both the retrograde and anterograde directions (Fig. A.1). The localization precision for Halo-DHC motors using a pattern diameter of $L = 75$ nm was determined to be (3.5 ± 0.4) nm (median, median absolute deviation (MAD)), with a minimum localization precision of 2.3 nm. On average, (109 ± 11) photons (median, MAD) were utilized to determine the current position of the motor. As the measured photon detection rate of (100±20) kcps (median, MAD) was lower than the 125 kcps observed in preliminary experiments for which the MINFLUX localization procedure was optimized, the time resolution was (1.5 ± 0.4) ms (mean, standard deviation (SD)), thus exceeding the anticipated time resolution of 1 ms. This is possible because the MINFLUX localization procedure determines the current photons per localization and adjusts the pattern dwell time accordingly to reach the set photon threshold. Despite this, a median step size uncertainty of (2.1 ± 0.6) nm could be obtained, which is well below the observed step sizes. As a result, individual steps of endogenous dynein in living primary neurons were successfully detected using MINFLUX localization.

Figure 4.18 illustrates the marked enhancement in localization precision of MINFLUX in comparison to the established centroid (camera-based) localization precision. While a conventional camera-based localization with 109 photons would result in a precision of 26.7 nm using the Rayleigh criterion, which is insufficient for resolving individual steps of endogenous dynein, the attained MINFLUX localization precision was more than seven times smaller, thereby enabling the detection of individual steps of endogenous dynein. The localization precision of the measured MINFLUX traces of Halo-DHC are situated between the lower limit of the background-free case (Eq. 2.6) and an upper limit of the corresponding curve with background taken into account (Wirth et al., 2023) and an $SBR = 1$ or $CFR = 0.5$. It is noteworthy that some traces even approach the background-free case. This highlights

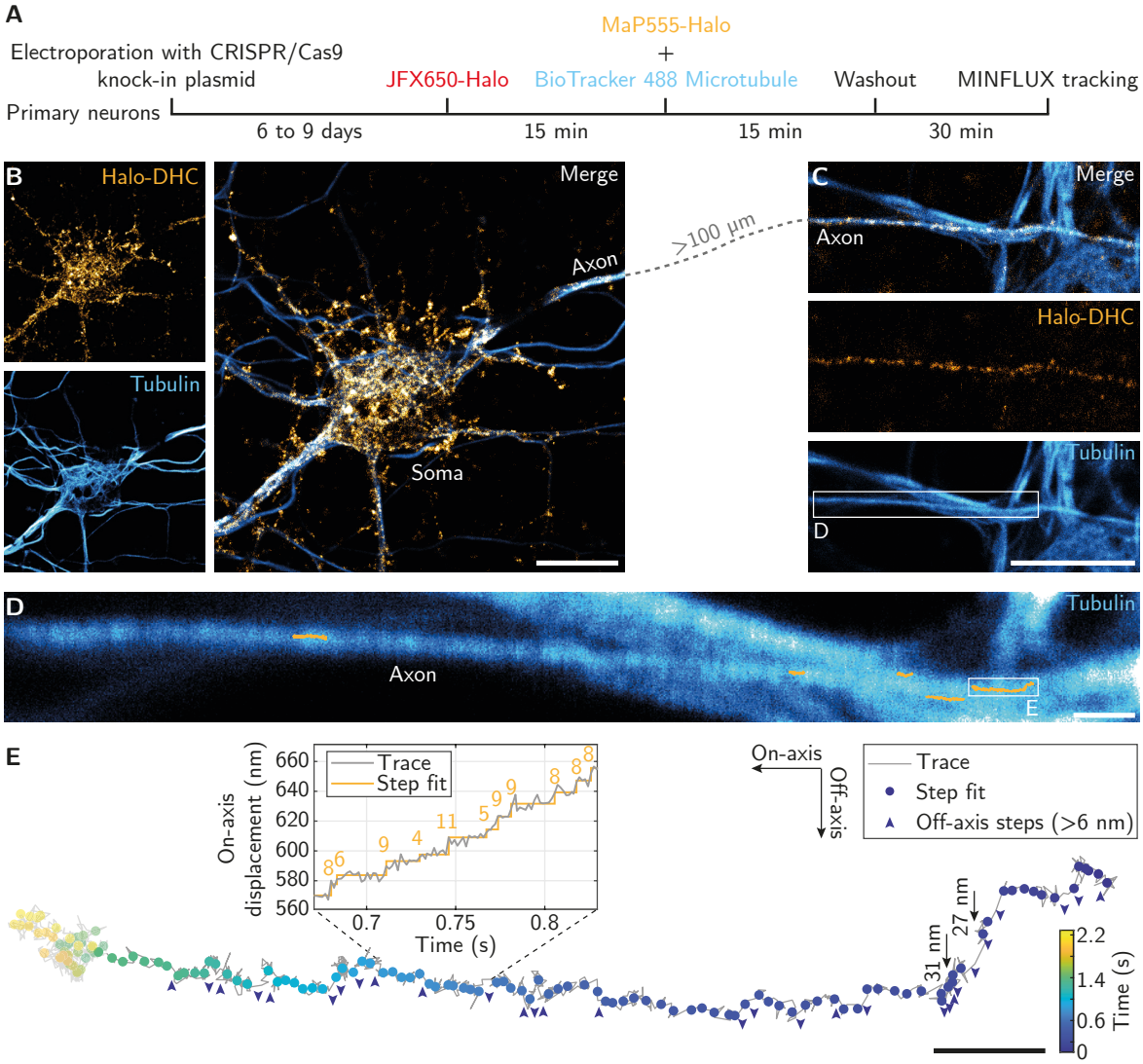

Figure 4.17 | MINFLUX tracking of endogenous dynein heavy chain
(A) Timeline of sample preparation, including electroporation of living primary neurons and live-cell labeling. **(B)** Confocal images of the soma of a Halo-DHC positive neuron, where Halo-DHC is visualized by MaP555-Halo labeling and microtubules by BioTracker 488 Green Microtubule staining. Scale bar: 10 µm. **(C)** The axon of the Halo-DHC positive neuron was identified and traced for a distance exceeding 100 µm. The overlay of Halo-DHC particles with tubulin staining demonstrates the colocalization of both, as well as the presence of a neighboring wildtype neuron devoid of the labeled Halo-DHC particles. The white box indicates the MINFLUX ROI. Scale bar: 10 µm. **(D)** MINFLUX ROI with overlaid individual MINFLUX traces (orange) that colocalized with the axon. The white box indicates the position of the representative MINFLUX trace. Scale bar: 1 µm. **(E)** The representative MINFLUX trace (successive localizations shown by a gray line) with a corresponding step fit (time color-coded dots) and sidesteps (off-axis steps larger than 6 nm, indicated by arrowheads) is shown. Two black arrows indicate large off-axis steps. The inset shows an on-axis displacement versus time plot with fitted steps. Scale bar: 100 nm.

the necessity of employing MINFLUX localization for the detection of individual steps of endogenous, and thus unrestrictedly fast, dynein.

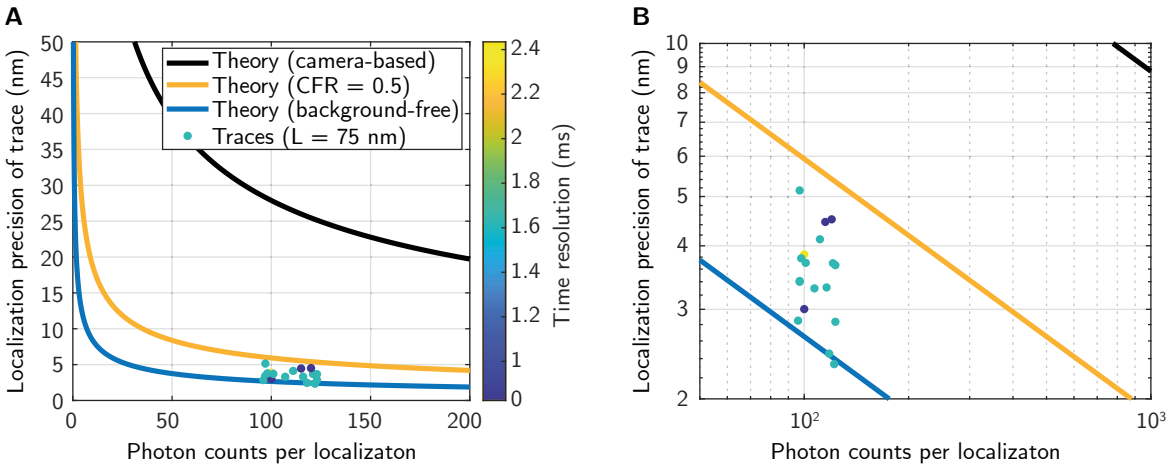

Figure 4.18 | Localization precision of dynein heavy chain MINFLUX traces
(A) A plot of localization precision versus photon counts per localization demonstrates the theoretical limits of camera-based localization (black) in comparison to MINFLUX-based localization (blue: background-free, orange: background considered with $CFR = 0.5$ or $SBR = 1$). Individual Halo-DHC MINFLUX traces (n = 18) are represented by dots, which are color-coded by their corresponding time resolution. **(B)** The same plot as shown in (A) with logarithmic axes.

The speed of Halo-DHC motors tracked with MINFLUX was found to be similar in both the retrograde and anterograde directions (Fig. 4.19). While comparable, the speed observed was slower than that determined through widefield measurements (Fig. 4.16). This discrepancy may be attributed to the potential for extremely fast particles to be missed by the MINFLUX localization procedure.

To assess the stepping behavior of endogenous dynein in living neurons, the MINFLUX traces of Halo-DHC motors were divided into retrograde and anterograde segments, with processive motion exceeding 50 nm. The minimal on-axis displacement anticipated from the microtubule lattice structure is 4 nm (Fig. 4.20A). This is due firstly to the HaloTag being positioned at the N-terminus of the DHC, which represents the center of mass and is referred to as the dynein tail. Secondly, the MTBD of dynein binds to every other αβ-tubulin dimer (Carter et al., 2008), which has a diameter ranging between 8.1 nm and 8.3 nm (Alushin et al., 2014). Therefore, the expected size of an on-axis step made by the dynein tail is that of an integer multiple of half the size of the αβ-tubulin dimer. The width of a protofilament is approximately 6 nm (Asenjo et al., 2013), so sideways steps exceeding 6 nm are considered a switch to the adjacent protofilament.

The observed on-axis step sizes of retrograde segments are presented as a histogram in Figure 4.20B. The median forward step size along the on-axis was observed to be (8.0 ± 2.2) nm, with step sizes mainly between 4 nm and 16 nm. Backward steps were infrequent, with a probability of $p = 0.04$ and a smaller median step size of (5.7 ± 2.0) nm. The median

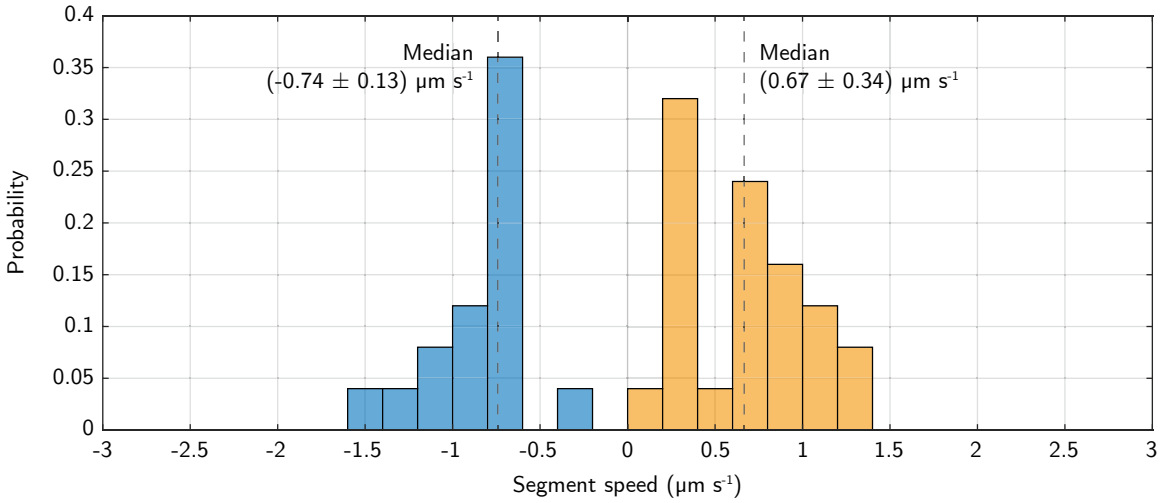

Figure 4.19 | Segment speed of dynein heavy chain MINFLUX traces
Histogram of segment speed of Halo-DHC, with retrograde segments (n = 25) color-coded in orange and anterograde segments (n = 17) in blue, and the median value indicated for both directions.

on-axis step size of the entire distribution was (7.9 ± 2.3) nm. The distribution of off-axis step sizes is centered around (0.1 ± 5.4) nm (mean, SD) and exhibits occasional sidestepping, with a probability of $p = 0.11$ to the right and $p = 0.10$ to the left (Fig. 4.20C). It is evident that the actual step size, s, was somewhat larger than the median on-axis step size, with a median value of (9.2 ± 2.6) nm (Fig. 4.20D). In addition to the primary peak, a secondary peak at approximately 12 nm is evident in the step size distribution, corresponding to a step size of the MTBD of 24 nm. The step angle, φ, was observed to be almost uniformly distributed between $-30°$ and $30°$, with a median of $\varphi = (-0.8 \pm 20.7)°$ (Fig. 4.20E). These limits are consistent with a step of 6 nm sideways and 8 nm along the on-axis, $\varphi = \arctan \frac{6\,\mathrm{nm}}{8\,\mathrm{nm}} \approx 37°$. In summary, an average step of endogenous dynein would be 8 nm in on-axis direction, thus corresponding to a 16 nm MTBD step, occasionally with a sideways component, but rarely backwards.

A subsequent analysis was conducted to ascertain the existence of potential discrepancies between consecutive steps. In the two-dimensional distributions presented in the four panels of Figure 4.21, the initial step, designated as step i, is consistently represented on the x-axis, while the subsequent step, step i+1, is depicted on the y-axis. An examination of the successive on-axis step sizes reveals a pronounced symmetry, with a peak occurring at approximately 8 nm (Fig. 4.21A). This indicates that following an initial 8 nm step along the on-axis, another 8 nm step is likely to follow. Secondly, the two-dimensional off-axis distribution also exhibits symmetry, with the majority of steps situated around 0 nm (Fig. 4.21B). This observation suggests that there was no evidence of left-right wobbling. The consecutive actual step sizes also appear to be symmetric, similar to the consecutive on-axis step sizes, with an initial 8 nm to 10 nm step followed by another step of similar size (Fig. 4.21C). In the

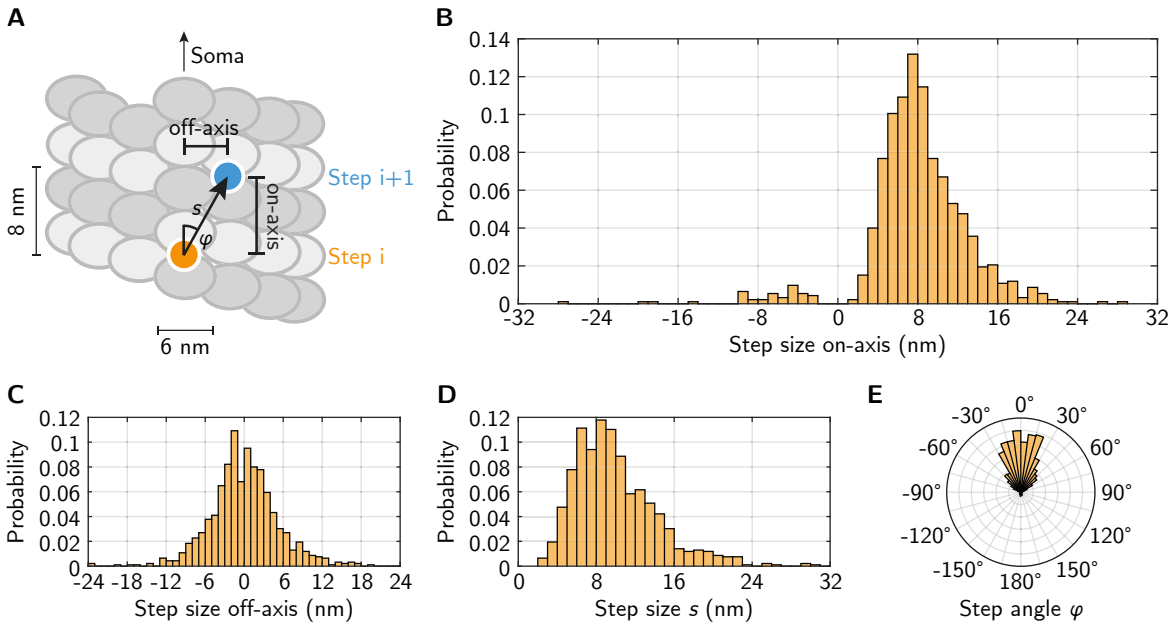

Figure 4.20 | Stepping behavior of dynein heavy chain
(A) Schematic representation of the microtubule lattice with a step of size *s*. The on- and off-axis step sizes are indicated, as well as the step angle *φ*. **(B)** On-axis step size histogram of Halo-DHC. **(C)** Step size histogram of off-axis step sizes of Halo-DHC. **(D)** Histogram of actual step sizes *s* of Halo-DHC. **(E)** Step angle distribution of Halo-DHC (n = 925 for all histograms).

last panel, the consecutive step angle also appears to be symmetricly centered, similar to the consecutive off-axis steps, which again indicates the absence of alternating left-right wobbling (Fig. 4.21D). Collectively, this indicates that each step of endogenous dynein is independent of the subsequent one, as there were no notable asymmetries.

Finally, the dwell time between consecutive steps was investigated. The distribution of dwell times appears to be exponentially decaying, although it seems that the first bin is underrepresented (Fig. 4.22A). This will be examined in greater detail in the following section (Section 4.3.4). In any case, the succession of steps occurs with remarkable rapidity, with half of the steps occurring in less than 7.4 ms. In total, endogenous dynein dwells for less than 100 ms before stepping again. When examining the consecutive dwell times, no asymmetry was observed, with the majority occurring within a range of 2.5 ms to 7.5 ms (Fig. 4.22B). This corroborates the previous finding regarding consecutive step sizes, indicating that consecutive dwell times are independent of each other, that is, there are no alternating fast and slow steps, but rather consecutive steps with similar dwell times.

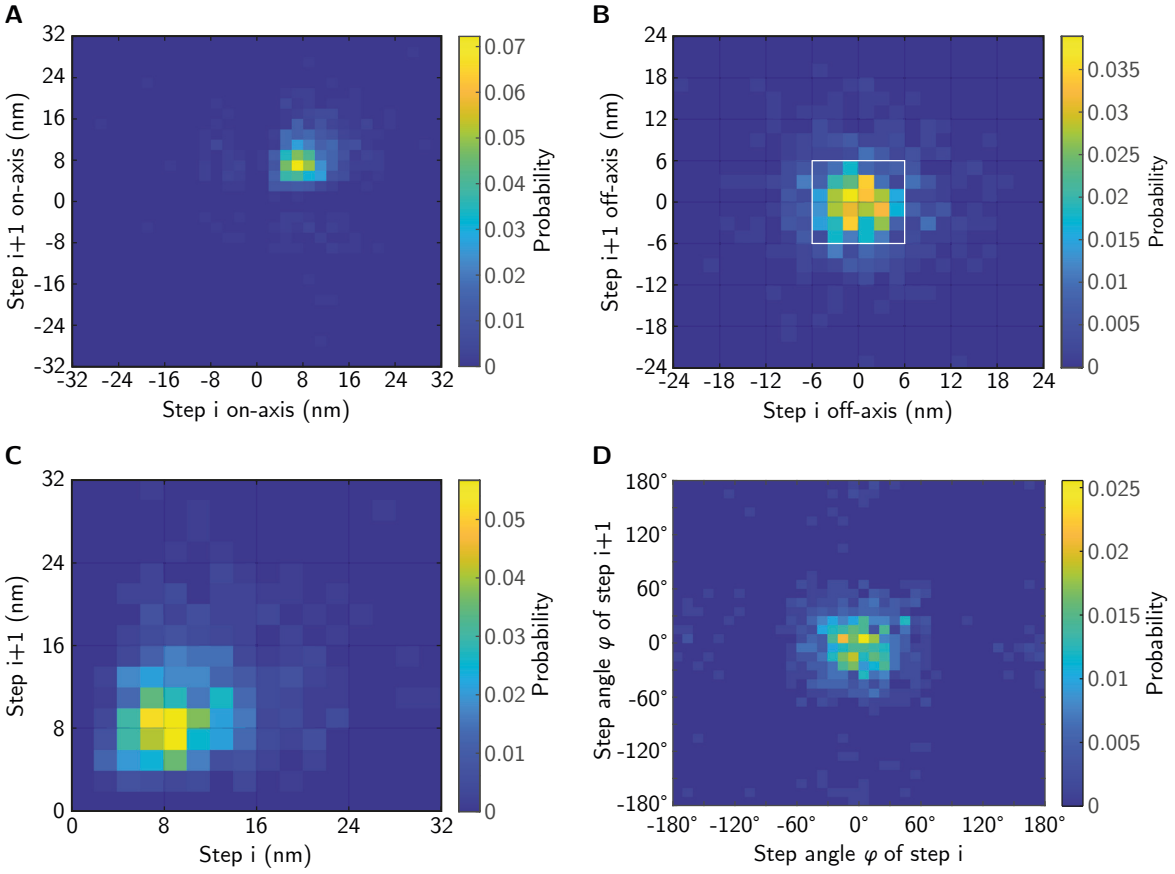

Figure 4.21 | Consecutive stepping of dynein heavy chain
(A) A two-dimensional histogram of consecutive on-axis step sizes of Halo-DHC, with the initial step (i) on the x-axis and the subsequent step (i+1) on the y-axis. The corresponding probabilities are color-coded. **(B)** Two-dimensional histogram of consecutive off-axis step sizes. The white box indicates off-axis steps between −6 and 6 nm, which correspond to the limits of the same protofilament. **(C)** Two-dimensional histogram of consecutive step sizes s. **(D)** Two-dimensional histogram of consecutive step angles φ.

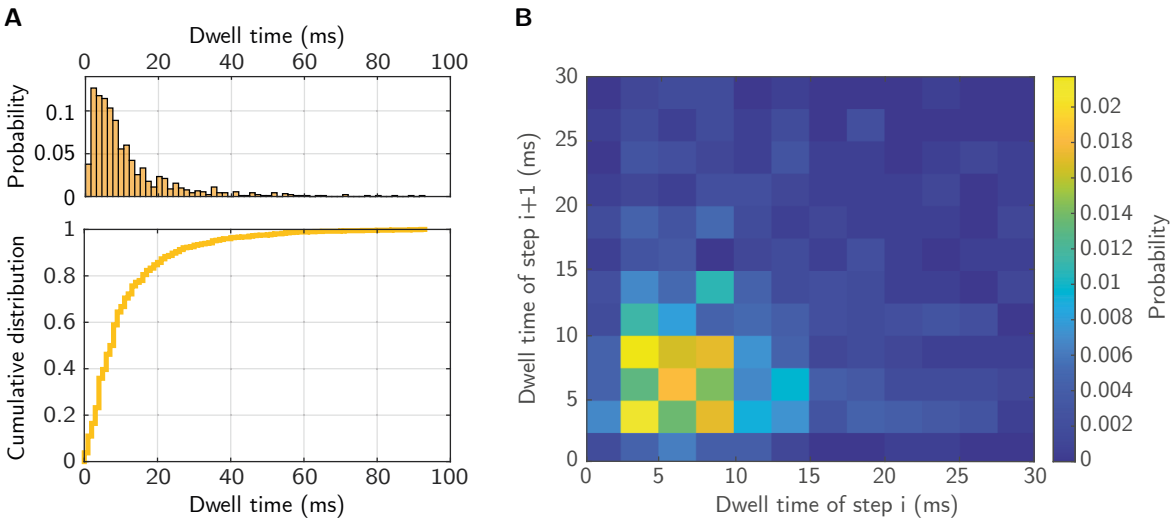

Figure 4.22 | Dwell time analysis of dynein heavy chain
(A) The upper panel depicts the dwell time histogram of Halo-DHC, while the lower panel illustrates the corresponding cumulative distribution of dwell times between consecutive steps (n = 900). **(B)** The two-dimensional histogram of consecutive dwell times is presented with color-coded probability.

4.3.2 MINFLUX Tracking of the Dynein Intermediate Chain

In addition to the DHC, the DIC was also tracked with MINFLUX to gain insight into its stepping behavior and identify potential differences between the two subunits during motility. To facilitate a comparative analysis of the dynamics of the two subunits, the identical sample preparation and labeling procedure was employed (Fig. 4.17A). In this instance, however, living primary neurons were electroporated with the pO-Halo-DIC CRISPR/Cas9 knock-in plasmid, which resulted in the tagging of the DIC at its N-terminus with a HaloTag, as had been demonstrated previously (Section 4.2.1). Figure 4.23A depicts a representative Halo-DIC-positive neuron, demonstrating the MaP555-Halo labeling of Halo-DIC and tubulin staining. It should be noted that the tubulin image does not show the microtubules of the soma, which were located at a different focal plane than those of the axon, which are shown here. As previously, the axon was identified as the longest and smoothest process, and a ROI for MINFLUX tracking was selected at a distance of at least 100 µm from the soma (Fig. 4.23B). It should be noted that the tubulin staining in Figure 4.23B also reveals a neighboring wild-type neuron; however, there is no colocalization of MaP555 labeling. This indicates the specificity of the HaloTag labeling. A single trace was selected from the MINFLUX region for subsequent analysis (Fig. 4.23C). Figure 4.23D presents the MINFLUX trace in detail, with corresponding color-coded step fits. It should be noted that the raw trace with all corresponding step fits is shown here. Consequently, the representation illustrates parts that were not considered in the segmentation analysis. The retrograde section in the middle of the trace, where the on-axis displacement versus time graph is taken from, appears disordered due to the presence of two direction reversals from anterograde to retrograde movement and

retrograde to anterograde. In total, MINFLUX traces from twelve independent experiments have been considered for subsequent analysis, exhibiting processive movement.

The localization precision of the Halo-DIC MINFLUX traces was determined to be (4.2 ± 0.5) nm (median, MAD), with a minimum of 2.8 nm. This value is slightly higher than that of Halo-DHC, which can be attributed to the lower number of photons per localization (91 ± 11), which is indirectly proportional to the localization precision via the square root. Furthermore, the time resolution was higher, at (1.1 ± 0.4) ms (mean, SD), compared to the MINFLUX traces of Halo-DHC, reaching the anticipated limit of 1 ms. This is likely attributable to a markedly higher photon detection rate of (167 ± 33) kcps (median, MAD), which was achievable during MINFLUX tracking. In accordance with the MINFLUX traces of Halo-DHC, the localization precision of the Halo-DIC MINFLUX traces were situated between the lower background-free curve and the upper curve, where background was taken into account (Fig. 4.24). In any case, all MINFLUX traces of Halo-DIC exhibited a localization precision that was markedly higher than what would be expected for camera-based methods. This allowed for the detection of inherently fast dynein steps in living neurons. In combination, the step size detection uncertainty of (2.3 ± 0.6) nm (median, MAD) is considerably below the anticipated step sizes of Halo-DIC motors, while the time resolution of (1.1 ± 0.4) ms is well below the expected dwell times. This enables the detection of individual steps of Halo-DIC motors, as was previously observed for Halo-DHC motors.

Once more, Halo-DIC MINFLUX traces were divided into segments of processive retrograde and anterograde movement to facilitate a detailed investigation of the stepping behavior. The speed of these segments was found to be similar in both directions (Fig. 4.25), and comparable to that of Halo-DHC (Fig. 4.19), reaching speeds of up to $2.9\,\mu m\,s^{-1}$, which is similar to the fastest particles observed with the widefield microscope (Fig. 4.13). However, it should be noted that the median speed is considerably slower than that observed using the widefield microscope. Despite the spatiotemporal precision achieved with MINFLUX, it is possible that very fast particles may still be missed.

In order to investigate the stepping behavior of Halo-DIC motors, an analysis was conducted on the steps within the retrograde segments. The on-axis step size distribution exhibits two principal peaks at 8 nm and 12 nm, in addition to a minor peak at approximately 16 nm (Fig. 4.26B). The majority of backsteps were observed to be between 4 nm and 8 nm in size. In comparison to the on-axis distribution of Halo-DHC, the present distribution exhibits a broader range of step sizes and a higher probability of backsteps ($p = 0.15$). Similarly, the off-axis step size distribution is broader, with a mean of (-0.4 ± 8.0) nm (mean, SD) and a pronounced peak at 6 nm (Fig. 4.26C), corresponding to a sidestep to the adjacent protofilament. The probabilities for sidestepping were markedly higher than those observed for Halo-DHC, with $p = 0.20$ to the left and $p = 0.16$ to the right. As with the on-axis step size distribution, the distribution of actual step sizes exhibits a peak at approximately 8 nm and one at approximately 12 nm (Fig. 4.26D), which is even more pronounced than that of the on-axis step size

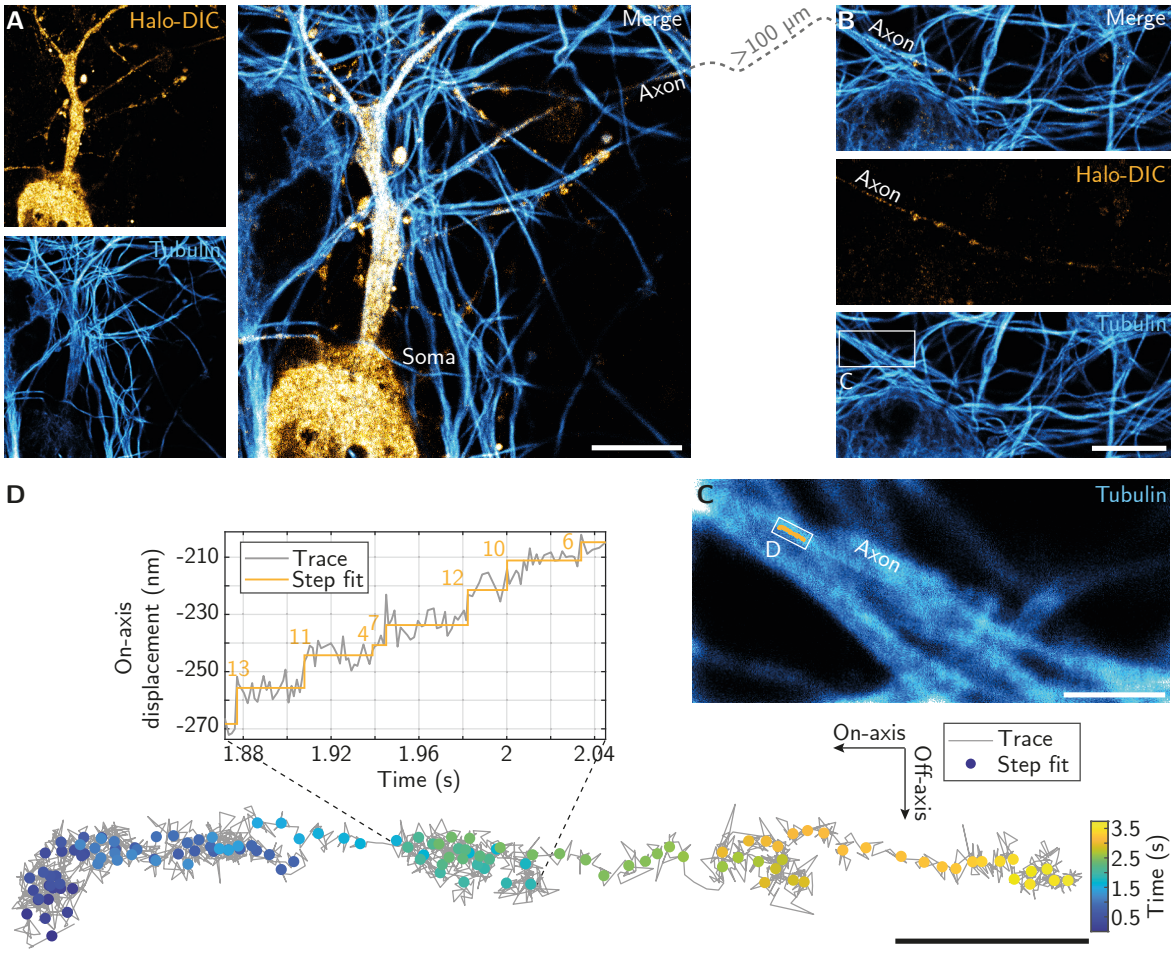

Figure 4.23 | MINFLUX tracking of endogenous dynein intermediate chain
(A) Confocal images of the soma of a Halo-DIC positive neuron, where Halo-DIC is visualized by MaP555-Halo labeling and microtubules by BioTracker 488 Green Microtubule staining. Scale bar: 10 µm. **(B)** The axon of the Halo-DIC positive neuron was identified and traced for a distance exceeding 100 µm. The overlay of Halo-DIC particles with tubulin staining demonstrates the colocalization of both, as well as the presence of a neighboring wildtype neuron devoid of the labeled Halo-DIC particles. The white box indicates the MINFLUX ROI. Scale bar: 10 µm. **(C)** MINFLUX ROI with overlaid individual MINFLUX trace (orange) that colocalized with the axon. The white box indicates the position of the representative MINFLUX trace. Scale bar: 2 µm. **(E)** The representative MINFLUX trace (successive localizations shown by a gray line) with a corresponding step fit (time color-coded dots) is shown. The inset shows an on-axis displacement versus time plot with fitted steps. Scale bar: 100 nm.

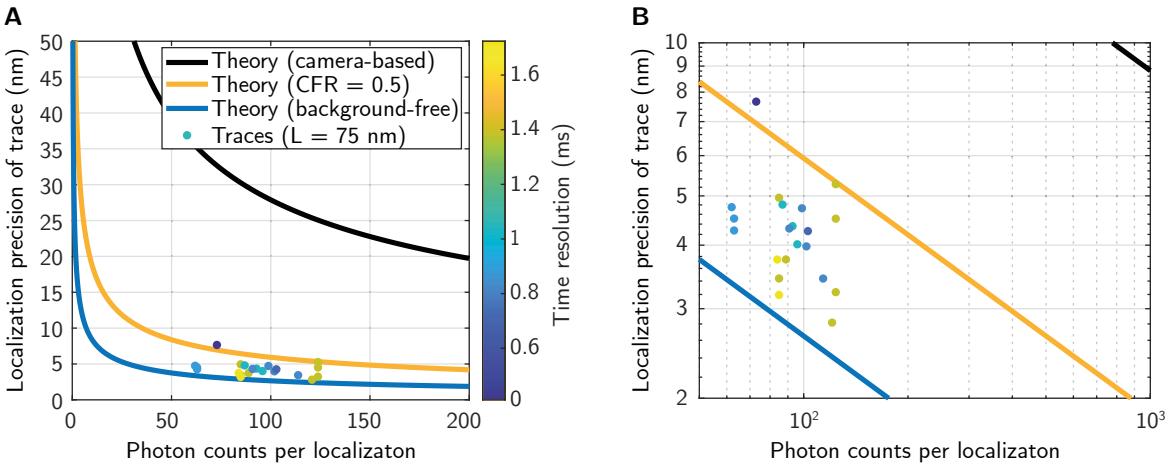

Figure 4.24 | Localization precision of dynein intermediate chain MINFLUX traces
(A) A plot of localization precision versus photon counts per localization demonstrates the theoretical limits of camera-based localization (black) in comparison to MINFLUX-based localization (blue: background-free, orange: background considered with $CFR = 0.5$ or $SBR = 1$). Individual Halo-DIC MINFLUX traces (n = 21) are represented by dots, which are color-coded by their corresponding time resolution. **(B)** The same plot as shown in (A) with logarithmic axes.

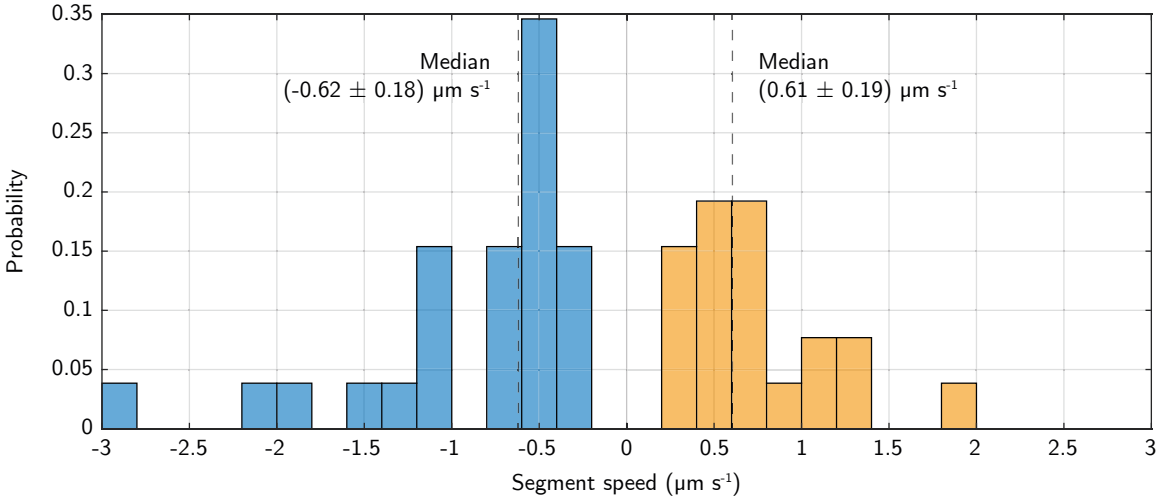

Figure 4.25 | Segment speed of dynein intermediate chain MINFLUX traces
Histogram of segment speed of Halo-DIC, with retrograde segments (n = 20) color-coded in orange and anterograde segments (n = 26) in blue, and the median value indicated for both directions.

distribution. It is evident that the actual step size distribution of Halo-DIC is broader than that of Halo-DHC, indicating larger steps with a median of $s = (11.8 \pm 3.4)$ nm. The angular distribution of Halo-DIC exhibits larger step angles than that of Halo-DHC, including a slight left-hand bias, as evidenced by the median angle of $\varphi = (-3.4 \pm 26.7)^\circ$ (Fig. 4.26E).

In conclusion, the on-axis step sizes exhibited a median of (9.8 ± 3.1) nm, which was larger than the (8.0 ± 2.2) nm observed for Halo-DHC. Additionally, the off-axis step size distribution of Halo-DIC was broader than that of Halo-DHC, with a SD of 8.0 nm compared to 5.4 nm for Halo-DHC. Furthermore, the occurrence of backsteps was more prevalent, and they were larger in size with (-7.4 ± 2.1) nm compared to those observed in Halo-DHC with (-5.7 ± 2.0) nm. This suggests that the N-terminus of the DIC exhibits greater flexibility during movement than the dynein tail (DHC N-terminus).

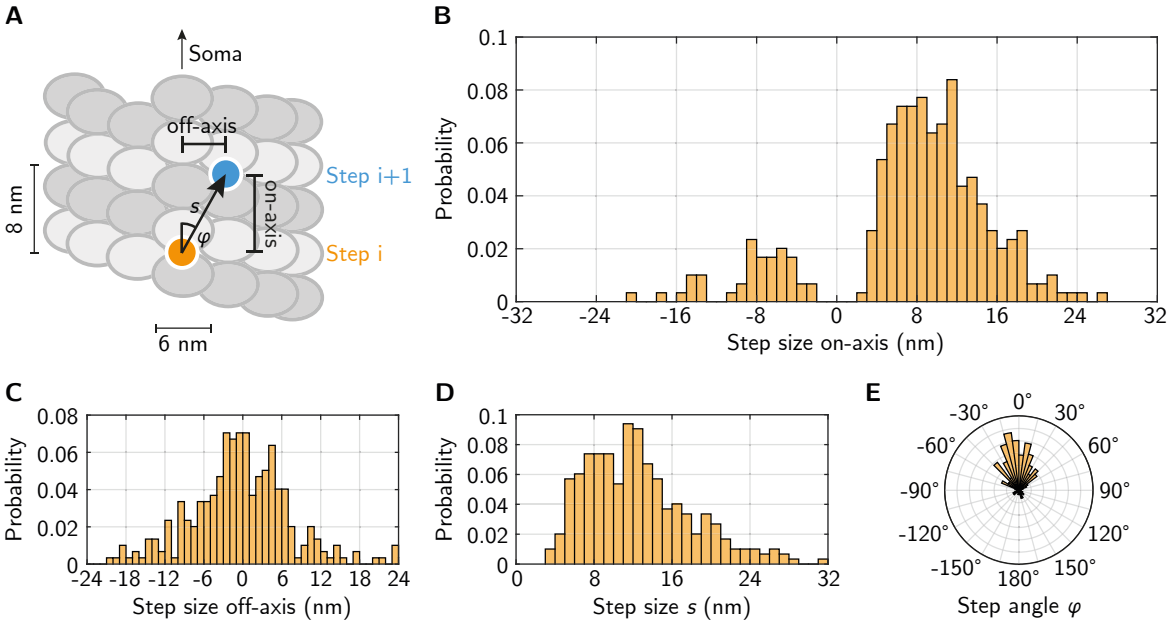

Figure 4.26 | Stepping behavior of dynein intermediate chain
(A) Schematic representation of the microtubule lattice with a step of size *s*. The on- and off-axis step sizes are indicated, as well as the step angle φ. **(B)** On-axis step size histogram of Halo-DIC. **(C)** Step size histogram of off-axis step sizes of Halo-DIC. **(D)** Histogram of actual step sizes *s* of Halo-DIC. **(E)** Step angle distribution of Halo-DIC (n = 298 for all histograms).

As previously, an analysis was performed to identify any asymmetries present in consecutive steps of the DIC. In the two-dimensional histogram of the on-axis steps, it can be observed that the majority of initial 8 nm steps are followed by another 8 nm step. However, there is also a less probable occurrence of an initial 12 nm step followed by another 12 nm step (Fig. 4.27A). Moreover, it can be discerned that there is a slight probability of a forward step of 8 nm followed by a backward step of −8 nm, as well as an initial backward step of −8 nm followed by another −8 nm backward step. The latter two possibilities, which were not discernible in the plot of the DHC, are likely attributable to the fact that the DIC exhibited a

greater prevalence of backsteps than the DHC. With regard to the consecutive off-axis steps, the highest probability was observed within the range of −6 nm to 6 nm (Fig. 4.27B). As was observed previously in both the off-axis step size and angular distributions (Fig. 4.26C, E), a slight left-handed bias is evident in the two-dimensional histogram of the consecutive off-axis steps, indicating that a left swing is followed by a centered step. Upon examination of the consecutive actual step sizes, three primary probabilities emerge. The predominant probability is an initial 12 nm step followed by another 12 nm step (Fig. 4.27C). The remaining probabilities are an initial 8 nm step followed by another 8 nm step and an initial 12 nm step followed by an 8 nm step. The consecutive step angles are predominantly distributed around 0°, exhibiting no discernible asymmetries (Fig. 4.27D). Overall, consecutive steps of Halo-DIC were predominantly independent, with each subsequent step of the same kind following the previous one. However, there were also instances where consecutive steps were unequal in size compared to the Halo-DHC motors.

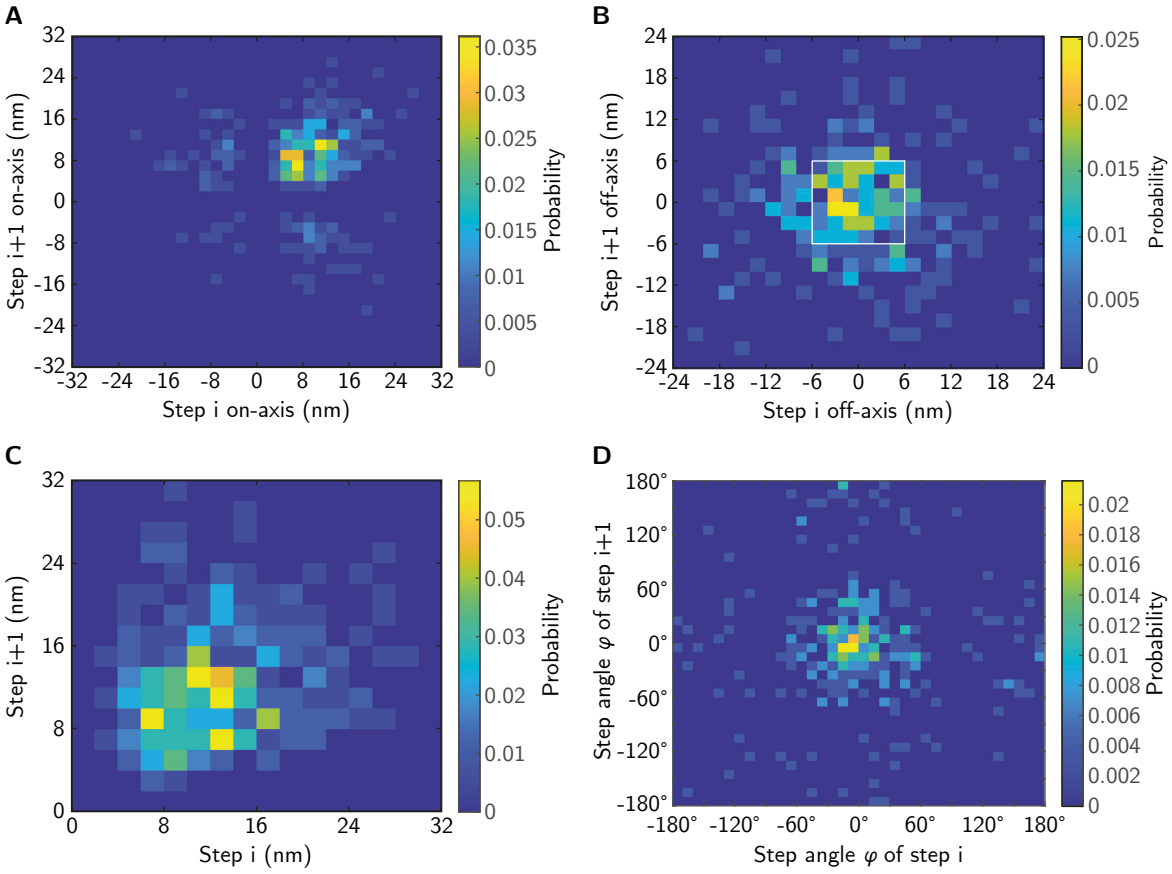

Figure 4.27 | Consecutive stepping of dynein intermediate chain
(A) A two-dimensional histogram of consecutive on-axis step sizes of Halo-DIC, with the initial step (i) on the x-axis and the subsequent step (i+1) on the y-axis. The corresponding probabilities are color-coded. **(B)** Two-dimensional histogram of consecutive off-axis step sizes. The white box indicates off-axis steps between −6 and 6 nm, which correspond to the limits of the same protofilament. **(C)** Two-dimensional histogram of consecutive step sizes s. **(D)** Two-dimensional histogram of consecutive step angles φ.

Finally, the dwell time between consecutive steps was examined. The dwell time distribution of Halo-DIC appears to be comparable to that of Halo-DHC, exhibiting a distribution similar to an exponential decay (Fig. 4.28A). A half of the dwell times lasted for a duration of less than 6.9 ms, which is comparable to what was observed in Halo-DHC motors. Furthermore, the consecutive dwell times were also symmetrically distributed between 2.5 and 7.5 ms (Fig. 4.28B), indicating that the stepping of endogenous dynein in living neurons is temporally independent, as revealed by MINFLUX.

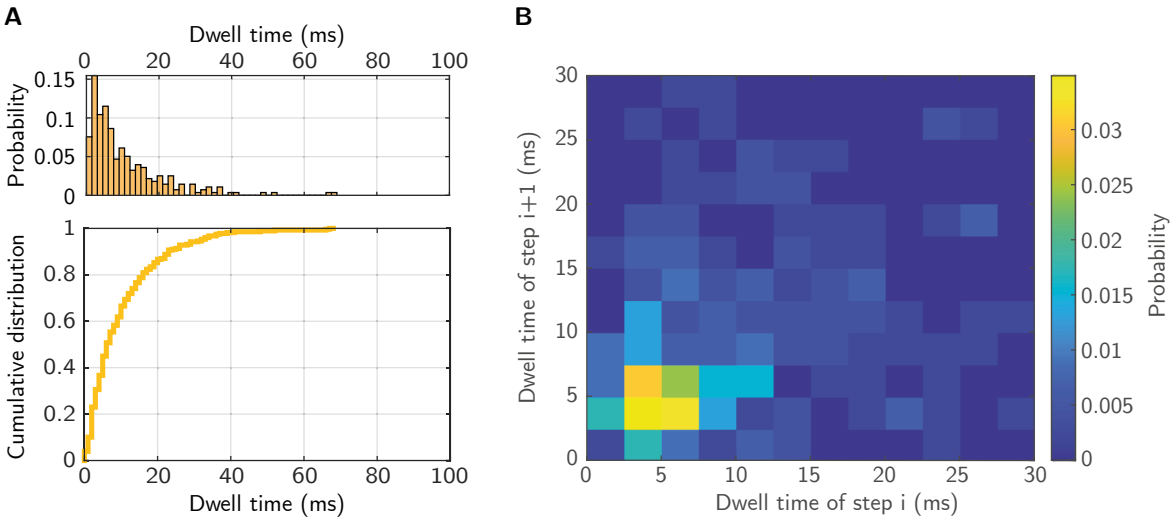

Figure 4.28 | Dwell time analysis of dynein intermediate chain
(A) The upper panel depicts the dwell time histogram of Halo-DIC, while the lower panel illustrates the corresponding cumulative distribution of dwell times between consecutive steps (n = 278). **(B)** The two-dimensional histogram of consecutive dwell times is presented with color-coded probability.

4.3.3 Examination of Pauses and Direction Reversals in Dynein Movement

The observation of bidirectional processive movement with intermittent pausing within the movement of labeled dynein across both widefield (Figs. 4.12 & 4.15) and MINFLUX measurements (Fig. 4.23D) warrants a closer examination of these pauses and direction reversals. Prior research has demonstrated that motors of opposite polarity, including both dynein and kinesin family motors, are attached to the same cargo (Hancock, 2014; Maday et al., 2014; Welte, 2004), resulting in bidirectional movement of the cargo (Encalada et al., 2011; Fu and Holzbaur, 2013; Kural et al., 2005; Maday et al., 2012). As only dynein has been tagged and labeled in this work, bidirectional movement can still be observed, in the retrograde direction as active, dynein-driven movement and in the opposite anterograde direction as kinesin-driven movement, in which dynein is attached to the cargo as a passenger. In particular, controversy remains regarding the underlying process of the observed pauses and direction reversals. One potential explanation is a stochastic process, typically referred to as a tug-of-war between opposing motors (Hendricks et al., 2010; Müller et al., 2008; Vale et al., 1992). This contrasts

with the other possibility, which is a regulated process involving adaptor or microtubule-associated proteins (Canty et al., 2023; Dixit et al., 2008; Ferro et al., 2022). Alternatively, or in addition, regulation may occur as a consequence of post-translational modification of microtubules (Guedes-Dias and Holzbaur, 2019).

To provide an indication of the two possible explanations for pauses and direction reversals, all pauses and direction reversals in the MINFLUX measurements were first categorized (Fig. 4.29). Pauses, defined as segments within a processive movement with a speed below $100\,\mathrm{nm\,s^{-1}}$ for a minimum of 100 ms, were observed in 41.0 % of all MINFLUX traces. A comparable proportion was observed for direction reversals, with 38.5 % of all traces. In both cases, the proportion of anterograde (A) and retrograde (R) movement was similar (A→A: 20.5 %, R→R: 20.5 %, A→R: 17.9 %, R→A: 20.5 %). Only 10.3 % of all traces exhibited both pauses and reversals. Furthermore, 30.8 % of all traces exhibited solely pauses, while 12.8 % displayed solely reversals. Of these, the proportions were similarly distributed between anterograde and retrograde (A→A: 15.4 %, R→R: 15.3 %, A→R: 12.8 %, R→A: 10.3 %). However, there were also highly processive traces devoid of both pauses and reversals (46.2 % of all traces). Notably, retrograde traces without any pauses or reversals (33.3 %) were observed to be almost three times more frequent than anterograde traces without any pauses or reversals (12.8 %).

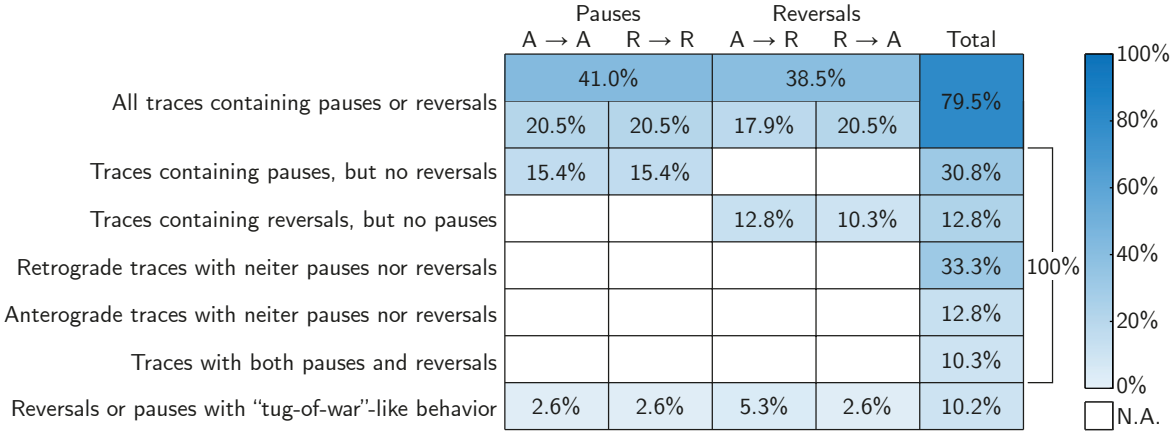

Figure 4.29 | Categorization of pauses and direction reversals in MINFLUX traces of dynein
Overview of different categories resulting from the segmentation of MINFLUX traces. It should be noted that traces present in the initial two rows may have been counted on multiple occasions, if they exhibited both pauses and reversals. In order to ensure that each trace is counted only once, the total incidence of traces with reversals but without pauses (fourth row) has been adjusted. In contrast, when distinguished after the type of reversals traces may have been counted multiple times if both types of reversals were present in the respective trace.

In comparison to conventional widefield measurements, MINFLUX permits the observation of individual steps at physiological ATP concentration within living neurons, thereby allowing the study of naturally occurring direction reversals and pauses in greater detail. Figure 4.30A illustrates four representative on-axis versus time plots, which encompass both types of pauses or direction reversals. Notably, the duration of direction reversals ((16 ± 13) ms) was on the order of the dwell time of individual steps, whereas the pause duration was approximately ten times longer ((154 ± 52) ms) (Fig. 4.30B). Pauses were, by definition, longer than 100 ms, given that this was the threshold defined a-priori based on the observation that individual steps were found to last less than 100 ms (Figs. 4.22A & 4.28A). Nevertheless, the duration of direction reversals could have been comparable to that of pauses, which was not observed. Given the observed rapidity of directional reversals, it can be inferred that a regulatory mechanism may be responsible for triggering a switch in motor activity, thereby leading to a directional reversal. This is in contrast to a proposed stochastic tug-of-war as an underlying mechanism for direction reversal. In a somewhat unexpected finding, and in contradiction to the previously stated conclusion, discrete backward and forward steps were also observed on rare occasions within both pauses and reversals (Fig. 4.30C). These constitute 10.2 % of all pauses and direction reversals (Fig. 4.29). This, in turn, leads to the suggestion that on rare occasions, a stochastic mechanical competition between motors of opposite polarity (tug-of-war) may also occur as an alternative to a regulated rapid reversal mechanism.

In order to gain a comprehensive understanding of the pauses and reversals within the context of the overall movement, two Markov chains were generated: one for the regulated reversal mechanism and the other for the unregulated, stochastic case. The transition probabilities between the states that constitute the Markov chains were calculated on the basis of both the frequency and duration of processive movements, pauses, and reversals, which were put in relation to one another. The first of the two Markov chains, which models the case of a regulatory reversal mechanism, differentiates between distinct pause and reversal states (Fig. 4.31A). To describe the unregulated stochastic mechanism (tug-of-war), the second Markov chain allows for processive movement to transition into a single pause state, from which movement can proceed in either direction (Fig. 4.31B).

Notably, the transition probabilities from either processive movement to a reversal or pause are observed to be comparable ($p_{\mathrm{A,A\to A}} \approx p_{\mathrm{A,A\to R}}$, $p_{\mathrm{R,R\to R}} \approx p_{\mathrm{R,R\to A}}$). This suggests that both pauses and reversals are similarly probable within a processive movement. However, a notable discrepancy emerges when comparing the transition probabilities from reversals or pauses back to processive movement ($p_{\mathrm{A\to A,A}} < p_{\mathrm{R\to A,A}}$, $p_{\mathrm{R\to R,R}} < p_{\mathrm{A\to R,R}}$). Pauses are approximately four times more likely to be sustained than reversals, as they last markedly longer than reversals, as previously discussed (Fig. 4.30B).

The transition matrices $\mathbf{P}$, which contain all transition probabilities (Eqs. 4.2 & 4.3), can

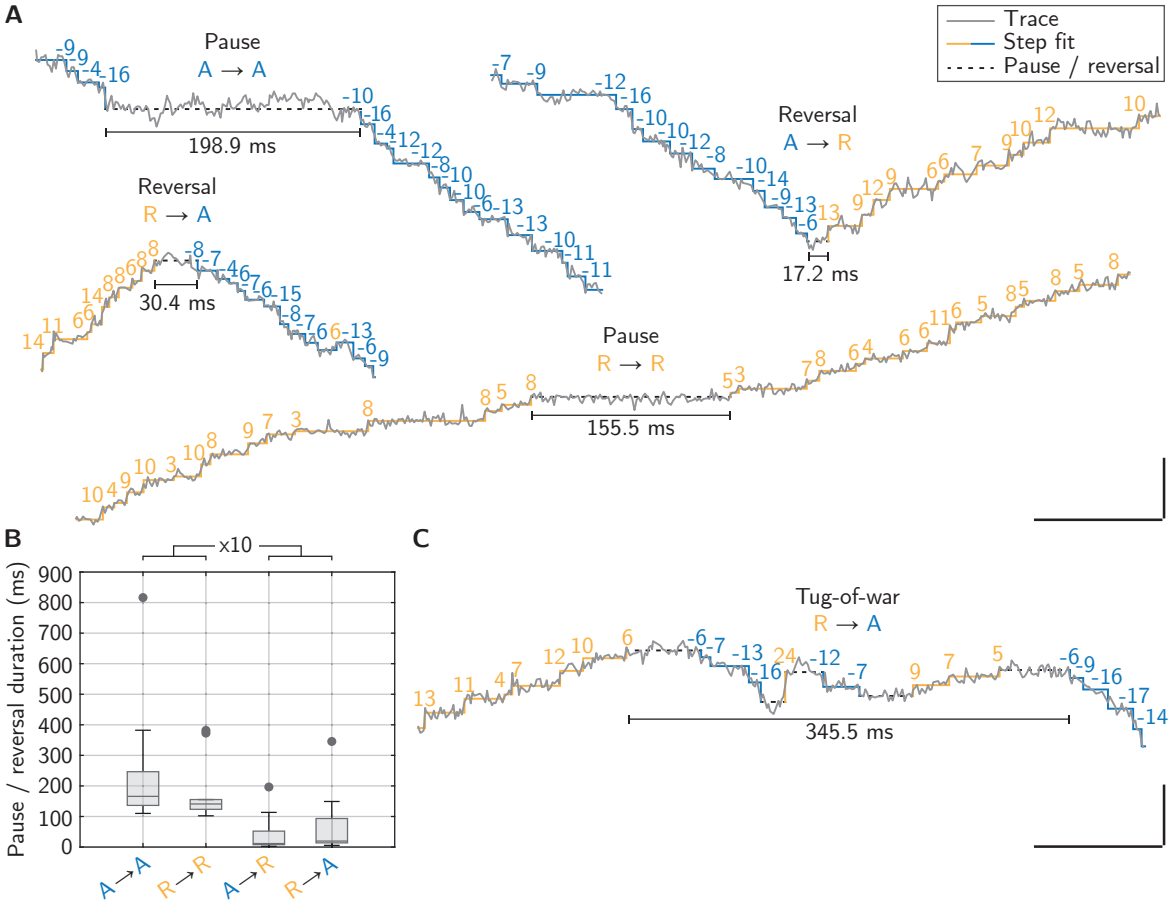

Figure 4.30 | Duration of pauses and direction reversals in MINFLUX traces of dynein
(A) Representative MINFLUX traces illustrate the occurrence of pauses within processive retrograde (R→R) and anterograde movements (A→A) and direction reversals, from anterograde to retrograde (A→R) and vice versa (R→A). The corresponding step fit is color-coded based on the movement direction (orange: retrograde, blue: anterograde). The duration of pauses and reversals is indicated below the respective pause or reversal. Scale bars: 50 nm, 100 ms. **(B)** A boxplot of all reversal and pause durations illustrates that pauses are approximately 10 times longer than reversals. Grey dots indicate outliers. **(C)** A representative excerpt from a MINFLUX trace containing a reversal that may be described as a tug-of-war. Scale bars: 50 nm, 100 ms.

be used to identify the eigenvector $\boldsymbol{\pi}$ to the eigenvalue 1.

$$\boldsymbol{\pi}\mathbf{P} = \boldsymbol{\pi} \tag{4.1}$$

$$\mathbf{P}_{\text{regulated}} = \begin{bmatrix} 0.985 & 0 & 0.007 & 0 & 0.007 & 0 \\ 0 & 0.957 & 0 & 0.023 & 0 & 0.020 \\ 0.076 & 0 & 0.924 & 0 & 0 & 0 \\ 0 & 0.062 & 0 & 0.938 & 0 & 0 \\ 0 & 0.243 & 0 & 0 & 0.758 & 0 \\ 0.274 & 0 & 0 & 0 & 0 & 0.726 \end{bmatrix} \tag{4.2}$$

$$\mathbf{P}_{\text{unregulated}} = \begin{bmatrix} 0.985 & 0 & 0.015 \\ 0 & 0.957 & 0.043 \\ 0.041 & 0.062 & 0.897 \end{bmatrix} \tag{4.3}$$

The eigenvector $\boldsymbol{\pi}$ represents the long-term, stationary probability distribution of each state. Notably, for both mechanisms, the largest stationary probability was the probability for processive movement in either direction, $\boldsymbol{\pi}_1$ and $\boldsymbol{\pi}_2$ (Eqs. 4.4 & 4.5). This indicates that, over time, dynein is most likely to be found in a processive state.

$$\boldsymbol{\pi}_{\text{regulated}} = \begin{pmatrix} 0.599 & 0.224 & 0.058 & 0.084 & 0.018 & 0.016 \end{pmatrix} \tag{4.4}$$

$$\boldsymbol{\pi}_{\text{unregulated}} = \begin{pmatrix} 0.534 & 0.275 & 0.191 \end{pmatrix} \tag{4.5}$$

Additionally, the aforementioned differences in pause and reversal transition probability highlight that reversals are shorter in duration (Fig. 4.30B) and less likely to endure than pauses (Fig. 4.31A).

In conclusion, these MINFLUX findings on endogenous dynein in living neurons at single-step resolution do not definitively resolve the controversy regarding the mechanism, stochastic or regulated, that underlies direction reversals within bidirectional axonal transport. However, the data strongly suggest a regulated rapid reversal mechanism, as this occurred with markedly higher frequency than a stochastic tug-of-war. An alternative interpretation of the findings is that they depict a scenario in which either a regulated or a stochastic mechanism occur, with the rapid regulated mechanism being the predominant one.

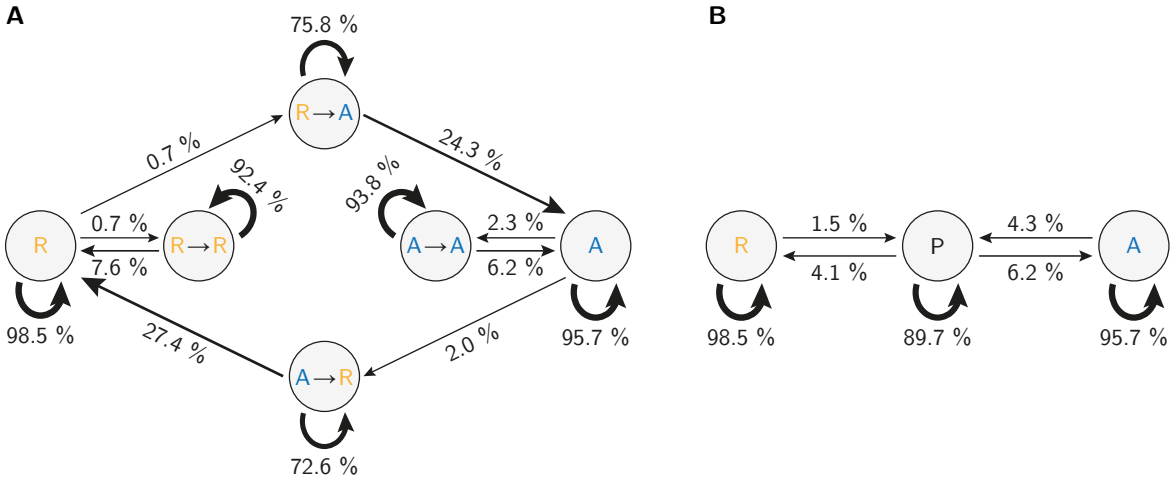

Figure 4.31 | Markov chains for the description of pause and reversal behavior
(A) Ergodic Markov chain for the regulated reversal mechanism, which encompasses the transitions between anterograde (A) and retrograde (R) segments, including transitions to reversal (R→A & A→R) and pause states (R→R & A→A). The thickness of the arrows indicates the transition probabilities between different states. **(B)** Ergodic Markov chain for the stochastic unregulated reversal mechanism (tug-of-war) depicting the transitions from anterograde (A) to retrograde segments (R) through a single stochastic pause state (P) that does not distinguish between pauses or reversals.

4.3.4 Elucidation of the Stepping Kinetics of Dynein

The question of whether the motor protein dynein consumes a single or multiple ATP molecules per step has remained a topic of contention since the initial structural investigations. This is due to the fact that the ring-shaped motor domain of dynein is, in principle, capable of binding with ATP in four of its six AAA domains (Kon et al., 2012). ATP hydrolysis between the first and second AAA domain (referred to as AAA1) has been demonstrated to be indispensable for dynein motility (Kon et al., 2004). Furthermore, it has been demonstrated that AAA3 (Bhabha et al., 2014; DeWitt et al., 2015; Nicholas et al., 2015) and AAA4 (Liu et al., 2020) play a regulatory role. However, it remains unclear whether ATP hydrolysis at AAA3 and/or AAA4 occurs in conjunction with AAA1 to perform a single step, suggesting that dynein may consume two (or more) ATPs to perform a single step (Peng et al., 2024), a hypothesis that remains a topic of debate.

To elucidate whether dynein necessitates the sequential hydrolysis of one or more ATPs to perform a single step, a comprehensive examination of the dwell times τ between successive steps of endogenous dynein was conducted. Three distinct models were utilized to describe the dwell time data: a single exponential decay and a convolution of two exponential decays with equal or unequal rate constants (Table 3.5). In order to ensure independence from the data representation, the data were fitted directly using maximum likelihood estimation, rather than the conventional approach of a non-linear least squares fit to the histogram, which would be dependent on the bin size. Akaike weights were employed as a metric for evaluating the likelihood that one of the candidate models represents the optimal fit, given the models and

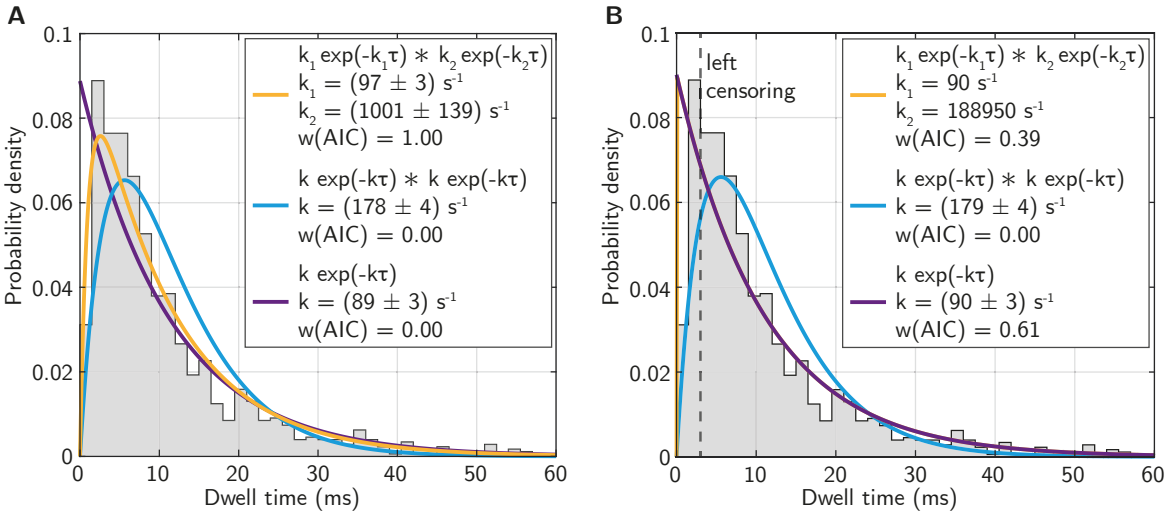

Figure 4.32 | Stepping kinetics of dynein in living neurons
(A) Histogram of dwell times (Halo-DHC and Halo-DIC) between consecutive steps with three possible models to describe the measurement data. The models were fitted to the data by maximum likelihood estimation. The orange curve represents a convolution of two exponentials with different rate constants, the cyan curve represents a convolution of two exponentials with equal rate constants, and the purple curve represents a single exponential model. The fitting parameters and Akaike weights are indicated in the legend. **(B)** Left censoring of the dwell time distribution with the same model fitting (n = 1178 & N = 18 for both histograms).

data (Burnham and Anderson, 2002).

The dwell time distribution of both Halo-DHC and Halo-DIC was best described by the model comprising a convolution of two exponentials with two distinct rate constants, k_1 being small and k_2 being large ($w(AIC) = 1.00$, Fig. 4.32A). The smaller rate constant k_1 may be attributed to the rate-limiting step within the ATPase cycle, while the higher rate constant k_2 may be ascribed to rapid cycle steps, given that the live-cell measurements were conducted at endogenous ATP concentrations and thus are not necessarily rate-limited by the binding of ATP. In accordance with this interpretation, the high rate constant k_2 is found to be in good agreement with the ATP hydrolysis and ADP dissociation rate of approximately $1000\,\mathrm{s}^{-1}$, which was previously determined in biochemical assays at saturating ATP concentrations (Holzbaur and Johnson, 1989). Furthermore, the low rate constant k_1 is consistent with the ATPase activity of recombinant dynein-dynactin-adaptor complexes (Elshenawy et al., 2019). An alternative interpretation is that some of the fastest steps ($\tau < 3\,\mathrm{ms}$), occurring on a timescale close to the temporal resolution of the measurement, may be missed and therefore underrepresented in the data. Therefore, when considering solely those steps exhibiting dwell times of $\tau > 3\,\mathrm{ms}$ (left censoring), the proposed single-exponential model, with a rate constant of $k = (90 \pm 3)\ \mathrm{s}^{-1}$, provides the optimal fit to the data ($w(AIC) = 0.61$, Fig. 4.32B). This results in the low rate constant k_1 of the model of two convolved exponentials with two distinct rate constants becoming equal to the rate constant k of the single exponential model. Similarly, the same conclusions can be drawn when the dwell time data for Halo-DHC and

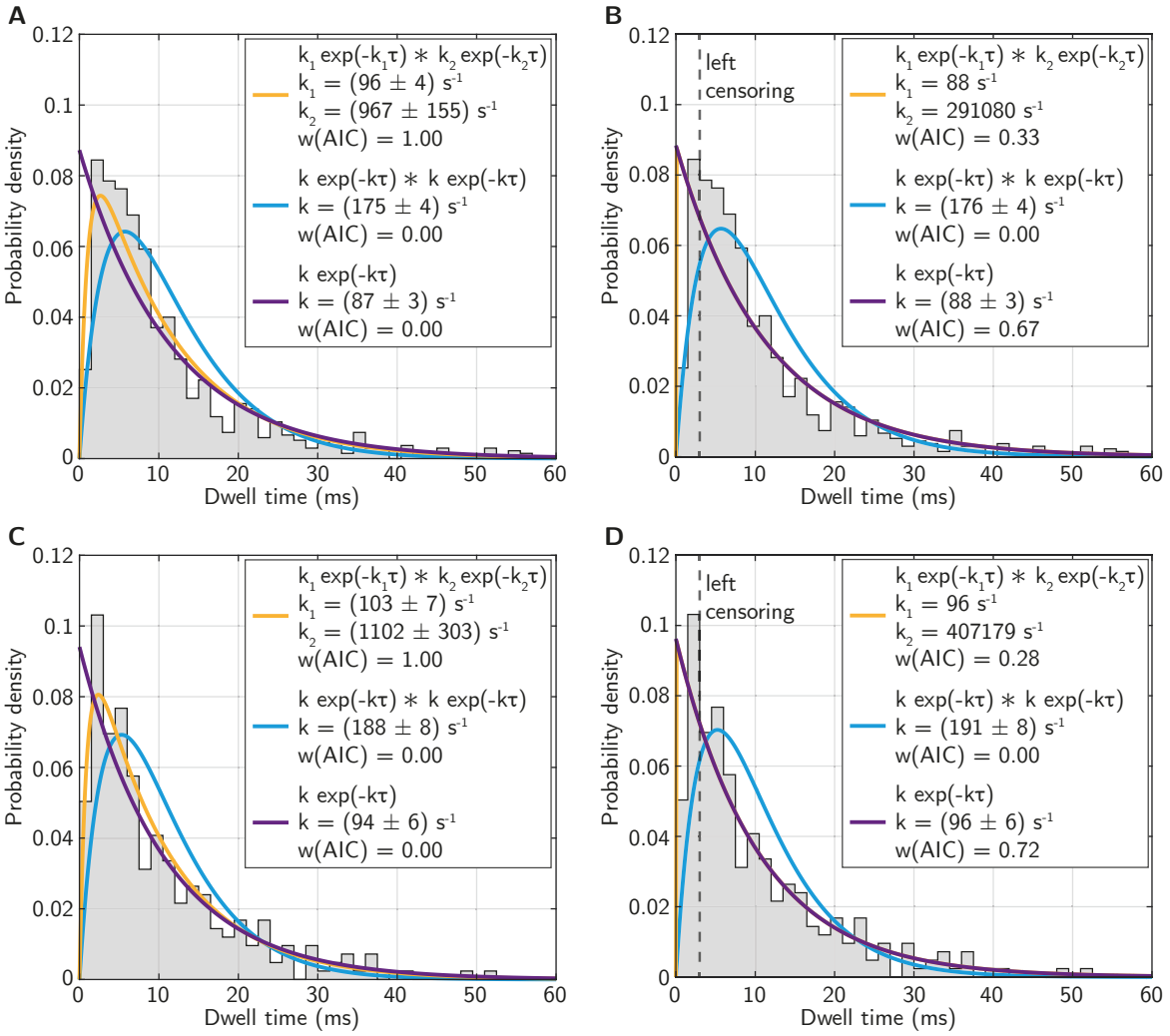

Figure 4.33 | Stepping kinetics of dynein heavy and intermediate chain in living neurons
(A) Dwell time histogram (Halo-DHC) with three possible models fitted to the data by maximum likelihood estimation. The fitting parameters and Akaike weights are indicated in the legend. **(B)** Left censoring of the dwell time distribution (Halo-DHC) with the same model fitting (n = 900 & N = 6 for both histograms). **(C)** Dwell time histogram (Halo-DIC) with three possible models fitted to the data by maximum likelihood estimation. The fitting parameters and Akaike weights are indicated in the legend. **(D)** Left censoring of the dwell time distribution (Halo-DIC) with the same model fitting (n = 278 & N = 12) for both histograms).

Halo-DIC are considered separately (Fig. 4.33).

In order to verify the fitting procedure, a gamma distribution of degree two was simulated, which would describe two processes with the same rate occurring consecutively. This corresponds to the situation in which dynein would require two ATP molecules to be hydrolyzed consecutively in order to perform a single step. When fitting the simulated distribution, the model of two convolved exponentials with the same rate was found to be the best fitting model ($w(AIC) = 0.73$, Fig. 4.34). This firstly confirms that the maximum likelihood fitting procedure, assessed by Akaike weights, did indeed identify the underlying model correctly, and secondly indicates that the model of two convolved exponentials with the same rate was not an adequate description of the measured dwell time data.

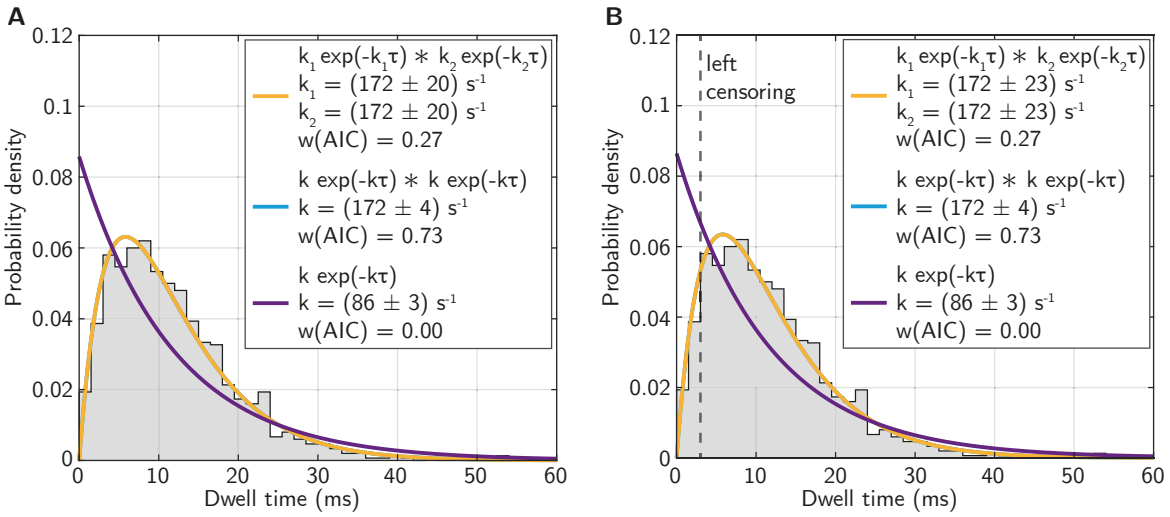

Figure 4.34 | Simulated gamma distribution
(A) Dwell time histogram of a simulated gamma distribution of degree 2 with three possible models fitted to the data by maximum likelihood estimation. The fitting parameters and Akaike weights are indicated in the legend. **(B)** Left censoring of the dwell time distribution with the same model fitting (n = 1000 for both histograms).

In conclusion, the measured dwell time between consecutive steps of endogenous dynein is best described by either a convolution of two exponentials with distinct rate constants or a single exponential. Both models indicate that a single rate-limiting process underlies the stepping kinetics of dynein, suggesting that the hydrolysis of a single ATP molecule is required to perform a single step. However, it should be noted that additional ATP molecules may be hydrolized independently, which are consequently not necessary for the performance of the step but may serve regulatory purposes.

4.3.5 Consideration of the Step Size in Relation to the Microtubule Lattice

Given that dynein is a microtubule-associated motor with its MTBD specifically binding between αβ-tubulin dimers with defined dimensions (Alushin et al., 2014; Carter et al., 2008),

it is reasonable to hypothesize that the steps might follow the periodic lattice formed by the microtubules. The two most prominent models that have been proposed to describe the stepping of dynein are the "alternating shuffle" model (Reck-Peterson et al., 2006), in which both MTBDs alternately take steps that are twice as large as the tail, and an uncoordinated model (DeWitt et al., 2012; Qiu et al., 2012), in which the MTBDs can independently perform steps. Consequently, in both models, the dynein tail (Halo-DHC) would perform steps half the size of those of the MTBD (Fig. 4.35A).

In order to ascertain whether or not the dynein tail follows the size of the microtubule lattice, the on-axis step size distribution of the dynein tail (Halo-DHC) was fitted using a Gaussian Mixture Model, without prior knowledge of the number or parameters of the fitted Gaussians (Fig. 4.35B). To identify the optimal Gaussian components, the AIC was calculated for 1,000 fitting runs, serving as a measure of goodness of fit. Indeed, the optimal Gaussian components exhibit step sizes of a 4 nm increment, within uncertainty boundaries, that range between 4 nm and 16 nm. This suggests that the dynein tail performs steps that align with the periodicity of the half-size microtubule lattice, specifically steps of a 4 nm increment and steps that are half the size of the MTBD.

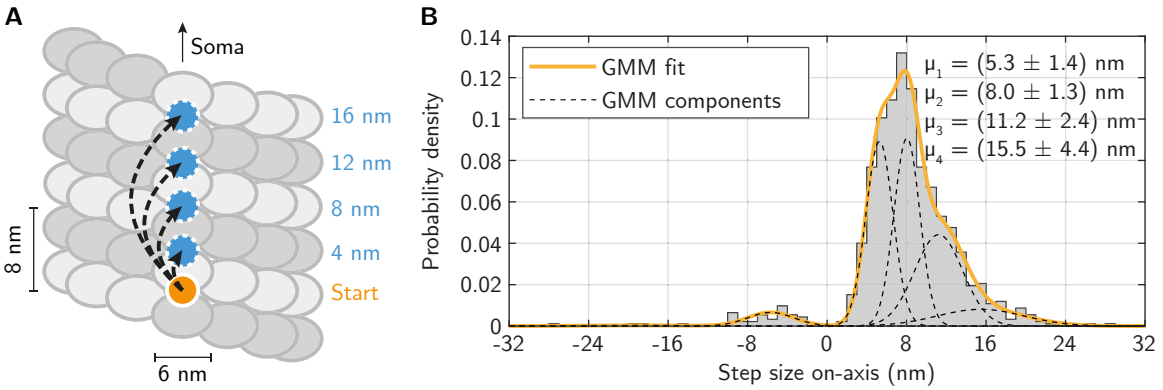

Figure 4.35 | Gaussian mixture model analysis of the dynein tail step sizes
(A) Schematic representation of the microtubule lattice with four possible step sizes of the dynein tail (Halo-DHC) in the retrograde direction. The step sizes are separated by an increment of 4 nm, thus matching the periodicity of the microtubule lattice. **(B)** The on-axis step size distribution of the dynein tail (Halo-DHC) was fitted by a Gaussian Mixture Model (GMM), as illustrated by the orange line, whose components (dashed lines, forward components: mean ± SD) represent the optimal composition of the distribution.

As the discrete steps of 4 nm increment might be obscured and their peaks might overlap due to the finite localization precision of the MINFLUX measurement, the hypothesis that the on-axis step size distribution comprises several Gaussian components is additionally investigated through simulation. To this end, a MINFLUX trace comprising 1,000 steps of 4 nm increment, whose probability of occurrence matches that of the fitted Gaussian components, is simulated (Fig. 4.36A). The dwell time between these steps was randomly selected from an exponential distribution with a decay constant of $k = 90\,\mathrm{s}^{-1}$ (Fig. 4.36B), which corre-

sponds to the observed rate constant of the measurement (Fig. 4.35B). To account for the localization precision of the measurement, noise was added to the simulated trace accordingly. Subsequently, the steps within the noisy trace were fitted using the same procedure that had been used for the measurement.

The resulting step size distribution of the simulation (Fig. 4.36C) exhibits a high degree of similarity to the measured distribution depicted in Figure 4.35B. As a consequence of the finite localization precision, the discrete 4 nm steps appear to be smeared out. When a Gaussian mixture model was fitted to the simulated data, as was done previously (Fig. 4.36C), the first three resulting Gaussian components resembled the discrete 4 nm incremental steps within the uncertainty boundaries. The fitted Gaussian components are also analogous to those observed in the measured distribution. Furthermore, the distribution of dwell times (Fig. 4.36D) is comparable to that of the initial simulation input and to that of the measurement (Fig. 4.22A). Similarly, when the simulated data are fitted using maximum likelihood estimation in a manner analogous to that employed for the measured dwell time distribution, comparable observations are evident. The model that best fits the data according to Akaike weights is a convolution of two exponentials with different rate constants (orange curve in Fig. 4.36E), with the single exponential model (purple curve) exhibiting a high degree of similarity for larger dwell times. However, very small dwell times ($\tau < 3\,\mathrm{ms}$) seem underrepresented when assuming the exponential decay as underlying model. Consequently, when these short dwell times are excluded from the fitting process (Fig. 4.36F), the single exponential model emerges as the optimal fit, with a rate constant of $k = (80 \pm 3)\ \mathrm{s}^{-1}$. This rate constant is also comparable to that observed in the measurement. In all instances, the convolution of two exponentials with an identical rate constant (cyan curve), corresponding to a consumption of 2 ATPs to perform a single step, failed to adequately represent the distributions.

By assuming a stepping behavior comprising 4 nm increment steps with a dwell time that is single exponentially distributed (1 ATP/step), which was implemented by simulation, distributions of step size and dwell time could be obtained that were found to be highly similar to those observed in the measurement. This provides an additional confirmation that

Figure 4.36 ***(facing page)*** **| Simulation of steps with 4 nm increment**
(A) The input for the simulation is presented with steps of 4 nm in increment, each occurring with a probability that corresponds to the observed probability of the step size distribution as determined from the measurement. **(B)** An exponential dwell time distribution was used as the input for the simulation. **(C)** The resulting step size distribution of the simulated noisy trace was fitted by a Gaussian mixture model, whose components (dashed lines, forward components: mean ± SD) represent the optimal composition of the distribution. **(D)** The resulting dwell time distribution of the simulated noisy trace. **(E)** Dwell time distribution of the simulated noisy trace with maximum likelihood estimation fit of three possible models to describe the data. The orange curve represents a convolution of two exponentials with different rate constants, the cyan curve represents a convolution of two exponentials with equal rate constants, and the purple curve represents a single exponential model. The fitting parameters and Akaike weights are indicated in the legend. **(F)** Left censoring of the simulated dwell time distribution.

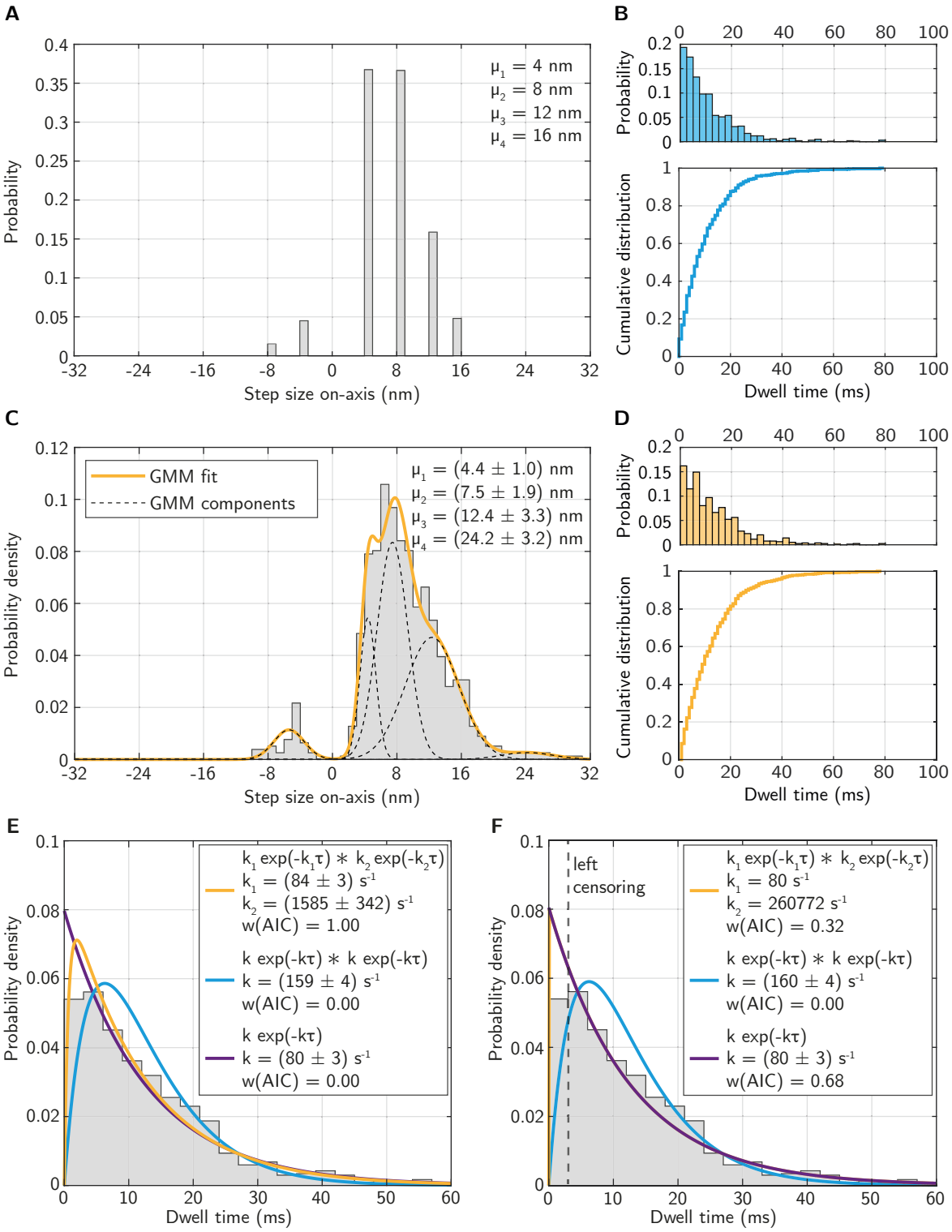
A
Probability
Step size on-axis (nm)
μ1 = 4 nm
μ2 = 8 nm
μ3 = 12 nm
μ4 = 16 nm
B
Probability
Cumulative distribution
Dwell time (ms)
C
Probability density
Step size on-axis (nm)
GMM fit
GMM components
μ1 = (4.4 ± 1.0) nm
μ2 = (7.5 ± 1.9) nm
μ3 = (12.4 ± 3.3) nm
μ4 = (24.2 ± 3.2) nm
D
Probability
Cumulative distribution
Dwell time (ms)
E
Probability density
Dwell time (ms)
k1 exp(-k1τ) ∗ k2 exp(-k2τ)
k1 = (84 ± 3) s-1
k2 = (1585 ± 342) s-1
w(AIC) = 1.00
k exp(-kτ) ∗ k exp(-kτ)
k = (159 ± 4) s-1
w(AIC) = 0.00
k exp(-kτ)
k = (80 ± 3) s-1
w(AIC) = 0.00
F
left
censoring
Probability density
Dwell time (ms)
k1 exp(-k1τ) ∗ k2 exp(-k2τ)
k1 = 80 s-1
k2 = 260772 s-1
w(AIC) = 0.32
k exp(-kτ) ∗ k exp(-kτ)
k = (160 ± 4) s-1
w(AIC) = 0.00
k exp(-kτ)
k = (80 ± 3) s-1
w(AIC) = 0.68

the dynein tail might perform steps of 4 nm increment, thus matching the microtubule lattice structure.

5 Discussion

Establishing Endogenous Dynein Tagging for Live-Cell Tracking

In order to establish the CRISPR/Cas9-mediated endogenous tagging of dynein in living neurons for MINFLUX tracking experiments, the entire sample preparation procedure was established and optimized. First, optimal conditions for the introduction of the different generated plasmids (Table 3.1) into the neurons via electroporation were determined. The optimal conditions were three pulses of 10 ms duration at 1400 V and 200 ng plasmid. Of the various protein tags tested, GFP and HaloTag were found to be the most effective, resulting in the observation of bidirectional axonal transport. The use of CRISPR/Cas9-mediated tagging was found to be advantageous over overexpression, as potential overexpression artifacts (Ratz et al., 2015) and potential alterations of motor complex integrity and endomembrane localization (King et al., 2003; Vaughan et al., 2001) were avoided. Among the different fluorophores tested (Table 4.1), the optimal labeling of tagged dynein was obtained by using the JFX650 HaloTag ligand for subsequent MINFLUX tracking, MaP555-Halo to identify CRISPR/Cas9-positive neurons, and BioTracker 488 Green Microtubule as a microtubule staining control. In contrast to PC12 cells, neurons were found to facilitate the tracking of individual molecules more effectively due to their axons containing unidirectionally oriented microtubules, which are necessary to determine movement direction, and a sparse distribution of dynein motors due to the thin and elongated shape of the axon.

In conclusion, the CRISPR/Cas9-mediated tagging of dynein in primary living hippocampal neurons has been successfully established, and can be used for single-molecule tracking of endogenous dynein using widefield microscopy and for MINFLUX tracking to resolve individual steps of endogenous dynein at its unimpeded speed under physiological ATP concentration.

Confirming Endogenous Dynein Tagging by Widefield Microscopy

The use of CRISPR/Cas9-mediated knock-in of a HaloTag7 sequence to two dynein loci enabled the tracking of individual labeled dynein subunits in primary neurons using the custom-built widefield microscope. This approach allows for the unimpeded direct study of the motor complex at physiological ATP concentrations. The tracking of both the DIC and DHC revealed bidirectional movement, including pauses and direction reversals, similar to what has been observed previously for intracellular cargo (Kural et al., 2005; Maday et al., 2012; Morris and Hollenbeck, 1993; Soppina et al., 2009; van Spronsen et al., 2013) or GFP-tagged DIC (Kobayashi and Murayama, 2009). It can be inferred that retrograde movement

is the result of active dynein-driven transport, while anterograde movement is most likely the result of dynein transported as a passenger of kinesin motors, both of which are bound to the same cargo (Hancock, 2014; Maday et al., 2014; Welte, 2004). The speeds in both directions were similar, with the DIC being slightly faster than the DHC, but both comparable to what has been observed previously for various cargoes transported in axons (Encalada et al., 2011; Fellows et al., 2024; Fu and Holzbaur, 2013). The limitations to widefield tracking of individual dynein motors were primarily due to the presence of labeled non-processive labeled motors, as well as photobleaching and out-of-focus movement. Overall, the strategy of tagging dynein endogenously by CRISPR/Cas9 is a suitable approach for studying the unimpeded dynein motor complex in living primary neurons, which was successfully visualized by the custom-built microscope.

Revealing Endogenous Dynein Steps in Live Neurons by MINFLUX Tracking

For the first time, individual nanometer-sized steps of endogenous, and thus unrestrained, mammalian dynein have been directly detected in live neurons through the use of MINFLUX tracking. Previously, the reduction of the ATP concentration by several orders of magnitude had markedly slowed down dynein, thereby facilitating the resolution of individual steps *in vitro* by widefield microscopy (DeWitt et al., 2012; Elshenawy et al., 2019; Niekamp et al., 2021; Qiu et al., 2012; Reck-Peterson et al., 2006). Alternatively, in live cells, large optical probes with a diameter exceeding 50 nm have been used to resolve steps of cargo transported by dynein (Nan et al., 2005; Peng et al., 2024).

The dynein tail (Halo-DHC, center of mass) was observed to move in discrete steps of a size between 4 and 16 nm along the on-axis of microtubules, exhibiting a prominent peak at 8 nm. These steps occur rapidly, with approximately half of the steps occurring in less than 7.4 ms. Previous *in vitro* measurements of purified dynein motor complexes without load have reported an on-axis step size distribution that is wider (8 nm to 32 nm) (Elshenawy et al., 2019; Mallik et al., 2004). However, when a high load was applied, the *in vitro* on-axis step size distributions (Elshenawy et al., 2019; Toba et al., 2006) appeared to be similar to those obtained in this work in live neurons, which seems reasonable given that dynein is only activated when bound to a cargo (load) in live cells. Furthermore, the measured mean forward step size of (8.7 ± 3.8) nm is comparable to the approximately 10 nm observed *in vitro* in the high load case (Elshenawy et al., 2019). This may indicate that dynein moves forward with a high force in live neurons, assuming a molecular gear mechanism that predicts a smaller step size under high load (Mallik et al., 2004). In contrast to *in vitro* measurements, additional factors may also contribute to the observed small forward step sizes, which were not present in the in vitro studies. These factors may include post-translational modifications (Guedes-Dias and Holzbaur, 2019) and microtubule-associated or adaptor proteins (Canty et al., 2023; Dixit et al., 2008; Ferro et al., 2022). Notwithstanding the aforementioned similarities, notable discrepancies were observed with regard to the occurrence of backward steps. *In vitro* studies

have revealed that the occurrence of backward steps is markedly higher in the absence of load (∼0.20) (DeWitt et al., 2012; Elshenawy et al., 2019; Reck-Peterson et al., 2006; Slivka et al., 2024), and even more so under high load (0.35 to 0.50) (Elshenawy et al., 2019). This stands in stark contrast to the observed occurrence of backward steps for Halo-DHC, which was found to be only 0.04. This finding suggests that dynein exhibits a high degree of efficiency in moving forward in live neurons, a condition that is undoubtedly distinct from that observed in a reduced *in vitro* environment.

An analysis of the off-axis steps of dynein, perpendicular to the on-axis, revealed that dynein frequently steps sideways, a finding that is consistent with those of previous studies (Elshenawy et al., 2019; Reck-Peterson et al., 2006; Slivka et al., 2024). This may be a consequence of the long stalk domain and flexibility of dynein, which allows for variable steps in both directions and may be necessary to circumvent obstacles in the crowded cellular environment (Ferro et al., 2019). Rarely, large sideways steps exceeding the diameter of a microtubule of 25 nm have been observed, which may indicate a step over many protofilaments or even a switch to a neighboring microtubule.

In contrast to the dynein tail (Halo-DHC), MINFLUX tracking of Halo-DIC revealed that both the on-axis and off-axis step size distributions are wider, with a higher incidence of backward and sideways steps and slightly larger on-axis steps. This may indicate that the N-terminus of the intermediate chain is more flexible in its movement, a finding that can be inferred from structural studies (Chaaban and Carter, 2022; Urnavicius et al., 2018).

In conclusion, MINFLUX permitted the direct tracking and detection of individual steps of endogenous dynein in living primary neurons at a spatiotemporal precision that was previously unattainable with established methods and a single small fluorophore. Consequently, the stepping behavior of dynein could be studied in its natural environment, confirming previous findings from *in vitro* measurements but also demonstrating discrepancies. Through MINFLUX, endogenous protein dynamics can be described directly and minimally invasively, not only *in vitro* but also inside cells, which represents a significant step towards the understanding of natural protein dynamics.

Discovering Rapid Direction Reversals Different from a Tug-of-War

MINFLUX tracking of endogenous dynein along the axon not only revealed the individual steps of dynein but also demonstrated bidirectional movement, in both retrograde and anterograde directions. As anticipated, this suggests that both dynein and kinesin motors are anchored to the same transported cargo, indicating that dynein may be a potential driver of retrograde movement and that kinesin may be responsible for driving anterograde movement. The presence of motors of both polarities acting on the cargo may facilitate navigation around obstacles and serve as a regulatory layer to reach the desired cargo destination (Hancock, 2014; Welte, 2004; Yildiz and Zhao, 2023). It is noteworthy, however, that nearly half of the recorded MINFLUX traces exhibited high processivity in a single direction and were

not bidirectional. This observation suggests that the various MINFLUX traces may have captured dynein attached to different types of cargo, given that the tracking procedure did not differentiate between cargo types. Furthermore, the high degree of processivity is underscored by the observation that processive retrograde and anterograde movement was most probable in the stationary long-term probability vector that originated from the constructed Markov chains.

By dividing the measured MINFLUX traces into segments of processive retrograde and anterograde movement, it was possible to observe pauses within these processive segments, as well as direction reversals from one movement direction to the other with an unprecedented level of detail. It is notable that direction reversals exhibited a significantly shorter duration than pauses, with an approximately ten times shorter duration, while the probability of their persistence was four times lower. This indicates that direction reversals appear to be a regulated process (Encalada et al., 2011; Fu and Holzbaur, 2013; Heber et al., 2024; Kunwar et al., 2011), which may be influenced by the involvement of adaptor or microtubule-associated proteins (Canty et al., 2023; Dixit et al., 2008; Ferro et al., 2022), or by post-translational modifications (Guedes-Dias and Holzbaur, 2019), in contrast to an unregulated and purely stochastic tug-of-war (Müller et al., 2008).

The duration of both pauses and reversals observed by MINFLUX tracking was markedly shorter than that previously observed in live cells using widefield microscopy (Fellows et al., 2024; Tirumala et al., 2024). This may be attributed to the fact that conventional methods did not permit the observation of individual steps in live cells using single fluorophores or fluorescent proteins, due to their limited spatiotemporal precision. It is conceivable that comparable rapid pauses or reversals, occurring in the order of several milliseconds as observed with MINFLUX tracking, may have been undetected in centroid tracking studies. Conversely, although some MINFLUX traces had a duration of several seconds and often ended in a stationary state, potential pauses or reversals on the order of seconds have not been observed with MINFLUX tracking, most likely due to photobleaching. Nevertheless, the single-step precision of MINFLUX has enabled the characterization of previously undetected reversals and pauses, suggesting the existence of a rapid regulatory reversal mechanism associated with bidirectional axonal transport in neurons.

Suggesting Incremental Dynein Step Sizes Matching the Microtubule Lattice

Given that dynein is a microtubule-based molecular motor and microtubules are highly periodic in their structure, it seems reasonable to posit that dynein performs steps that align with the periodicity of microtubules. As the MTBD of dynein binds between αβ-tubulin dimers with a length of 8 nm, assuming a stepping model where the dynein tail performs steps half the size of the MTBD and given that, in this work, Halo-DHC—that is to say, the dynein tail—has been tracked, the expected incremental step size of the dynein tail would be 4 nm. Although the spatiotemporal precision of the MINFLUX measurements may not have been

sufficient to resolve distinct peaks of 4 nm increment within the on-axis step size histogram, a Gaussian mixture model fit indicated the anticipated, albeit blurred and thus overlapping peaks separated by 4 nm. A simulation of steps with 4 nm increment at the measurement precision furthermore yielded a distribution and corresponding 4 nm incremental fit that was similarly shaped to that of the measurement. It can thus be proposed that the dynein tail may indeed perform steps of 4 nm increment that align with the microtubule lattice. Indeed, a recent MINFLUX study has demonstrated that the MTBD of truncated artificially linked yeast dynein monomers performs steps of 8 nm increment *in vitro* (Slivka et al., 2024). This serves to corroborate the hypothesis, although it should be noted that the yeast dynein in that study was almost ten times slower and obviously different from live-cell measurements of the endogenous mammalian dynein motor complex that was tracked in this work.

Determining the Single Rate-Limiting Process Underlying Dynein Kinetics

The tracking of endogenous dynein in live neurons using MINFLUX permitted not only the study of step sizes but also the determination of the kinetics underlying the stepping behavior. By considering all dwell times between successive steps, it was determined that the model comprising a convolution of two exponentials with a slow rate-limiting constant and a fast constant was the best fitting model. Alternatively, when extremely short dwell times were not considered, as they might have been missed and thus underrepresented, the single exponential model was the best fitting one. Both models include a single rate-limiting constant, which suggests that a single rate-limiting process underlies dynein kinetics. This can be interpreted by identifying the single rate-limiting process at a rate of $k = (90 \pm 3)\ \mathrm{s}^{-1}$ as the consumption of one ATP molecule per step, consistent with previous *in vitro* studies (DeWitt et al., 2015; Elshenawy et al., 2019; Mallik et al., 2004; Reck-Peterson et al., 2006; Slivka et al., 2024; Toba et al., 2006). It is, however, not possible to completely exclude the possibility that additional ATP molecules are hydrolyzed independently of the performance of a step.

The observation that dynein utilizes a single ATP molecule to perform a step is in accordance with the prevailing stepping mechanisms, which were derived from *in vitro* measurements. These include the "alternating shuffle" model (Reck-Peterson et al., 2006), which posits that the head domains alternately perform steps twice the size of the tail domain, the "inchworm model" (Niekamp et al., 2021), which suggests that one head domain always leads and the other follows, and an uncoordinated head movement (DeWitt et al., 2012; Qiu et al., 2012), which postulates that the head domains step independently.

This contrasts with a recently proposed model of successive consumption of two ATP molecules per step (Peng et al., 2024), which is not supported by the dwell time data and corresponding fits that originate from direct tracking of dynein in the present work. With regard to the latter model, it remains uncertain whether and how tracking the transported cargo can be extrapolated to dynein itself. Although the size of the introduced HaloTag, used in this work for binding the tracked fluorophore, can be considered small in comparison

to the size of the dynein motor complex, it cannot be completely excluded that this small alteration causes minor interference. However, these concerns are addressed by the fact that the CRISPR/Cas9-tagged dynein exhibits movement patterns similar to those observed in other live-cell studies (Encalada et al., 2011; Kural et al., 2005; Maday et al., 2012; Morris and Hollenbeck, 1993; Soppina et al., 2009; van Spronsen et al., 2013) and that the tagging position of the dynein tail is a common tagging position utilized in other studies (Elshenawy et al., 2019, 2020; Schlager et al., 2014). Moreover, tracking dynein with HaloTags on different positions on the motor complex (Halo-DHC and Halo-DIC) yielded comparable dwell time distributions and led to the same conclusions regarding the fitting procedure. It is therefore unlikely that the introduction of a comparatively small HaloTag would cause interference.

In light of these observations, it can be concluded that endogenous dynein requires one ATP molecule to perform a single step, a finding that provides clarification on the debate concerning the number of ATP molecules consumed per step.

6 Outlook

In addition to the MINFLUX tracking of the two dynein subunits (Halo-DHC and Halo-DIC) and the detection of their stepping behavior, rapid direction reversals and underlying single rate-limiting kinetics, further tagging positions and labeling strategies may be worthy of consideration for the purposes of clarifying the stepping mechanism of dynein in live cells. The CRISPR/Cas9 knock-in plasmid pO-Dync1h1-Halo, which has been generated in this work, might be used to tag and track the dynein head domain. By comparing the stepping behavior of the head domain to that of the dynein tail, it may be possible to clarify the underlying stepping mechanism of mammalian dynein in live cells. The hypothesis of uncoordinated independent head movement (DeWitt et al., 2012; Qiu et al., 2012) would be substantiated if the dynein head were to perform steps twice as large as those of the tail, while its dwell time distribution was also best described by a single exponential, albeit at a rate half as large as that of the tail, given that the tail performs a step with each head step. In contrast, the inchworm (Niekamp et al., 2021) or alternating shuffle model (Reck-Peterson et al., 2006) would be confirmed if the dwell time distribution of the head was best described by a convolution of two exponentials with equal rates, while the step size of the head was also twice as large as that of the tail. The latter two models can be differentiated most elegantly by performing two-color MINFLUX tracking, as was done for kinesin *in vitro* (Scheiderer et al., 2024). Two-color tracking in live cells would necessitate the implementation of an orthogonal labeling strategy, such as the use of a SNAP-tag in conjunction with the HaloTag.

The tagging of the MTBD of dynein, as has been done *in vitro* on truncated artificially linked dynein monomers (Slivka et al., 2024), would require, for example, the use of highly laborious genetic code expansion (Arsić et al., 2022; Mihaila et al., 2022) for the mammalian motor complex in live cells. This is due to the fact that the MTBD is relatively small in comparison to a self-labeling tag such as the HaloTag. One potential insertion site could be analogous to that employed for yeast, as demonstrated in previous studies (Niekamp et al., 2021; Slivka et al., 2024), given the similarity in amino acid sequence and structure between the yeast MTBD (Nishida et al., 2020) and those of rat or human (Zhang et al., 2017).

In order to evaluate the hypothesis that dynein would consume two ATP molecules to perform a step, a hypothesis that was proposed by analyzing the dwell times between steps of the transported cargo (Peng et al., 2024), it might be possible to tag and track dynactin using MINFLUX. An analysis of step sizes and dwell times would provide clarity on the underlying stepping behavior of the motor complex.

To ascertain whether disparate types of cargo may result in variations in stepping behav-

ior, the MINFLUX tracking procedure could be adapted. To this end, the tracking procedure could be modified to select whether the tracked dynein is transporting a specific type of cargo. This could be achieved by labeling one specific type of cargo, such as lysosomes, endosomes, or mitochondria, with a fluorophore that can be excited with the 561 nm laser. The prescan could then be conducted with the 561 nm laser to localize the labeled transported cargo, and then switching to the 640 nm laser in the subsequent iterations to perform the MINFLUX tracking on the labeled dynein that transports the labeled cargo.

The analysis of the on-axis step size distribution using a Gaussian mixture model led to the hypothesis that the dynein tail (Halo-DHC) performs steps of an increment of 4 nm, which would then align with the microtubule lattice structure. However, due to the limited localization precision, potential peaks separated by 4 nm may appear blurred and overlap. To enhance the localization precision, it may be feasible to reduce the TCP diameter L to resolve the peaks separated by 4 nm.

Given that dynein has been observed to helically move around the microtubule *in vitro* (Elshenawy et al., 2019), it may be feasible to utilize a three dimensional donut excitation beam in conjunction with a modified TCP comprising additional probing positions in the z direction (Gwosch et al., 2020; Schmidt et al., 2021) to ascertain whether a comparable helical movement is also discernible in live cells. Some two-dimensional MINFLUX traces exhibited motion that resembled a sinuous line, which may correspond to a helical motion in three dimensions.

In this work, MINFLUX traces have been acquired in the mid axon. It is plausible that there are regional variations in dynein motility within the axon. As an example of motility differing depending on the axonal region, it has been demonstrated that autophagosomes, which are retrogradely driven by dynein, initially move bidirectionally in the distal region but then switch to a unidirectional processive motility (Maday et al., 2012). Dynein tracking in distinct axonal regions may yield disparate motility patterns, including the potential for a higher incidence of direction reversals in the axon initial segment.

In conclusion, MINFLUX tracking of the endogenously tagged dynein established in this work allowed, for the first time, the direct detection of individual nanometer-sized dynein steps in live neurons. This enabled the characterization of dynein's stepping behavior, and revealed previously unseen rapid directional reversals that had remained hidden by the lack of spatiotemporal precision of conventional methods. The rapid reversals indicate the presence of a regulated reversal mechanism for opposing motors, which is distinct from an unregulated stochastic tug-of-war. Furthermore, direct tracking of dynein revealed its underlying kinetics to be single-rate limited, indicating the consumption of a single ATP molecule per step. The methods and results established in this work have the potential to stimulate further insights into fast protein dynamics in their natural cellular environment and to elucidate the molecular aspects of various diseases, through the superior spatiotemporal precision of MINFLUX.

A Appendix

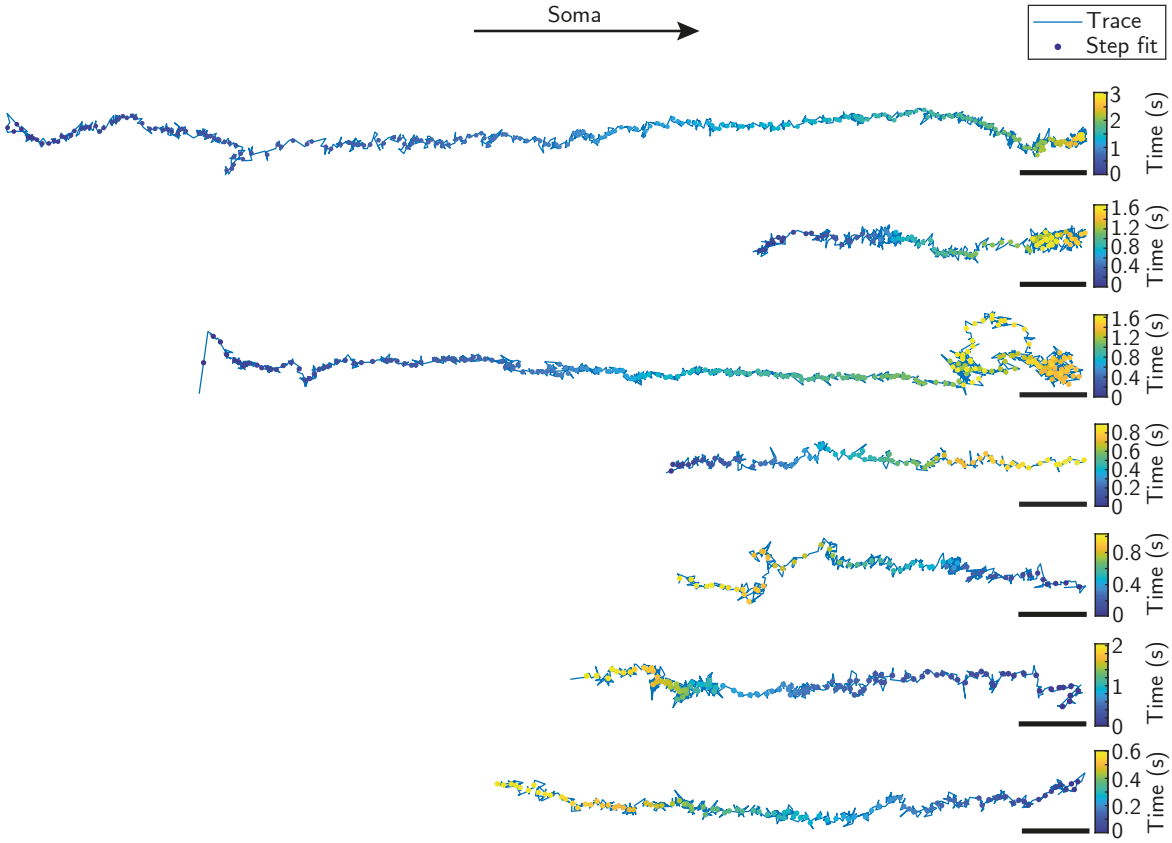

Figure A.1 | Additional MINFLUX traces of endogenous dynein
The MINFLUX traces displayed here were acquired with both Halo-DHC and Halo-DIC motors in living neurons. They contain portions of the trace and corresponding steps that were filtered out as direction reversals or pauses in the subsequent segmentation analysis. This is due to the fact that the step-finding algorithm utilized fits steps to the entire trace, including direction reversals or pauses. Scale bars: 100 nm.

Bibliography

Shabeen Ally, Adam G. Larson, Kari Barlan, Sarah E. Rice, and Vladimir I. Gelfand. Opposite-polarity motors activate one another to trigger cargo transport in live cells. *Journal of Cell Biology*, 187:1071–1082, 2009. doi: 10.1083/jcb.200908075.

Gregory M. Alushin, Gabriel C. Lander, Elizabeth H. Kellogg, Rui Zhang, David Baker, and Eva Nogales. High-Resolution Microtubule Structures Reveal the Structural Transitions in αβ-Tubulin upon GTP Hydrolysis. *Cell*, 157:1117–1129, 2014. doi: 10.1016/j.cell.2014.03.053.

Jun Ando, Tomohiro Shima, Riko Kanazawa, Rieko Shimo-Kon, Akihiko Nakamura, Mayuko Yamamoto, Takahide Kon, and Ryota Iino. Small stepping motion of processive dynein revealed by load-free high-speed single-particle tracking. *Scientific Reports*, 10:1080, 2020. doi: 10.1038/s41598-020-58070-y.

Aleksandra Arsić, Cathleen Hagemann, Nevena Stajković, Timm Schubert, and Ivana Nikić-Spiegel. Minimal genetically encoded tags for fluorescent protein labeling in living neurons. *Nature Communications*, 13:314, 2022. doi: 10.1038/s41467-022-27956-y.

Charles L. Asbury, Adrian N. Fehr, and Steven M. Block. Kinesin Moves by an Asymmetric Hand-Over-Hand Mechanism. *Science*, 302:2130–2134, 2003. doi: 10.1126/science.1092985.

Ana B. Asenjo, Chandrima Chatterjee, Dongyan Tan, Vania DePaoli, William J. Rice, Ruben Diaz-Avalos, Mariena Silvestry, and Hernando Sosa. Structural Model for Tubulin Recognition and Deformation by Kinesin-13 Microtubule Depolymerases. *Cell Reports*, 3:759–768, 2013. doi: 10.1016/j.celrep.2013.01.030.

P W Baas, J S Deitch, M M Black, and G A Banker. Polarity orientation of microtubules in hippocampal neurons: uniformity in the axon and nonuniformity in the dendrite. *Proceedings of the National Academy of Sciences*, 85:8335–8339, 1988. doi: 10.1073/pnas.85.21.8335.

Francisco Balzarotti, Yvan Eilers, Klaus C. Gwosch, Arvid H. Gynnå, Volker Westphal, Fernando D. Stefani, Johan Elf, and Stefan W. Hell. Nanometer resolution imaging and tracking of fluorescent molecules with minimal photon fluxes. *Science (New York, N.Y.)*, 355:606–612, 2017. doi: 10.1126/science.aak9913.

Eric Betzig, George H. Patterson, Rachid Sougrat, O. Wolf Lindwasser, Scott Olenych, Juan S. Bonifacino, Michael W. Davidson, Jennifer Lippincott-Schwartz, and Harald F. Hess. Imaging Intracellular Fluorescent Proteins at Nanometer Resolution. *Science (New York, N.Y.)*, 313:1642–1645, 2006. doi: 10.1126/science.1127344.

Gira Bhabha, Hui-Chun Cheng, Nan Zhang, Arne Moeller, Maofu Liao, Jeffrey A. Speir, Yifan Cheng, and Ronald D. Vale. Allosteric Communication in the Dynein Motor Domain. *Cell*, 159:857–868, 2014. doi: 10.1016/j.cell.2014.10.018.

Steven L. Brunton and J. Nathan Kutz. *Data-Driven Science and Engineering*. Cambridge University Press, 2019. doi: 10.1017/9781108380690.

Janis K. Burkhardt, Christophe J. Echeverri, Tommy Nilsson, and Richard B. Vallee. Overexpression of the Dynamitin (p50) Subunit of the Dynactin Complex Disrupts Dynein-dependent Maintenance of Membrane Organelle Distribution. *Journal of Cell Biology*, 139: 469–484, 1997. doi: 10.1083/JCB.139.2.469.

Kenneth P. Burnham and David R. Anderson, editors. *Model Selection and Multimodel Inference*. Springer New York, 2nd, 2002. doi: 10.1007/b97636.

Alexey N. Butkevich, Gyuzel Yu Mitronova, Sven C. Sidenstein, Jessica L. Klocke, Dirk Kamin, Dirk N.H. Meineke, Elisa D'Este, Philip Tobias Kraemer, Johann G. Danzl, Vladimir N. Belov, and Stefan W. Hell. Fluorescent Rhodamines and Fluorogenic Carbopyronines for Super-Resolution STED Microscopy in Living Cells. *Angewandte Chemie International Edition*, 55:3290–3294, 2016. doi: 10.1002/ANIE.201511018.

Alexey N. Butkevich, Haisen Ta, Michael Ratz, Stefan Stoldt, Stefan Jakobs, Vladimir N. Belov, and Stefan W. Hell. Two-Color 810 nm STED Nanoscopy of Living Cells with Endogenous SNAP-Tagged Fusion Proteins. *ACS Chemical Biology*, 13:475–480, 2018. doi: 10.1021/acschembio.7b00616.

John T. Canty, Ruensern Tan, Emre Kusakci, Jonathan Fernandes, and Ahmet Yildiz. Structure and Mechanics of Dynein Motors. *Annual Review of Biophysics*, 50:549–574, 2021. doi: 10.1146/annurev-biophys-111020-101511.

John T. Canty, Andrew Hensley, Merve Aslan, Amanda Jack, and Ahmet Yildiz. TRAK adaptors regulate the recruitment and activation of dynein and kinesin in mitochondrial transport. *Nature Communications*, 14:1376, 2023. doi: 10.1038/s41467-023-36945-8.

Andrew P. Carter, Joan E. Garbarino, Elizabeth M. Wilson-Kubalek, Wesley E. Shipley, Carol Cho, Ronald A. Milligan, Ronald D. Vale, and I. R. Gibbons. Structure and Functional Role of Dynein's Microtubule-Binding Domain. *Science*, 322:1691–1695, 2008. doi: 10.1126/science.1164424.

Sydney E. Cason, Adam R. Fenton, and Erika L. F. Holzbaur. *Employing Live-Cell Imaging to Study Motor-Mediated Transport*, pages 45–59. Humana, New York, NY, 2023. doi: 10.1007/978-1-0716-2958-1_3.

Sami Chaaban and Andrew P. Carter. Structure of dynein–dynactin on microtubules shows tandem adaptor binding. *Nature 2022*, pages 1–5, 2022. doi: 10.1038/s41586-022-05186-y.

Brendan P. Cormack, Raphael H. Valdivia, and Stanley Falkow. FACS-optimized mutants of the green fluorescent protein (GFP). *Gene*, 173:33–38, 1996. doi: 10.1016/0378-1119(95)00685-0.

Georgeta Crivat and Justin W. Taraska. Imaging proteins inside cells with fluorescent tags. *Trends in Biotechnology*, 30:8–16, 2012. doi: 10.1016/j.tibtech.2011.08.002.

Takahiro Deguchi, Malina K. Iwanski, Eva-Maria Schentarra, Christopher Heidebrecht, Lisa Schmidt, Jennifer Heck, Tobias Weihs, Sebastian Schnorrenberg, Philipp Hoess, Sheng Liu, Veronika Chevyreva, Kyung-Min Noh, Lukas C. Kapitein, and Jonas Ries. Direct observation of motor protein stepping in living cells using MINFLUX. *Science*, 379:1010–1015, 2023. doi: 10.1126/science.ade2676.

Katrin Deinhardt, Sara Salinas, Carole Verastegui, Rose Watson, Daniel Worth, Sarah Hanrahan, Cecilia Bucci, and Giampietro Schiavo. Rab5 and Rab7 Control Endocytic Sorting along the Axonal Retrograde Transport Pathway. *Neuron*, 52:293–305, 2006. doi: 10.1016/j.neuron.2006.08.018.

Victoria E. Deneke, Alberto Puliafito, Daniel Krueger, Avaneesh V. Narla, Alessandro De Simone, Luca Primo, Massimo Vergassola, Stefano De Renzis, and Stefano Di Talia. Self-Organized Nuclear Positioning Synchronizes the Cell Cycle in Drosophila Embryos. *Cell*, 177:925–941.e17, 2019. doi: 10.1016/J.CELL.2019.03.007.

Mark A. DeWitt, Amy Y. Chang, Peter A. Combs, and Ahmet Yildiz. Cytoplasmic dynein moves through uncoordinated stepping of the AAA+ ring domains. *Science*, 335:221–225, 2012. doi: 10.1126/SCIENCE.1215804.

Mark A DeWitt, Caroline A Cypranowska, Frank B Cleary, Vladislav Belyy, and Ahmet Yildiz. The AAA3 domain of cytoplasmic dynein acts as a switch to facilitate microtubule release. *Nature Structural and Molecular Biology*, 22:73–80, 2015. doi: 10.1038/nsmb.2930.

James A. Dix and A.S. Verkman. Crowding Effects on Diffusion in Solutions and Cells. *Annual Review of Biophysics*, 37:247–263, 2008. doi: 10.1146/annurev.biophys.37.032807.125824.

Ram Dixit, Jennifer L. Ross, Yale E. Goldman, and Erika L. F. Holzbaur. Differential Regulation of Dynein and Kinesin Motor Proteins by Tau. *Science*, 319:1086–1089, 2008. doi: 10.1126/science.1152993.

John G Doench, Nicolo Fusi, Meagan Sullender, Mudra Hegde, Emma W Vaimberg, Katherine F Donovan, Ian Smith, Zuzana Tothova, Craig Wilen, Robert Orchard, Herbert W Virgin, Jennifer Listgarten, and David E Root. Optimized sgRNA design to maximize activity and minimize off-target effects of CRISPR-Cas9. *Nature Biotechnology*, 34:184–191, 2016. doi: 10.1038/nbt.3437.

Jennifer A. Doudna and Emmanuelle Charpentier. The new frontier of genome engineering with CRISPR-Cas9. *Science*, 346, 2014. doi: 10.1126/science.1258096.

Yvan Eilers, Haisen Ta, Klaus C. Gwosch, Francisco Balzarotti, and Stefan W. Hell. MINFLUX monitors rapid molecular jumps with superior spatiotemporal resolution. *Proceedings of the National Academy of Sciences*, 115:6117–6122, 2018. doi: 10.1073/pnas.1801672115.

Mohamed M. Elshenawy, John T. Canty, Liya Oster, Luke S. Ferro, Zhou Zhou, Scott C. Blanchard, and Ahmet Yildiz. Cargo adaptors regulate stepping and force generation of mammalian dynein–dynactin. *Nature Chemical Biology*, 15:1093–1101, 2019. doi: 10.1038/s41589-019-0352-0.

Mohamed M. Elshenawy, Emre Kusakci, Sara Volz, Janina Baumbach, Simon L. Bullock, and Ahmet Yildiz. Lis1 activates dynein motility by modulating its pairing with dynactin. *Nature Cell Biology*, 22:570–578, 2020. doi: 10.1038/s41556-020-0501-4.

Sandra E. Encalada, Lukasz Szpankowski, Chun hong Xia, and Lawrence S.B. Goldstein. Stable Kinesin and Dynein Assemblies Drive the Axonal Transport of Mammalian Prion Protein Vesicles. *Cell*, 144:551–565, 2011. doi: 10.1016/j.cell.2011.01.021.

Lance P Encell, Rachel Friedman Ohana, Kris Zimmerman, Paul Otto, Gediminas Vidugiris, Monika G Wood, Georgyi V Los, Mark G McDougall, Chad Zimprich, Natasha Karassina, Randall D Learish, Robin Hurst, James Hartnett, Sarah Wheeler, Pete Stecha, Jami English, Kate Zhao, Jacqui Mendez, Hélène A Benink, Nancy Murphy, Danette L Daniels, Michael R Slater, Marjeta Urh, Aldis Darzins, Dieter H Klaubert, Robert F Bulleit, and Keith V Wood. Development of a Dehalogenase-Based Protein Fusion Tag Capable of Rapid, Selective and Covalent Attachment to Customizable Ligands. *Current Chemical Genomics and Translational Medicine*, 6:55–71, 2012. doi: 10.2174/1875397301206010055.

Alexander D. Fellows, Michaela Bruntraeger, Thomas Burgold, Andrew R. Bassett, and Andrew P. Carter. Dynein and dynactin move long-range but are delivered separately to the axon tip. *Journal of Cell Biology*, 223:2023.07.03.547521, 2024. doi: 10.1083/jcb.202309084.

Adam R. Fenton, Thomas A. Jongens, and Erika L. F. Holzbaur. Mitochondrial adaptor TRAK2 activates and functionally links opposing kinesin and dynein motors. *Nature Communications*, 12:4578, 2021. doi: 10.1038/s41467-021-24862-7.

Luke S Ferro, Sinan Can, Meghan A Turner, Mohamed M ElShenawy, and Ahmet Yildiz. Kinesin and dynein use distinct mechanisms to bypass obstacles. *eLife*, 8, 2019. doi: 10.7554/eLife.48629.

Luke S. Ferro, Qianglin Fang, Lisa Eshun-Wilson, Jonathan Fernandes, Amanda Jack, Daniel P. Farrell, Mert Golcuk, Teun Huijben, Katelyn Costa, Mert Gur, Frank DiMaio, Eva Nogales, and Ahmet Yildiz. Structural and functional insight into regulation of kinesin-1 by microtubule-associated protein MAP7. *Science*, 375:326–331, 2022. doi: 10.1126/science.abf6154.

Meng Fu and Erika L.F. Holzbaur. JIP1 regulates the directionality of APP axonal transport by coordinating kinesin and dynein motors. *Journal of Cell Biology*, 202:495–508, 2013. doi: 10.1083/jcb.201302078.

Toby J Gibson, Markus Seiler, and Reiner A Veitia. The transience of transient overexpression. *Nature Methods*, 10:715–721, 2013. doi: 10.1038/nmeth.2534.

Jonathan B. Grimm, Liangqi Xie, Jason C. Casler, Ronak Patel, Ariana N. Tkachuk, Natalie Falco, Heejun Choi, Jennifer Lippincott-Schwartz, Timothy A. Brown, Benjamin S. Glick, Zhe Liu, and Luke D. Lavis. A General Method to Improve Fluorophores Using Deuterated Auxochromes. *JACS Au*, 1:690–696, 2021. doi: 10.1021/jacsau.1c00006.

Danielle A. Grotjahn, Saikat Chowdhury, Yiru Xu, Richard J. McKenney, Trina A. Schroer, and Gabriel C. Lander. Cryo-electron tomography reveals that dynactin recruits a team of dyneins for processive motility. *Nature Structural and Molecular Biology*, 25:203–207, 2018. doi: 10.1038/s41594-018-0027-7.

Pedro Guedes-Dias and Erika L. F. Holzbaur. Axonal transport: Driving synaptic function. *Science*, 366, 2019. doi: 10.1126/science.aaw9997.

Xiaoli Guo, Ginny G. Farías, Rafael Mattera, and Juan S. Bonifacino. Rab5 and its effector FHF contribute to neuronal polarity through dynein-dependent retrieval of somatodendritic proteins from the axon. *Proceedings of the National Academy of Sciences*, 113:E5318–E5327, 2016. doi: 10.1073/pnas.1601844113.

Klaus C. Gwosch, Jasmin K. Pape, Francisco Balzarotti, Philipp Hoess, Jan Ellenberg, Jonas Ries, and Stefan W. Hell. MINFLUX nanoscopy delivers 3D multicolor nanometer resolution in cells. *Nature Methods*, 17:217–224, 2020. doi: 10.1038/s41592-019-0688-0.

Klaus C. Gwosch, Francisco Balzarotti, Jasmin K. Pape, Philipp Hoess, Jan Ellenberg, Jonas Ries, Ulf Matti, Roman Schmidt, Steffen J. Sahl, and Stefan W. Hell. Reply to: Assessment of 3D MINFLUX data for quantitative structural biology in cells. *Nature Methods*, 20:52–54, 2023. doi: 10.1038/s41592-022-01695-w.

Majid Hafezparast, Rainer Klocke, Christiana Ruhrberg, Andreas Marquardt, Azlina Ahmad-Annuar, Samantha Bowen, Giovanna Lalli, Abi S. Witherden, Holger Hummerich, Sharon Nicholson, P. Jeffrey Morgan, Ravi Oozageer, John V. Priestley, Sharon Averill, Von R. King, Simon Ball, Jo Peters, Takashi Toda, Ayumu Yamamoto, Yasushi Hiraoka, Martin Augustin, Dirk Korthaus, Sigrid Wattler, Philipp Wabnitz, Carmen Dickneite, Stefan Lampel, Florian Boehme, Gisela Peraus, Andreas Popp, Martina Rudelius, Juergen Schlegel, Helmut Fuchs, Martin Hrabe De Angelis, Giampietro Schiavo, David T. Shima, Andreas P. Russ, Gabriele Stumm, Joanne E. Martin, and Elizabeth M.C. Fisher. Mutations in dynein link motor neuron degeneration to defects in retrograde transport. *Science*, 300:808–812, 2003. doi: 10.1126/SCIENCE.1083129.

William O. Hancock. Bidirectional cargo transport: moving beyond tug of war. *Nature Reviews Molecular Cell Biology*, 15:615–628, 2014. doi: 10.1038/nrm3853.

Martin Harterink, Karin Vocking, Xingxiu Pan, Eva M. Soriano Jerez, Lotte Slenders, Amélie Fréal, Roderick P. Tas, Willine J. van de Wetering, Karina Timmer, Jasmijn Motshagen, Sam F.B. van Beuningen, Lukas C. Kapitein, Willie J.C. Geerts, Jan A. Post, and Casper C. Hoogenraad. TRIM46 Organizes Microtubule Fasciculation in the Axon Initial Segment. *The Journal of Neuroscience*, 39:4864–4873, 2019. doi: 10.1523/JNEUROSCI.3105-18.2019.

Simone Heber, Mark A. McClintock, Bernd Simon, Eve Mehtab, Karine Lapouge, Janosch Hennig, Simon L. Bullock, and Anne Ephrussi. Tropomyosin 1-I/C coordinates kinesin-1 and dynein motors during oskar mRNA transport. *Nature Structural and Molecular Biology*, 31:476–488, 2024. doi: 10.1038/s41594-024-01212-x.

Stefan W. Hell. Far-Field Optical Nanoscopy. *Science*, 316:1153–1158, 2007. doi: 10.1126/science.1137395.

Stefan W Hell. Microscopy and its focal switch. *Nature Methods*, 6:24–32, 2009. doi: 10.1038/nmeth.1291.

Stefan W. Hell. Nanoscopy with Focused Light (Nobel Lecture). *Angewandte Chemie International Edition*, 54:8054–8066, 2015. doi: 10.1002/anie.201504181.

Stefan W. Hell and Jan Wichmann. Breaking the diffraction resolution limit by stimulated emission: stimulated-emission-depletion fluorescence microscopy. *Optics Letters*, 19:780–782, 1994. doi: 10.1364/OL.19.000780.

Adam G. Hendricks, Eran Perlson, Jennifer L. Ross, Harry W. Schroeder, Mariko Tokito, and Erika L.F. Holzbaur. Motor Coordination via a Tug-of-War Mechanism Drives Bidirectional Vesicle Transport. *Current Biology*, 20:697–702, 2010. doi: 10.1016/j.cub.2010.02.058.

Samuel T. Hess, Thanu P.K. Girirajan, and Michael D. Mason. Ultra-High Resolution Imaging by Fluorescence Photoactivation Localization Microscopy. *Biophysical Journal*, 91:4258–4272, 2006. doi: 10.1529/BIOPHYSJ.106.091116.

Erika L. F. Holzbaur and Kenneth A. Johnson. Microtubules accelerate ADP release by dynein. *Biochemistry*, 28:7010–7016, 1989. doi: 10.1021/bi00443a034.

Joe Howard and Anthony A. Hyman. Dynamics and mechanics of the microtubule plus end. *Nature*, 422:753–758, 2003. doi: 10.1038/nature01600.

Patrick D Hsu, David A Scott, Joshua A Weinstein, F Ann Ran, Silvana Konermann, Vineeta Agarwala, Yinqing Li, Eli J Fine, Xuebing Wu, Ophir Shalem, Thomas J Cradick, Luciano A Marraffini, Gang Bao, and Feng Zhang. DNA targeting specificity of RNA-guided Cas9 nucleases. *Nature Biotechnology*, 31:827–832, 2013. doi: 10.1038/nbt.2647.

Wei Hua, Johnson Chung, and Jeff Gelles. Distinguishing Inchworm and Hand-Over-Hand Processive Kinesin Movement by Neck Rotation Measurements. *Science*, 295:844–848, 2002. doi: 10.1126/science.1063089.

Carsten Janke and Maria M. Magiera. The tubulin code and its role in controlling microtubule properties and functions. *Nature Reviews Molecular Cell Biology*, 21:307–326, 2020. doi: 10.1038/s41580-020-0214-3.

Martin Jinek, Krzysztof Chylinski, Ines Fonfara, Michael Hauer, Jennifer A. Doudna, and Emmanuelle Charpentier. A Programmable Dual-RNA–Guided DNA Endonuclease in Adaptive Bacterial Immunity. *Science*, 337:816–821, 2012. doi: 10.1126/science.1225829.

Agnieszka A. Kendrick, Andrea M. Dickey, William B. Redwine, Phuoc Tien Tran, Laura Pontano Vaites, Monika Dzieciatkowska, J. Wade Harper, and Samara L. Reck-Peterson. Hook3 is a scaffold for the opposite-polarity microtubule-based motors cytoplasmic dynein-1 and KIF1C. *Journal of Cell Biology*, 218:2982–3001, 2019. doi: 10.1083/jcb.201812170.

Antje Keppler, Susanne Gendreizig, Thomas Gronemeyer, Horst Pick, Horst Vogel, and Kai Johnsson. A general method for the covalent labeling of fusion proteins with small molecules in vivo. *Nature Biotechnology*, 21:86–89, 2003. doi: 10.1038/nbt765.

Stephen J. King, Christa L. Brown, Kerstin C. Maier, Nicholas J. Quintyne, and Trina A. Schroer. Analysis of the Dynein-Dynactin Interaction In Vitro and In Vivo. *Molecular Biology of the Cell*, 14:5089–5097, 2003. doi: 10.1091/mbc.e03-01-0025.

Thomas A. Klar, Stefan Jakobs, Marcus Dyba, Alexander Egner, and Stefan W. Hell. Fluorescence microscopy with diffraction resolution barrier broken by stimulated emission. *Proceedings of the National Academy of Sciences of the United States of America*, 97:8206–8210, 2000. doi: 10.1073/pnas.97.15.8206.

Eva Klinman and Erika L.F. Holzbaur. Comparative analysis of axonal transport markers in primary mammalian neurons. *Methods in Cell Biology*, 131:409–424, 2016. doi: 10.1016/bs.mcb.2015.06.011.

Gavin J. Knott and Jennifer A. Doudna. CRISPR-Cas guides the future of genetic engineering. *Science*, 361:866–869, 2018. doi: 10.1126/science.aat5011.

Takuya Kobayashi and Takashi Murayama. Cell Cycle-Dependent Microtubule-Based Dynamic Transport of Cytoplasmic Dynein in Mammalian Cells. *PLoS ONE*, 4:e7827, 2009. doi: 10.1371/journal.pone.0007827.

Takahide Kon, Masaya Nishiura, Reiko Ohkura, Yoko Y. Toyoshima, and Kazuo Sutoh. Distinct Functions of Nucleotide-Binding/Hydrolysis Sites in the Four AAA Modules of Cytoplasmic Dynein. *Biochemistry*, 43:11266–11274, 2004. doi: 10.1021/bi048985a.

Takahide Kon, Takuji Oyama, Rieko Shimo-Kon, Kenji Imamula, Tomohiro Shima, Kazuo Sutoh, and Genji Kurisu. The 2.8 Å crystal structure of the dynein motor domain. *Nature*, 484:345–350, 2012. doi: 10.1038/nature10955.

Elena F. Koslover, Caleb K. Chan, and Julie A. Theriot. Cytoplasmic Flow and Mixing Due to Deformation of Motile Cells. *Biophysical Journal*, 113:2077–2087, 2017. doi: 10.1016/J.BPJ.2017.09.009.

Ambarish Kunwar, Suvranta K. Tripathy, Jing Xu, Michelle K. Mattson, Preetha Anand, Roby Sigua, Michael Vershinin, Richard J. McKenney, Clare C. Yu, Alexander Mogilner, and Steven P. Gross. Mechanical stochastic tug-of-war models cannot explain bidirectional lipid-droplet transport. *Proceedings of the National Academy of Sciences*, 108:18960–18965, 2011. doi: 10.1073/pnas.1107841108.

Comert Kural, Hwajin Kim, Sheyum Syed, Gohta Goshima, Vladimir I. Gelfand, and Paul R. Selvin. Kinesin and Dynein Move a Peroxisome in Vivo: A Tug-of-War or Coordinated Movement? *Science*, 308:1469–1472, 2005. doi: 10.1126/science.1108408.

Joseph R Lakowicz. *Principles of Fluorescence Spectroscopy*. Springer US, 2006. doi: 10.1007/978-0-387-46312-4.

Nicolas Lardon, Lu Wang, Aline Tschanz, Philipp Hoess, Mai Tran, Elisa D'Este, Jonas Ries, and Kai Johnsson. Systematic Tuning of Rhodamine Spirocyclization for Super-resolution Microscopy. *Journal of the American Chemical Society*, 143:14592–14600, 2021. doi: 10.1021/jacs.1c05004.

Xinglei Liu, Lu Rao, and Arne Gennerich. The regulatory function of the AAA4 ATPase domain of cytoplasmic dynein. *Nature Communications*, 11:5952, 2020. doi: 10.1038/s41467-020-19477-3.

Luuk Loeff, Jacob W.J. Kerssemakers, Chirlmin Joo, and Cees Dekker. AutoStepfinder: A fast and automated step detection method for single-molecule analysis. *Patterns*, 2:100256, 2021. doi: 10.1016/J.PATTER.2021.100256.

Georgyi V. Los, Lance P. Encell, Mark G. McDougall, Danette D. Hartzell, Natasha Karassina, Chad Zimprich, Monika G. Wood, Randy Learish, Rachel Friedman Ohana, Marjeta Urh, Dan Simpson, Jacqui Mendez, Kris Zimmerman, Paul Otto, Gediminas Vidugiris, Ji Zhu, Aldis Darzins, Dieter H. Klaubert, Robert F. Bulleit, and Keith V. Wood. HaloTag: A Novel Protein Labeling Technology for Cell Imaging and Protein Analysis. *ACS Chemical Biology*, 3:373–382, 2008. doi: 10.1021/cb800025k.

Gražvydas Lukinavičius, Keitaro Umezawa, Nicolas Olivier, Alf Honigmann, Guoying Yang, Tilman Plass, Veronika Mueller, Luc Reymond, Ivan R. Corrêa Jr, Zhen-Ge Luo, Carsten Schultz, Edward A. Lemke, Paul Heppenstall, Christian Eggeling, Suliana Manley, and Kai Johnsson. A near-infrared fluorophore for live-cell super-resolution microscopy of cellular proteins. *Nature Chemistry*, 5:132–139, 2013. doi: 10.1038/nchem.1546.

Gražvydas Lukinavičius, Luc Reymond, Elisa D'Este, Anastasiya Masharina, Fabian Göttfert, Haisen Ta, Angelika Güther, Mathias Fournier, Stefano Rizzo, Herbert Waldmann, Claudia Blaukopf, Christoph Sommer, Daniel W Gerlich, Hans-Dieter Arndt, Stefan W Hell, and Kai Johnsson. Fluorogenic probes for live-cell imaging of the cytoskeleton. *Nature Methods*, 11:731–733, 2014. doi: 10.1038/nmeth.2972.

Gražvydas Lukinavičius, Luc Reymond, Keitaro Umezawa, Olivier Sallin, Elisa D'Este, Fabian Göttfert, Haisen Ta, Stefan W. Hell, Yasuteru Urano, and Kai Johnsson. Fluorogenic Probes for Multicolor Imaging in Living Cells. *Journal of the American Chemical Society*, 138:9365–9368, 2016. doi: 10.1021/jacs.6b04782.

Sandra Maday, Karen E. Wallace, and Erika L.F. Holzbaur. Autophagosomes initiate distally and mature during transport toward the cell soma in primary neurons. *Journal of Cell Biology*, 196:407–417, 2012. doi: 10.1083/jcb.201106120.

Sandra Maday, Alison E. Twelvetrees, Armen J. Moughamian, and Erika L.F. Holzbaur. Axonal Transport: Cargo-Specific Mechanisms of Motility and Regulation. *Neuron*, 84: 292–309, 2014. doi: 10.1016/J.NEURON.2014.10.019.

Roop Mallik, Brian C. Carter, Stephanie A. Lex, Stephen J. King, and Steven P. Gross. Cytoplasmic dynein functions as a gear in response to load. *Nature*, 427:649–652, 2004. doi: 10.1038/nature02293.

Pierre Mangeol, Bram Prevo, and Erwin J. G. Peterman. KymographClear and KymographDirect: two tools for the automated quantitative analysis of molecular and cellular dynamics using kymographs. *Molecular Biology of the Cell*, 27:1948–1957, 2016. doi: 10.1091/mbc.e15-06-0404.

MaryAnn Martin, Stanley J. Iyadurai, Andrew Gassman, Joseph G. Gindhart, Thomas S. Hays, and William M. Saxton. Cytoplasmic Dynein, the Dynactin Complex, and Kinesin Are Interdependent and Essential for Fast Axonal Transport. *Molecular Biology of the Cell*, 10:3717–3728, 1999. doi: 10.1091/mbc.10.11.3717.

Richard J. McKenney, Walter Huynh, Marvin E. Tanenbaum, Gira Bhabha, and Ronald D. Vale. Activation of cytoplasmic dynein motility by dynactin-cargo adapter complexes. *Science*, 345:337–341, 2014. doi: 10.1126/science.1254198.

Tiberiu S. Mihaila, Carina Bäte, Lynn M. Ostersehlt, Jasmin K. Pape, Jan Keller-Findeisen, Steffen J. Sahl, and Stefan W. Hell. Enhanced incorporation of subnanometer tags into cellular proteins for fluorescence nanoscopy via optimized genetic code expansion. *Proceedings of the National Academy of Sciences*, 119, 2022. doi: 10.1073/PNAS.2201861119.

Saurabh S Mogre, Aidan I Brown, and Elena F Koslover. Getting around the cell: physical transport in the intracellular world. *Physical Biology*, 17:061003, 2020. doi: 10.1088/1478-3975/aba5e5.

Robert L. Morris and Peter J. Hollenbeck. The regulation of bidirectional mitochondrial transport is coordinated with axonal outgrowth. *Journal of Cell Science*, 104:917–927, 1993. doi: 10.1242/JCS.104.3.917.

Armen J. Moughamian, Gregory E. Osborn, Jacob E. Lazarus, Sandra Maday, and Erika L.F. Holzbaur. Ordered Recruitment of Dynactin to the Microtubule Plus-End is Required for Efficient Initiation of Retrograde Axonal Transport. *Journal of Neuroscience*, 33:13190–13203, 2013. doi: 10.1523/JNEUROSCI.0935-13.2013.

Kenneth R. Myers, Kevin W.-H. Lo, R. John Lye, John M. Kogoy, Violetta Soura, Majid Hafezparast, and K. Kevin Pfister. Intermediate chain subunit as a probe for cytoplasmic dynein function: Biochemical analyses and live cell imaging in PC12 cells. *Journal of Neuroscience Research*, 85:2640–2647, 2007. doi: 10.1002/jnr.21213.

Melanie J. I. Müller, Stefan Klumpp, and Reinhard Lipowsky. Tug-of-war as a cooperative mechanism for bidirectional cargo transport by molecular motors. *Proceedings of the National Academy of Sciences*, 105:4609–4614, 2008. doi: 10.1073/pnas.0706825105.

Maxence V. Nachury and David U. Mick. Establishing and regulating the composition of cilia for signal transduction. *Nature Reviews Molecular Cell Biology*, 20:389–405, 2019. doi: 10.1038/s41580-019-0116-4.

Xiaolin Nan, Peter A. Sims, Peng Chen, and X. Sunney Xie. Observation of Individual Microtubule Motor Steps in Living Cells with Endocytosed Quantum Dots. *The Journal of Physical Chemistry B*, 109:24220–24224, 2005. doi: 10.1021/jp056360w.

Matthew P. Nicholas, Florian Berger, Lu Rao, Sibylle Brenner, Carol Cho, and Arne Gennerich. Cytoplasmic dynein regulates its attachment to microtubules via nucleotide state-switched mechanosensing at multiple AAA domains. *Proceedings of the National Academy of Sciences*, 112:6371–6376, 2015. doi: 10.1073/pnas.1417422112.

Stefan Niekamp, Nico Stuurman, Nan Zhang, and Ronald D. Vale. Three-color single-molecule imaging reveals conformational dynamics of dynein undergoing motility. *Proceedings of the National Academy of Sciences*, 118:e2101391118, 2021. doi: 10.1073/pnas.2101391118.

Noritaka Nishida, Yuta Komori, Osamu Takarada, Atsushi Watanabe, Satoko Tamura, Satoshi Kubo, Ichio Shimada, and Masahide Kikkawa. Structural basis for two-way communication between dynein and microtubules. *Nature Communications*, 11:1038, 2020. doi: 10.1038/s41467-020-14842-8.

Maria G Paez-Segala, Mei G Sun, Gleb Shtengel, Sarada Viswanathan, Michelle A Baird, John J Macklin, Ronak Patel, John R Allen, Elizabeth S Howe, Grzegorz Piszczek, Harald F Hess, Michael W Davidson, Yalin Wang, and Loren L Looger. Fixation-resistant photoactivatable fluorescent proteins for CLEM. *Nature Methods*, 12:215–218, 2015. doi: 10.1038/nmeth.3225.

B M Paschal, H S Shpetner, and R B Vallee. MAP 1C is a microtubule-activated ATPase which translocates microtubules in vitro and has dynein-like properties. *The Journal of cell biology*, 105:1273–1282, 1987. doi: 10.1083/jcb.105.3.1273.

Bryce M. Paschal and Richard B. Vallee. Retrograde transport by the microtubule-associated protein MAP 1C. *Nature*, 330:181–183, 1987. doi: 10.1038/330181a0.

Chunte Sam Peng, Yunxiang Zhang, Qian Liu, G. Edward Marti, Yu-Wen Alvin Huang, Thomas C. Südhof, Bianxiao Cui, and Steven Chu. Nanometer-resolution tracking of single cargo reveals dynein motor mechanisms. *Nature Chemical Biology*, pages 1–9, 2024. doi: 10.1038/s41589-024-01694-2.

Franck Perez, Georgios S. Diamantopoulos, Romaine Stalder, and Thomas E. Kreis. CLIP-170 Highlights Growing Microtubule Ends In Vivo. *Cell*, 96:517–527, 1999. doi: 10.1016/S0092-8674(00)80656-X.

Rob Phillips, Jane Kondev, Julie Theriot, Hernan G. Garcia, and Nigel Orme. *Physical Biology of the Cell*. Garland Science, 2012. doi: 10.1201/9781134111589.

Douglas C. Prasher, Virginia K. Eckenrode, William W. Ward, Frank G. Prendergast, and Milton J. Cormier. Primary structure of the Aequorea victoria green-fluorescent protein. *Gene*, 111:229–233, 1992. doi: 10.1016/0378-1119(92)90691-H.

E. M. Purcell. Life at low Reynolds number. *American Journal of Physics*, 45:3–11, 1977. doi: 10.1119/1.10903.

Weihong Qiu, Nathan D Derr, Brian S Goodman, Elizabeth Villa, David Wu, William Shih, and Samara L Reck-Peterson. Dynein achieves processive motion using both stochastic and coordinated stepping. *Nature Structural and Molecular Biology*, 19:193–200, 2012. doi: 10.1038/nsmb.2205.

Michael Ratz, Ilaria Testa, Stefan W. Hell, and Stefan Jakobs. CRISPR/Cas9-mediated endogenous protein tagging for RESOLFT super-resolution microscopy of living human cells. *Scientific Reports*, 5:9592, 2015. doi: 10.1038/srep09592.

Samara L. Reck-Peterson, Ahmet Yildiz, Andrew P. Carter, Arne Gennerich, Nan Zhang, and Ronald D. Vale. Single-Molecule Analysis of Dynein Processivity and Stepping Behavior. *Cell*, 126:335–348, 2006. doi: 10.1016/j.cell.2006.05.046.

Samara L. Reck-Peterson, William B. Redwine, Ronald D. Vale, and Andrew P. Carter. The cytoplasmic dynein transport machinery and its many cargoes. *Nature Reviews Molecular Cell Biology*, 19:382–398, 2018. doi: 10.1038/s41580-018-0004-3.

Michael J. Rust, Mark Bates, and Xiaowei Zhuang. Sub-diffraction-limit imaging by stochastic optical reconstruction microscopy (STORM). *Nature Methods*, 3:793–796, 2006. doi: 10.1038/nmeth929.

Steffen J. Sahl, Stefan W. Hell, and Stefan Jakobs. Fluorescence nanoscopy in cell biology. *Nature Reviews Molecular Cell Biology*, 18:685–701, 2017. doi: 10.1038/nrm.2017.71.

Lukas Scheiderer, Jan O. Wirth, Miroslaw Tarnawski, and Stefan W. Hell. Dual-color MINFLUX: Kinesin-1 takes Chassé-Inchworm steps. *bioRxiv*, 2024.03.05.583551, 2024. doi: 10.1101/2024.03.05.583551.

Johannes Schindelin, Ignacio Arganda-Carreras, Erwin Frise, Verena Kaynig, Mark Longair, Tobias Pietzsch, Stephan Preibisch, Curtis Rueden, Stephan Saalfeld, Benjamin Schmid, Jean-Yves Tinevez, Daniel James White, Volker Hartenstein, Kevin Eliceiri, Pavel Tomancak, and Albert Cardona. Fiji: an open-source platform for biological-image analysis. *Nature Methods*, 9:676–682, 2012. doi: 10.1038/nmeth.2019.

Max A Schlager, Ha Thi Hoang, Linas Urnavicius, Simon L Bullock, and Andrew P Carter. In vitro reconstitution of a highly processive recombinant human dynein complex. *The EMBO Journal*, 33:1855–1868, 2014. doi: 10.15252/embj.201488792.

Roman Schmidt, Tobias Weihs, Christian A. Wurm, Isabelle Jansen, Jasmin Rehman, Steffen J. Sahl, and Stefan W. Hell. MINFLUX nanometer-scale 3D imaging and microsecond-range tracking on a common fluorescence microscope. *Nature Communications*, 12:1478, 2021. doi: 10.1038/s41467-021-21652-z.

Mark J. Schnitzer and Steven M. Block. Kinesin hydrolyses one ATP per 8-nm step. *Nature*, 388:386–390, 1997. doi: 10.1038/41111.

Alexey Sharonov and Robin M. Hochstrasser. Wide-field subdiffraction imaging by accumulated binding of diffusing probes. *Proceedings of the National Academy of Sciences*, 103: 18911–18916, 2006. doi: 10.1073/pnas.0609643104.

David J. Sharp, Gregory C. Rogers, and Jonathan M. Scholey. Microtubule motors in mitosis. *Nature*, 407:41–47, 2000. doi: 10.1038/35024000.

Sheng Min Shih, Benjamin D Engel, Fatih Kocabas, Thomas Bilyard, Arne Gennerich, Wallace F Marshall, and Ahmet Yildiz. Intraflagellar transport drives flagellar surface motility. *eLife*, 2, 2013. doi: 10.7554/eLife.00744.

James N. Sleigh, Alexander M. Rossor, Alexander D. Fellows, Andrew P. Tosolini, and Giampietro Schiavo. Axonal transport and neurological disease. *Nature Reviews Neurology*, 15:691–703, 2019. doi: 10.1038/s41582-019-0257-2.

Joseph Slivka, Emma Gleave, Devinda P Wijewardena, John T Canty, Paul R Selvin, Andrew P Carter, and Ahmet Yildiz. Stepping dynamics of dynein characterized by MINFLUX. *bioRxiv*, 2024.07.16.603667, 2024. doi: 10.1101/2024.07.16.603667.

Virupakshi Soppina, Arpan Kumar Rai, Avin Jayesh Ramaiya, Pradeep Barak, and Roop Mallik. Tug-of-war between dissimilar teams of microtubule motors regulates transport and fission of endosomes. *Proceedings of the National Academy of Sciences*, 106:19381–19386, 2009. doi: 10.1073/pnas.0906524106.

Xiaoli Sun, Aihua Zhang, Brenda Baker, Luo Sun, Angela Howard, John Buswell, Damien Maurel, Anastasiya Masharina, Kai Johnsson, Christopher J. Noren, Ming Qun Xu, and Ivan R. Corrêa. Development of SNAP-Tag Fluorogenic Probes for Wash-Free Fluorescence Imaging. *ChemBioChem*, 12:2217–2226, 2011. doi: 10.1002/CBIC.201100173.

Keiichiro Suzuki, Yuji Tsunekawa, Reyna Hernandez-Benitez, Jun Wu, Jie Zhu, Euiseok J. Kim, Fumiyuki Hatanaka, Mako Yamamoto, Toshikazu Araoka, Zhe Li, Masakazu Kurita, Tomoaki Hishida, Mo Li, Emi Aizawa, Shicheng Guo, Song Chen, April Goebl, Rupa Devi Soligalla, Jing Qu, Tingshuai Jiang, Xin Fu, Maryam Jafari, Concepcion Rodriguez Esteban, W. Travis Berggren, Jeronimo Lajara, Estrella Nuñez-Delicado, Pedro Guillen, Josep M. Campistol, Fumio Matsuzaki, Guang-Hui Liu, Pierre Magistretti, Kun Zhang, Edward M. Callaway, Kang Zhang, and Juan Carlos Izpisua Belmonte. In vivo genome editing via CRISPR/Cas9 mediated homology-independent targeted integration. *Nature*, 540:144–149, 2016. doi: 10.1038/nature20565.

Nireekshit Addanki Tirumala, Gregory Michael Ian Redpath, Sarah Viktoria Skerhut, Pritha Dolai, Natasha Kapoor-Kaushik, Nicholas Ariotti, K. Vijay Kumar, and Vaishnavi Ananthanarayanan. Single-molecule imaging of stochastic interactions that drive dynein activation and cargo movement in cells. *Journal of Cell Biology*, 223, 2024. doi: 10.1083/jcb.202210026.

Shiori Toba, Tomonobu M. Watanabe, Lisa Yamaguchi-Okimoto, Yoko Yano Toyoshima, and Hideo Higuchi. Overlapping hand-over-hand mechanism of single molecular motility of cytoplasmic dynein. *Proceedings of the National Academy of Sciences*, 103:5741–5745, 2006. doi: 10.1073/pnas.0508511103.

Makio Tokunaga, Naoko Imamoto, and Kumiko Sakata-Sogawa. Highly inclined thin illumination enables clear single-molecule imaging in cells. *Nature Methods*, 5:159–161, 2008. doi: 10.1038/nmeth1171.

Alison E E. Twelvetrees, Stefano Pernigo, Anneri Sanger, Pedro Guedes-Dias, Giampietro Schiavo, Roberto A A. Steiner, Mark P P. Dodding, and Erika L L.F. Holzbaur. The Dynamic Localization of Cytoplasmic Dynein in Neurons Is Driven by Kinesin-1. *Neuron*, 90:1000–1015, 2016. doi: 10.1016/J.NEURON.2016.04.046.

Linas Urnavicius, Kai Zhang, Aristides G. Diamant, Carina Motz, Max A. Schlager, Minmin Yu, Nisha A. Patel, Carol V. Robinson, and Andrew P. Carter. The structure of the dynactin complex and its interaction with dynein. *Science*, 347:1441–1446, 2015. doi: 10.1126/science.aaa4080.

Linas Urnavicius, Clinton K. Lau, Mohamed M. Elshenawy, Edgar Morales-Rios, Carina Motz, Ahmet Yildiz, and Andrew P. Carter. Cryo-EM shows how dynactin recruits two dyneins for faster movement. *Nature*, 554:202–206, 2018. doi: 10.1038/nature25462.

R D Vale, F Malik, and D Brown. Directional instability of microtubule transport in the presence of kinesin and dynein, two opposite polarity motor proteins. *The Journal of cell biology*, 119:1589–1596, 1992. doi: 10.1083/jcb.119.6.1589.

Ronald D Vale. The Molecular Motor Toolbox for Intracellular Transport. *Cell*, 112:467–480, 2003. doi: 10.1016/S0092-8674(03)00111-9.

Myrrhe van Spronsen, Marina Mikhaylova, Joanna Lipka, Max A. Schlager, Dave J. van den Heuvel, Marijn Kuijpers, Phebe S. Wulf, Nanda Keijzer, Jeroen Demmers, Lukas C. Kapitein, Dick Jaarsma, Hans C. Gerritsen, Anna Akhmanova, and Casper C. Hoogenraad. TRAK/Milton Motor-Adaptor Proteins Steer Mitochondrial Trafficking to Axons and Dendrites. *Neuron*, 77:485–502, 2013. doi: 10.1016/j.neuron.2012.11.027.

Patricia S. Vaughan, John D. Leszyk, and Kevin T. Vaughan. Cytoplasmic Dynein Intermediate Chain Phosphorylation Regulates Binding to Dynactin. *Journal of Biological Chemistry*, 276:26171–26179, 2001. doi: 10.1074/jbc.M102649200.

Wilhelm J. Walter and Stefan Diez. A staggering giant. *Nature*, 482:44–45, 2012. doi: 10.1038/482044a.

Lu Wang, Mai Tran, Elisa D'Este, Julia Roberti, Birgit Koch, Lin Xue, and Kai Johnsson. A general strategy to develop cell permeable and fluorogenic probes for multicolour nanoscopy. *Nature Chemistry*, 12:165–172, 2020. doi: 10.1038/s41557-019-0371-1.

Michael A Welte. Bidirectional Transport along Microtubules. *Current Biology*, 14:R525–R537, 2004. doi: 10.1016/j.cub.2004.06.045.

Michael A Welte, Steven P Gross, Marya Postner, Steven M Block, and Eric F Wieschaus. Developmental Regulation of Vesicle Transport in Drosophila Embryos: Forces and Kinetics. *Cell*, 92:547–557, 1998. doi: 10.1016/S0092-8674(00)80947-2.

Jelmer Willems, Arthur P. H. de Jong, Nicky Scheefhals, Eline Mertens, Lisa A. E. Catsburg, Rogier B. Poorthuis, Fred de Winter, Joost Verhaagen, Frank J. Meye, and Harold D. MacGillavry. ORANGE: A CRISPR/Cas9-based genome editing toolbox for epitope tagging of endogenous proteins in neurons. *PLOS Biology*, 18:e3000665, 2020. doi: 10.1371/journal.pbio.3000665.

Jan O. Wirth, Lukas Scheiderer, Tobias Engelhardt, Johann Engelhardt, Jessica Matthias, and Stefan W. Hell. MINFLUX dissects the unimpeded walking of kinesin-1. *Science*, 379: 1004–1010, 2023. doi: 10.1126/science.ade2650.

Lin Xue, Iuliia A Karpenko, Julien Hiblot, and Kai Johnsson. Imaging and manipulating proteins in live cells through covalent labeling. *Nature Chemical Biology*, 11:917–923, 2015. doi: 10.1038/nchembio.1959.

Ahmet Yildiz and Paul R. Selvin. Fluorescence Imaging with One Nanometer Accuracy: Application to Molecular Motors. *Accounts of Chemical Research*, 38:574–582, 2005. doi: 10.1021/ar040136s.

Ahmet Yildiz and Yuanchang Zhao. Dyneins. *Current Biology*, 33:R1274–R1279, 2023. doi: 10.1016/J.CUB.2023.10.064.

Ahmet Yildiz, Michio Tomishige, Ronald D. Vale, and Paul R. Selvin. Kinesin Walks Hand-Over-Hand. *Science*, 303:676–678, 2004. doi: 10.1126/science.1093753.

David A. Zacharias, Jonathan D. Violin, Alexandra C. Newton, and Roger Y. Tsien. Partitioning of Lipid-Modified Monomeric GFPs into Membrane Microdomains of Live Cells. *Science*, 296:913–916, 2002. doi: 10.1126/science.1068539.

Kai Zhang, Helen E. Foster, Arnaud Rondelet, Samuel E. Lacey, Nadia Bahi-Buisson, Alexander W. Bird, and Andrew P. Carter. Cryo-EM Reveals How Human Cytoplasmic Dynein Is Auto-inhibited and Activated. *Cell*, 169:1303–1314.e18, 2017. doi: 10.1016/j.cell.2017.05.025.

List of Figures

List of Tables

Acknowledgments

I would like to express my sincerest gratitude to my supervisor Prof. Dr. Stefan W. Hell for providing me with the unique opportunity to conduct research within his department. He provided me with all the necessary resources and offered valuable guidance and mentorship on my research ideas, as well as support in my family formation.

Furthermore, I would like to express my gratitude to Prof. Dr. Joachim Spatz for agreeing to referee my thesis, and to Prof. Dr. Selim Jochim and Prof. Dr. Ulrich Schwarz for their participation as members of the examination committee.

Moreover, I would like to acknowledge the assistance of Dr. Johann Engelhardt, Dr. Jessica Matthias, and Dr. Elisa D'Este, who served as my primary contacts for technical, optical, or biological inquiries. I would also like to extend my gratitude to Jasmine Hubrich, who assisted in generating the CRISPR/Cas9 knock-in plasmids and introduced me to neuronal handling and laboratory techniques. Moreover, I would like to thank the members of the Optical Nanoscopy department for their helpful and cheerful discussions. My gratitude also extends to Dr. Jade Cottam Jones for providing an excellent organizational framework, as well as to Prof. Dr. Kai Johnsson and Dr. Alexey Butkevich for the provision of fluorophores.

I would also like to express my profound gratitude to my long-time friends and family who have accompanied me for many years and have provided me with invaluable support in all circumstances.

Finally, my special thanks go to my beloved wife Mirjam, who has stood by my side faithfully, carried me through challenging phases of my doctorate, enriches my life immensely, and loves me from the bottom of her heart.

Soli Deo gloria.

Groß sind die Werke des HERRN; wer sie erforscht, der hat Freude daran.

—Psalm 111,2